A study of proton emission following nuclear muon capture for the COMET experiment

Nam Hoai Tran

Department of Physics, Graduate School of Science
Osaka University

Abstract

COMET [1] is an experiment that aims to search for a charged lepton flavour violation (CLFV) process, the muon-to-electron conversion in the presence of a nucleus, $\mu^- N \rightarrow e^- N$. The process is forbidden in the Standard Model (SM), however is predicted to occur in various extensions of SM. Current experimental upper limit of the branching ratio is $BR(\mu^- + Au \rightarrow e^- + Au) < 7 \times 10^{-13}$, set by the SINDRUM II experiment [2].

Using the J-PARC proton beam and the pion capture by a solenoidal field, COMET will have a single event sensitivity 10,000 times better than the current limit. The COMET collaboration has taken a phased approach in which the first phase, COMET Phase-I [3], starts in 2013 and initial data taking in around 2017.

In order to optimize detector design for the Phase-I, backgrounds from nuclear muon capture are crucial. We have proposed a dedicated experiment, namely AlCap, at PSI, Switzerland to study the backgrounds, including protons, neutrons and photons. The measurements of proton rate and spectrum on aluminium have been carried out in the 2013 run. The second run to study neutrons and photons is planned in 2015.

The preliminary results from the analysis of the 2013 run are presented in this thesis. The measured proton spectrum peaks at 3.7 MeV and decays exponentially with the decay constant of 2.6 MeV. The emission rate of protons in the energy range from 4 MeV to 8 MeV is $(1.7 \pm 0.1)\%$. The total proton emission rate is estimated to be $(3.5 \pm 0.2)\%$ assuming the spectrum shape holds. The resulted proton rate and spectrum were used to optimise the tracking detector hit rate of the COMET Phase-I.

Declaration

This dissertation is the result of my own work, except where explicit reference is made to the work of others, and has not been submitted for another qualification to this or any other university.

Nam Hoai Tran

Acknowledgements

First and foremost I would like to thank my supervisor Yoshitaka Kuno, for his great support and almost infinite patience in last four years. I am also grateful to all members of the Kuno group, Department of Physics, Osaka University. Thanks to Akira Sato, Hideyuki Sakamoto for the knowledge and supervision they have provided. And to Takahisa Itahashi for the advice and allowing me to practice on his expensive silicon detectors.

The measurement described in this thesis is the product of effort of all members of the AlCap Collaboration. Special thanks to Peter Kammel for always pushing the experiment forward and your very helpful advices. I enjoyed the stays at your group at University of Washington in Seattle a lot. I would also like to thank the fellow graduate students in the collaboration Andy, John, Ben, Damien for all the hard work in the beam time, in the analysis phase, and also for the beers. I wish you all success with your work.

Finally, I would like to thank my family and friends. Without your love and support I wouldn't make it through these long years of graduate school.

Contents

Chapter 1

Overview

1.1 Introduction

The COMET experiment [1], proposed at the Japan Proton Accelerator Research Complex (J-PARC), is a next-generation-experiment that searches for evidence of charged lepton flavour violation (CLFV) with muons. The branching ratio of CLFV in the Standard Model, even with massive neutrinos, is prohibitively small, at the order of 10^{-54}. Therefore, any experimental observation of CLFV would be a clear signal of new physics beyond the SM.

The COMET (**CO**herent **M**uon to **E**lectron **T**ransition) Collaboration aims to probe the conversion of a muon to an electron in a nucleus field at a single event sensitivity of 6×10^{-17}, pushing for a four orders of magnitude improvement from the current limit set by the SINDRUM-II [2]. A staging approach is adopted at the COMET to achieve an intermediate physics result, as well as to gain operational experience. The first stage, COMET Phase I, is scheduled to start data taking in 2016 with the goal single event sensitivity of 3×10^{-15} after a three-month running period.

A cylindrical drift chamber being developed by the Osaka University group together with the Kyushu University group and the Chinese groups will be a main tracking detector in the COMET Phase I. It is anticipated that the chamber will be heavily occupied by protons emitted after nuclear muon capture in the stopping target, and thus an absorber will be installed to reduce the proton hit rate to a tolerable level. A study of proton emission following nuclear muon capture for optimisation of the proton absorber is presented in this thesis.

The thesis is structured as follows: firstly, the physics motivation of the COMET experiment, with muon's normal decays and CLFV decays, is described in this later part of this chapter. Chapter 2 gives an overview of the COMET experiment: beam lines, detectors and their requirements, and expected sensitivities. Details of the study on proton emission are described in Chapters 3, 4, 5: physics, method, experimental set up, data analysis. The results and impacts of the study on COMET Phase-I design is discussed in Chapter 6.

1.2 Lepton flavour

According to the SM, all matter is built from a small set of fundamental spin one-half particles, called fermions: six quarks and six leptons. The six leptons form three generations (or flavours), namely:

$$\begin{pmatrix} \nu_e \\ e^- \end{pmatrix}, \quad \begin{pmatrix} \nu_\mu \\ \mu^- \end{pmatrix} \quad \text{and} \quad \begin{pmatrix} \nu_\tau \\ \tau^- \end{pmatrix}.$$

Each lepton is assigned a lepton flavour quantum number, L_e, L_μ, L_τ, equals to $+1$ for each lepton and -1 for each antilepton of the appropriate generation. The lepton flavour

number is conserved in the SM, for example in the decay of a positive pion:

$$\begin{array}{cccc} & \pi^+ & \to \mu^+ & + \nu_\mu \\ L_\mu & 0 & -1 & +1 \end{array}$$

or, the interaction of an electron-type antineutrino with a proton (inverse beta decay):

$$\begin{array}{cccccc} & \overline{\nu}_e & + p & \to e^+ & + n \\ L_e & -1 & 0 & -1 & 0 \end{array}$$

The decay of a muon to an electron and a photon, where lepton flavour numbers are violated by one unit or more, is forbidden:

$$\begin{array}{cccc} & \mu^+ & \to e^+ & + \gamma \\ L_\mu & -1 & 0 & 0 \\ L_e & 0 & -1 & 0 \end{array} \tag{1.1}$$

However, it is observed that neutrinos do change flavour in the so-called neutrino oscillations where a neutrino of a certain lepton flavour can be measured to have a different flavour as it travels in space-time. The phenomenon has been confirmed in many experiments with solar neutrinos, atmospheric neutrinos, reactor neutrinos and beam neutrinos. The observation of neutrino oscillations means that the lepton flavour is not strictly conserved and neutrinos are massive. The massive neutrinos allow lepton flavour violation in the charged leptons, but at an unmeasurably small level as described in section 1.4.

1.3 Muon and its decays in the Standard Model

1.3.1 Basic properties of the muon

The muon is a charged lepton, its static properties have been measured with great precisions and are summarised in the "Review of Particle Physics" of the Particle Data Group (PDG) [3]. Some of the basic properties are quoted as follows:

1. The muon mass is given by the muon to electron mass ratio,

$$\frac{m_\mu}{m_e} = 206.7682843 \pm 0.0000052 \tag{1.2}$$

$$m_\mu = 105.6583715 \pm 0.0000035 \text{ MeV}/c^2 \tag{1.3}$$

2. The spin of the muon is determined to be $\frac{1}{2}$ as the measurements of the muon's gyromagnetic give $g_\mu = 2$ within an overall accuracy better than 1 ppm. It is common to quoted the result of g_μ as muon magnetic moment anomaly:

$$\frac{g-2}{2} = (11659209 \pm 6) \times 10^{-10} \tag{1.4}$$

3. The charge of the muon is known to be equal to that of the electron within about 3 ppb,

$$\frac{q_{\mu^+}}{q_{e^-}} + 1 = (1.2 \pm 2.1) \times 10^{-9} \tag{1.5}$$

4. Electric dipole moment:

$$d = \frac{1}{2}(d_{\mu^-} - d_{\mu^+}) = (-0.1 \pm 0.9) \times 10^{-19}\ e \cdot \text{cm} \tag{1.6}$$

5. The muon is not stable, average lifetime of the free muon is:

$$\tau_\mu = 2.1969811 \pm 0.0000022\ \mu\text{s} \tag{1.7}$$

1.3.2 Decays of the muon

Because of charge and lepton flavour conservations, the simplest possible decay of muons is:

$$\mu^- \to e^- \nu_\mu \overline{\nu}_e \tag{1.8}$$

Muons can also decay in the radiative mode:

$$\mu^- \to e^- \nu_\mu \overline{\nu}_e \gamma \tag{1.9}$$

or with an associated e^+e^- pair:

$$\mu \to e^- \nu_\mu \overline{\nu}_e e^+ e^- \tag{1.10}$$

The dominant process, $\mu^- \to e^- \nu_\mu \overline{\nu}_e$ is commonly called the Michel decay. It can be described by the V-A interaction which is a special case of a local, derivative-free, lepton-number-conserving four-fermion interaction. The model contains independent real parameters that can be determined from measurements of muon life time, muon decay and inverse muon decay. Experimental results from extensive measurements of the Michel parameters are consistent with the predictions of the V-A theory [3–5].

The radiative decay (1.9) is treated as an internal bremsstrahlung process [6]. Since it is not possible to clearly separated this mode from the Michel decay in the soft-photon limit, the radiative mode is regarded as a subset of the Michel decay. An additional parameter is included to describe the electron and photon spectra in this decay channel. Like the case of the Michel decay, experiments results on the branching ratio and the parameter are in agreement with the SM's predictions [3].

There is a small probability (order of 10^{-4} [6]) that the photon in $\mu^- \to e^- \nu_\mu \overline{\nu}_e \gamma$ would internally convert to an e^+e^- pair, resulting in the decay mode $\mu^- \to e^- \nu_\mu \overline{\nu}_e e^+ e^-$.

The branching ratios for decay modes of muons, compiled by the PDG, are listed in Table 1.1.

Decay mode	Branching ratio	Remarks
$\mu^- \to e^- \nu_\mu \overline{\nu}_e$	$\simeq 1$	commonly called Michel decay
$\mu^- \to e^- \nu_\mu \overline{\nu}_e \gamma$	0.014 ± 0.004	subset of Michel decay, $E_\gamma > 10$ MeV
$\mu^- \to e^- \nu_\mu \overline{\nu}_e e^+ e^-$	$(3.4 \pm 0.2 \pm 0.3) \times 10^{-5}$	transverse momentum cut $p_T > 17$ MeV/c

Table 1.1: Decay modes and branching ratios of muon listed by PDG [3]

1.4 Lepton flavour violated decays of muons

The existence of the muon has always been a puzzle. At first, people thought that it would be an excited state of the electron. Therefore, the searches for $\mu^+ \to e^+ \gamma$ was performed by Hincks and Pontercorvo [7]; and Sard and Althaus [8]. Those searches failed to find the photon of about 50 MeV that would have accompanied the decay electron in case the two-body decay $\mu^+ \to e^+ \gamma$ had occurred. From the modern point of view, those experiments were the first searches for charged lepton flavour violation (LFV).

Since then, successive searches for LFV with the muon have been carried out. All the results were negative and the limits of the LFV branching ratios had been more and more stringent. Those null-result experiments suggested the lepton flavours - muon flavour L_μ and electron flavour L_e. The notion of lepton flavour was experimentally verified in the Nobel Prize-winning experiment of Danby et al. at Brookhaven National Laboratory (BNL) [9].

Then the concepts of generations of particles was developed [10], and integrated into the SM, in which the lepton flavour conservation is guaranteed by an exact symmetry, owing to massless neutrinos.

Following the above LFV searches with muons, searches with various particles, such as kaons, taus, and others have been done. The upper limit have been improved at a rate of two orders of magnitude per decade.

While all of those searches yielded negative results, LFV with neutrinos is confirmed with observations of neutrino oscillations; i.e. neutrino of one type changes to another type when it travels in space-time. The phenomenon means that there exists a mismatch between the flavour and mass eigenstates of neutrinos; and neutrinos are massive. Therefore, the SM must be modified to accommodate the massive neutrinos.

With the massive neutrinos charged lepton flavour violation (CLFV) must occur through oscillations in loops. But, CLFV processes are highly suppressed in the SM. For example, Marciano and Mori [11] calculated the branching ratio of the process $\mu^+ \to e^+\gamma$ to be $\mathcal{B}(\mu^+ \to e^+\gamma) < 10^{-54}$. Other CLFV processes with muons are also suppressed to similar practically unmeasurable levels. Therefore, any experimental observation of CLFV would be an unambiguous signal of the physics beyond the SM. Many theoretical models for physics beyond the SM, including supersymmetric (SUSY) models, extra dimensional models, little Higgs models, predict significantly larger CLFV [11–13].

Among the CLFV processes, the $\mu^+ \to e^+\gamma$ and the $\mu^- N \to e^- N$ are expected to have large effect in many models. The current experimental limits on these two decay modes are set respectively by the MEG experiment [14] and the SINDRUM-II experiment [2]:

$$\mathcal{B}(\mu^+ \to e^+\gamma) < 5.7 \times 10^{-13}\,, \tag{1.11}$$

and:

$$\mathcal{B}(\mu^- + Au \to e^- + Au) < 7 \times 10^{-13}\,. \tag{1.12}$$

1.5 Phenomenology of $\mu - e$ conversion

The conversion of a captured negative muon in a muonic atom into an electron in the field of a nucleus has been one of the most powerful probe to search for CLFV. This section highlights phenomenology of the $\mu^- N \to e^- N$.

1.5.1 What is $\mu - e$ conversion

When a negatively charged muon is stopped in a material, it is quickly captured by an atom into a high orbital momentum state, forming a muonic atom, then it rapidly cascades to the lowest state 1S. There, it undergoes either:

- normal Michel decay: $\mu^- \to e^- \nu_\mu \overline{\nu}_e$; or
- weak capture by the nucleus: $\mu^- p \to \nu_\mu n$.

In the context of physics beyond the SM, the exotic process of $\mu - e$ conversion where a muon decays to an electron without neutrinos is also expected, but has never been observed:

$$\mu^- + N(A, Z) \to e^- + N(A, Z)\,. \tag{1.13}$$

The emitted electron in this decay mode, the $\mu - e$ conversion electron, is mono-energetic at an energy far above the endpoint of the Michel spectrum (52.8 MeV):

$$E_{\mu e} = m_\mu - E_b - \frac{E_\mu^2}{2m_N}\,. \tag{1.14}$$

where m_μ is the muon mas; $E_b \simeq Z^2\alpha^2 m_\mu/2$ is the binding energy of the muonic atom; and the last term is the nuclear recoil energy neglecting high order terms. For Al ($Z = 13$), the target of choice in the new $\mu - e$ conversion experiments, the outgoing electron has energy of $E_{\mu e} \simeq 104.96$ MeV.

1.5.2 Measurement of $\mu - e$ conversion

The quantity measured in searches for $\mu - e$ conversion is the ratio between the rate of $\mu - e$ conversion, and the rate of all muons captured:

$$R_{\mu e} = \frac{\Gamma(\mu^- N \to e^- N)}{\Gamma(\text{capture})} \tag{1.15}$$

The muon capture rate can be measured by observing the characteristic X-rays emitted when the muon stops, and cascades to the 1S orbit. Since the stopped muon either decays or be captured, the stopping rate is:

$$\Gamma_{\text{stop}} = \Gamma_{\text{decay}} + \Gamma_{\text{capture}} \tag{1.16}$$

The mean lifetime $\tau = 1/\Gamma$, then:

$$\frac{1}{\tau_{\text{stop}}} = \frac{1}{\tau_{\text{decay}}} + \frac{1}{\tau_{\text{capture}}} \tag{1.17}$$

The mean lifetimes of free muons and muons in a material are well-known, therefore the number of captures can be inferred from the number of stops. For aluminium,

$$\frac{\Gamma_{\text{capture}}}{\Gamma_{\text{stop}}} = 0.609 \tag{1.18}$$

and the mean lifetime of stopped muons is 864 ns [15].

The core advantages of the $\mu - e$ conversion searches compares to other CLFV searches ($\mu^+ \to e^+\gamma$ or $\mu^+ \to e^+e^+e^+$) are:

- the emitted electron is the only product, so the measurement is simple, no coincidence is required; and
- the electron is mono-energetic, its energy is far above the endpoint of the Michel spectrum (52.8 MeV) where the background is very clean. Essentially, the only intrinsic physics background comes from decay of the muon orbiting the nucleus.

Chapter 2

The COMET experiment

This chapter describes the new experimental search for $\mu - e$ conversion, namely COMET - (**CO**herent **M**uon to **E**lectron **T**ransition). The experiment will be carried out at the Japan Proton Accelerator Research Complex (J-PARC), aims at a single event sensitivity of 6×10^{-17}, i.e. 10,000 times better than the current best limit.

2.1 Experimental status of $\mu - e$ conversion searches

2.1.1 Experimental history

The searches for $\mu - e$ conversion has been ongoing for more than 50 years, started in 1952 with cosmic rays [16] and then moved to accelerators. The list of upper limits for $\mu - e$ conversion in table 2.1 is reproduced from a recent review of Bernstein and Cooper [13].

Year	**Limit** (90% C.L.)	**Material**	**Reference**
1952	1.0×10^{-1}	Sn, Sb	[16]
1955	5.0×10^{-4}	Cu	[17]
1961	4.0×10^{-6}	Cu	[18]
1961	5.9×10^{-6}	Cu	[19]
1962	2.2×10^{-7}	Cu	[20]
1964	2.2×10^{-7}	Cu	[21]
1972	2.6×10^{-8}	Cu	[22]
1977	4.0×10^{-10}	S	[23]
1982	7.0×10^{-11}	S	[24]
1988	4.6×10^{-12}	Ti	[25]
1993	4.3×10^{-12}	Ti	[26]
1996	4.6×10^{-11}	Pb	[27]
2006	7.0×10^{-13}	Au	[2]

Table 2.1: History of $\mu - e$ conversion experiments with more and more stringent upper limit.

The latest experiments were the SINDRUM and SINDRUM-II at the Paul Scherrer Institute (PSI), Switzerland. The SINDRUM-II (figure 2.1) measured the branching ratio of $\mu - e$ conversion on a series of heavy targets: Ti, Pb and Au. The proton beam at PSI is a continuous beam, with a time structure of 0.3 ns bursts every 19.75 ns. An 8-mm-thick CH_2 degrader was used to reduce the radiative pion capture and other prompt backgrounds. Cosmic backgrounds are rejected using a combination of passive shielding, veto counters and

reconstruction cuts. The momenta of beam muons used in the experiment were 52 MeV/c and 53 MeV/c, and the momentum spread was 2%.

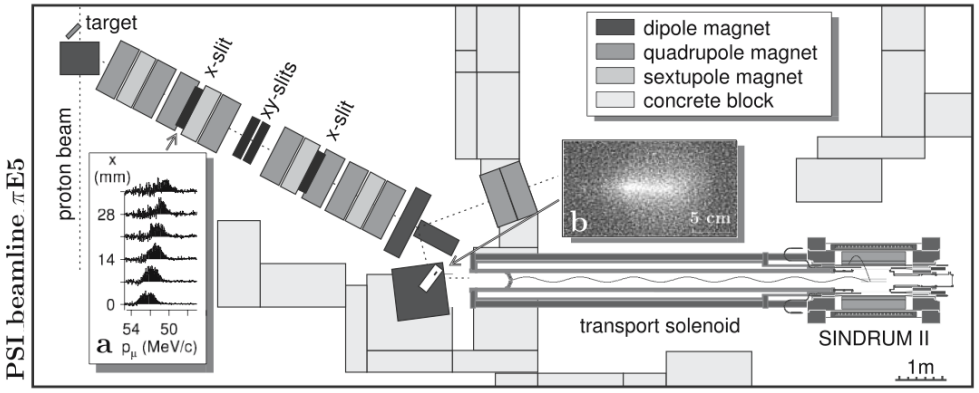

Figure 2.1: SINDRUM-II experimental set up, reprinted from reference [2] with permission from Springer.

Electrons emitted from the target were tracked in a 0.33 T solenoidal magnetic field. Detector system consisted of a superconducting solenoid, two plastic scintillation hodoscopes, a plexiglass Cerenkov hodoscope, and two drift chambers. In the latest measurement, the SINDRUM-II collaboration have not found any conversion electron from captured muons in a gold target, hence set the upper limit for the branching ratio of $\mu - e$ conversion in gold with 90 % C.L. at 7.0×10^{-13}.

The reconstructed momenta of electrons around the signal region from SINDRUM-II is shown in figure 2.2. It can be seen that the muon decay in orbit background falls steeply near the endpoint as expected, but, the prompt background induced by pions still remains even after the cut in timing and track angle. This indicates the problem of pion contamination is very important in probing better sensitivity.

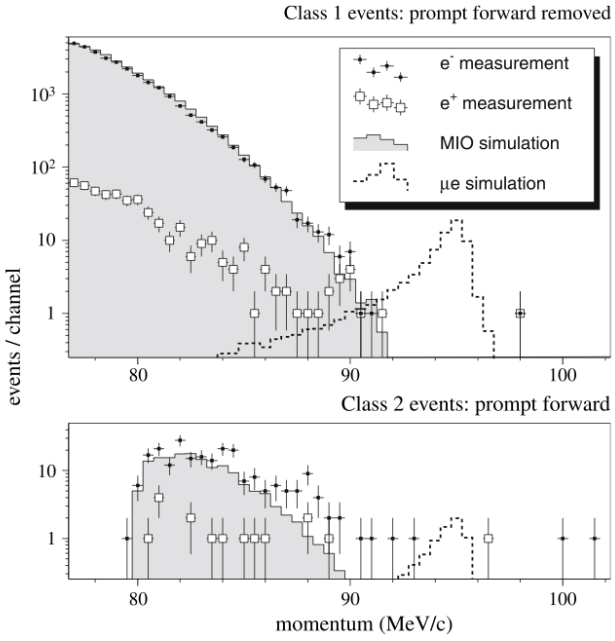

Figure 2.2: SINDRUM-II results showing background events reaching into the signal region. Reprinted from reference [2] with permission from Springer.

2.1.2 New generation of $\mu - e$ conversion experiments

A new generation of $\mu - e$ conversion experiments have been proposed with scenarios to overcome pion induced background in the SINDRUM-II. Lobashev and collaborators first suggested the basic idea for new $\mu - e$ conversion at the Moscow Muon Factory; this idea was used to develop the MECO experiment at Brookhaven National Laboratory. The MECO experiment was cancelled due to budget constraints. Two recent experiments, COMET at J-PARC and Mu2e at Fermilab, use the initial idea with more upgrades and modifications.

The basic ideas of the two experiments are:

1. Highly intense muon source: the total number of muons needed is of the order of 10^{18} in order to achieve a sensitivity of 10^{-16}. This can be done by producing more pions using a high power proton beam, and having a high efficiency pion collection system;

2. Pulsed proton beam: the proton pulse should be short compares to the lifetime of muons in the stopping target material, and the period between pulses should be long enough for prompt backgrounds from pion to decay before beginning the measurement. It is also crucial that there is no proton leaks into the measuring interval;

3. Curved solenoids for charge and momentum selection: at first, the curved solenoids remove the line of sight backgrounds. A charged particle travels through a curved solenoidal magnetic field has the centre of the helical motion drifted up or down with respect to the bending plane depends on the sign of the charge, and the magnitude of the drift is proportional to its momentum. By using this effect and placing suitable collimators, charge and momentum selection can be made. Details of the magnet system are described in section 2.2.2 and section 2.2.3.

2.2 Concepts of the COMET experiment

This section elaborates the design choices of the COMET to realise the basic ideas mentioned previously. Figures and numbers, other than noted, are taken from the COMET's documentations:

- Conceptual design report for the COMET experiment [28],
- Experimental Proposal for Phase-I of the COMET Experiment at J-PARC [29],
- and COMET Phase-I Technical Design Report [30].

2.2.1 Proton beam

A high power pulsed proton beam is of utmost importance to achieve the desired sensitivity of the COMET experiment. A slow-extracted proton beam from the J-PARC main ring (MR), which is designed to deliver 3.6×10^{15} protons per cycle at a frequency of 0.45 Hz, will be used for the COMET experiment. The proton beam power of the current design is $8\,\mathrm{GeV} \times 7\,\mu\mathrm{A}$, or 4.4×10^{13} protons/s at 8 GeV. The beam energy was chosen to minimise the production of antiprotons which may introduce background events.

The proton pulse width is chosen to be 100 ns, and the pulse period to be from 1 µs to 2 µs. This time structure is sufficient for the search for $\mu - e$ conversion in an aluminium target where the mean lifetime of negative muons in muonic atoms is 864 ns. One possible plan of accelerator operation to realise the beam pulsing is shown in figure 2.3, where 4 out of 9 MR buckets are filled.

As mentioned, it is very important that there is no stray proton arrives in the measuring period between two proton bunches. An extinction factor is defined as the ratio between

number of protons in between two pulses and the number of protons in the main pulse. In order to achieve the goal sensitivity of the COMET, an extinction factor less than 10^{-9} is required.

Requirements for the proton beam are summarised in table 2.2.

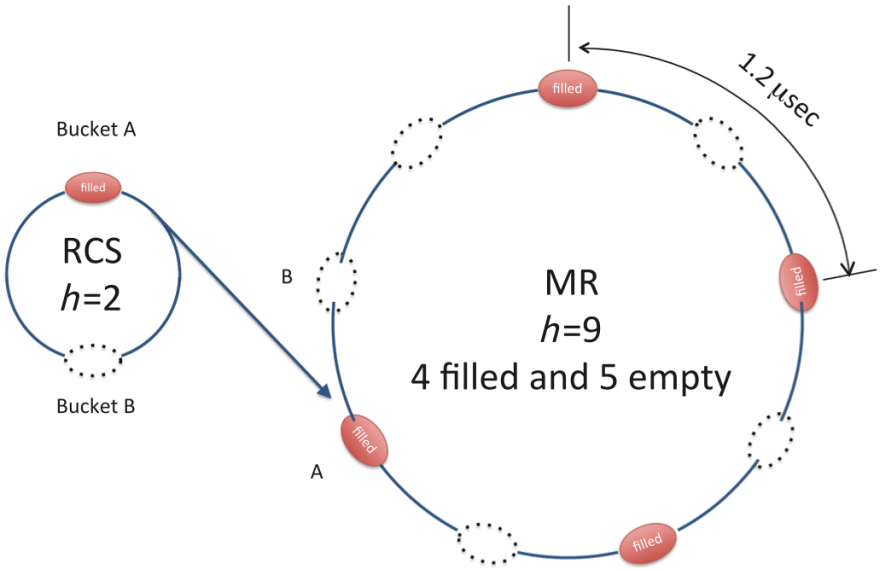

Figure 2.3: The COMET proton bunch structure in the RCS (Rapid Cycling Synchrotron) and MR where 4 buckets are filled producing 100 ns bunches separated by 1.2 μs.

Beam power	56 kW
Energy	8 GeV
Average current	7 μA
Beam emittance	10 $\pi\cdot$ mm$\cdot$ mrad
Protons per bunch	$< 10^{11}$
Extinction	10^{-9}
Bunch separation	$1 \sim 2$ μs
Bunch length	100 ns

Table 2.2: Pulsed proton beam for the COMET experiment

2.2.2 Pion production and capture solenoid

Muons for the COMET experiment are produced by colliding the proton beam with a pion production target, made of either platinum, gold or tungsten, collecting pions and then letting them decay. To collect as many pions (and cloud muons) as possible, the pions are captured using a high solenoidal magnetic field with a large solid angle. Since muons will be stopped in a conversion target, low energy muons, and thus low energy pions, are preferred. It is known from other measurements that backward scattered pions (with respect to proton beam direction) of high energy are suppressed, and the yield of low energy pions in the backward direction is not too low compares to that of the forward direction (see figure 2.4). For these reasons, the COMET decided to collect backward pions. The pion capture system is composed of several superconducting solenoids: capture solenoids and matching solenoids. The magnetic field distribution along the beam axis of the COMET

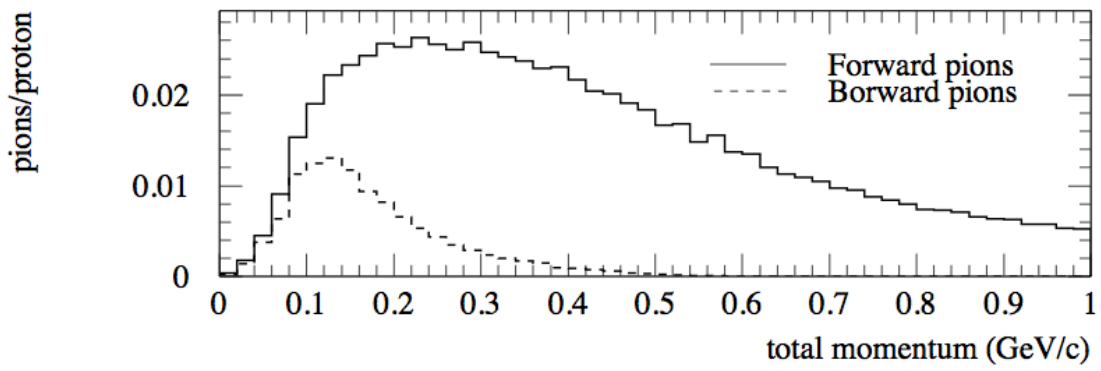

Figure 2.4: Comparison between backward and forward pions production in a gold target.

is shown in figure 2.5. The peak field of 5 T is created by the capture solenoid, and the matching solenoids provide a smooth transition from that peak field to the 3 T field in the pions/muons transportation region. The superconducting solenoids are cooled by liquid helium, and a radiation shield composed of copper and tungsten will be installed inside the cryostat to reduce radiation heat load.

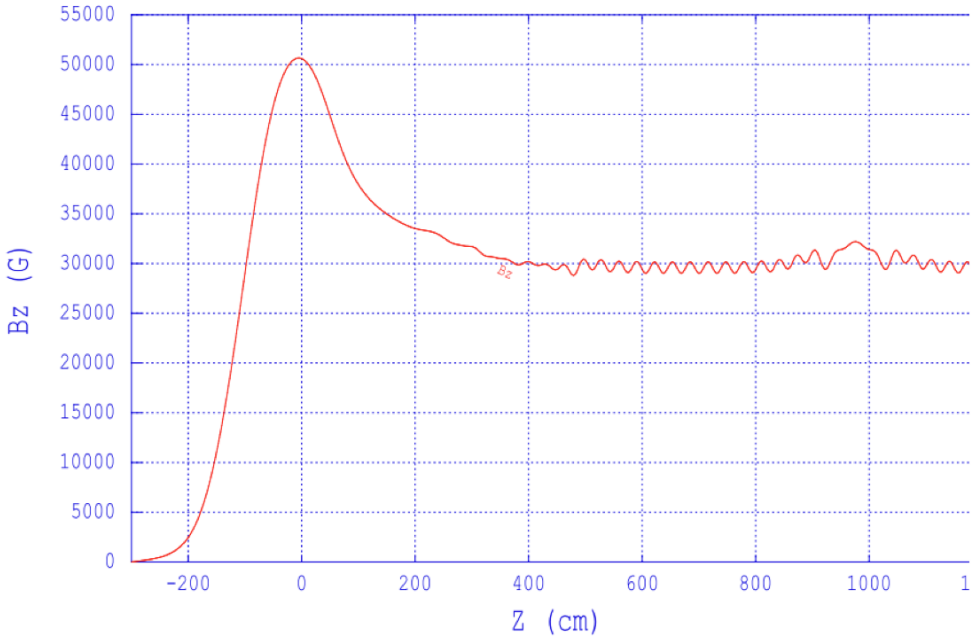

Figure 2.5: Magnetic field distribution along the COMET beam line.

2.2.3 Pions and muons transportation solenoids

Muons and pions are transported to the muon stopping target through a muon beam line, which includes several curved and straight superconducting solenoid magnets. A schematic layout of the muon beam line, include the capture and detector sections, is shown in figure 2.6.

The requirements for the muon transportation beam line are:

- being long enough for pions to decay, for instance, the survival rate of pions will be about 2×10^{-3} after 20 m;

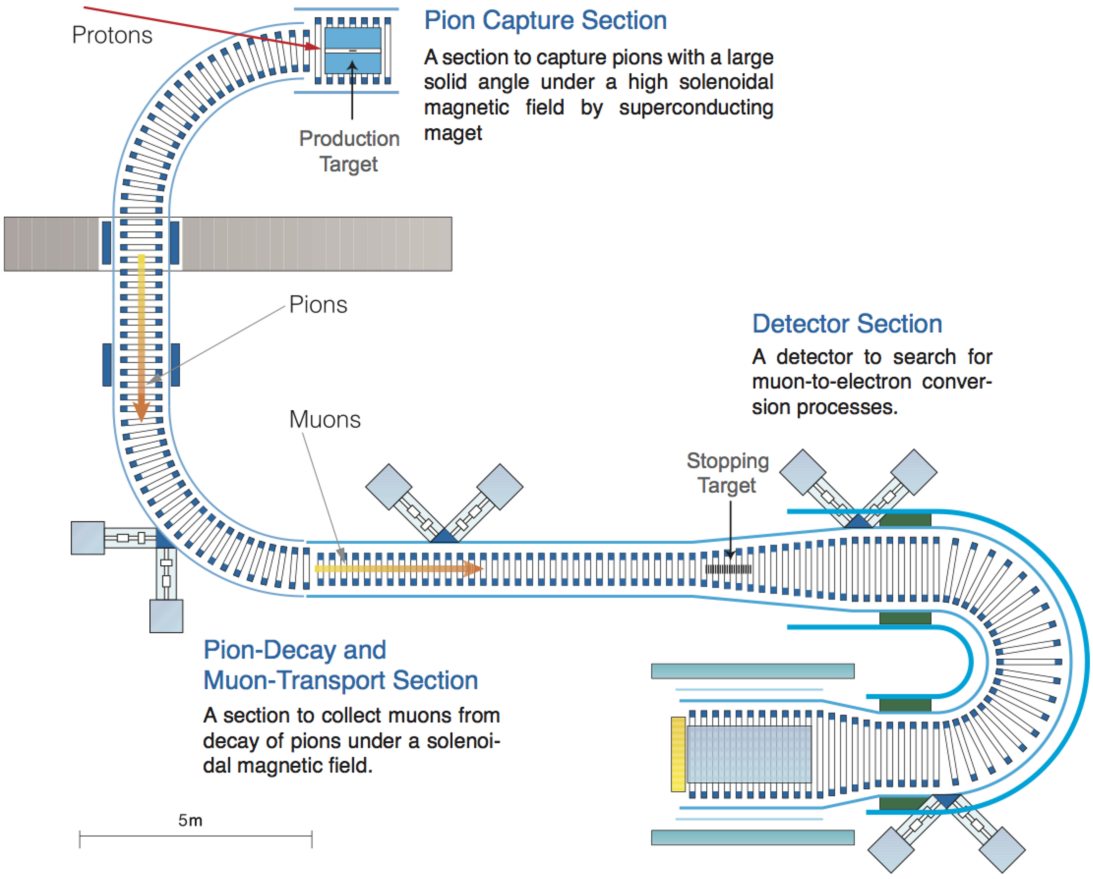

Figure 2.6: Schematic layout of the COMET beam line.

- being able to select low momentum negative muons with momentum of around 40 MeV/c, and eliminate high momentum muons ($>$ 75 MeV/c), since they can decay in flight and produce spurious signals of $\sim$ 105 MeV electrons.

The selection of charge and momentum is done by the curved solenoids. It is know that, in a curved solenoidal field, the centre of the helical trajectory of a charged particle drifts perpendicularly to the curved plane. The magnitude of the drift is given by:

$$D = \frac{1}{qB}\frac{s}{R}\frac{p_L^2 + \frac{1}{2}p_T^2}{p_L} \tag{2.1}$$

$$= \frac{1}{qB}\frac{s}{R}\frac{p}{2}\left(\cos\theta + \frac{1}{\cos\theta}\right) \tag{2.2}$$

$$= \frac{1}{qB}\theta_{bend}\frac{p}{2}\left(\cos\theta + \frac{1}{\cos\theta}\right), \tag{2.3}$$

where q is the electric charge of the particle; B is the magnetic field at the axis; s and R are the path length and the radius of the curvature; p, p_T and p_L are total momentum, transversal momentum and longitudinal momentum of the particles, respectively; $\theta = \mathrm{atan}(p_T/p_L)$ is the pitch angle of the helical trajectory; and $\theta_{bend} = s/R$ is called the bending angle. It is clear that D is proportional to θ_{bend}, to total momentum p. Charged particles with opposite signs move in opposite directions. Therefore it is possible to select muons around 40 MeV/c by using suitable collimator after the curved solenoid.

In order to keep the centre of the helical trajectories of the muons with a reference momentum p_0 in the vertical plane, a compensating dipole field parallel to the drift direction

is needed. In the COMET, the dipole fields are produced by additional coils winded around the solenoid coils. The magnitude of the compensating field is:

$$B_{\mathrm{comp}} = \frac{1}{qR}\frac{p_0}{2}\left(\cos\theta_0 + \frac{1}{\cos\theta_0}\right), \tag{2.4}$$

where the trajectories of charged particles with momentum p_0 and pitch angle θ_0 are corrected to be on-axis. An average dipole field of 0.03 T is needed to select 40 MeV/c muons as required by the COMET design.

2.2.4 Muon stopping target

Muon stopping target is place at 180° bending after the pion production target (figure 2.6) in its own solenoid. The target is designed to maximise the muon stopping efficiency and minimise the energy loss of signal electrons.

It is calculated that the branching ratio of $\mu-e$ conversion increases with atomic number Z, and plateaus above $Z \simeq 30$, then decreases as $Z > 60$ (see figure 2.7). Although the sensitivity is better for higher Z material, the acceptance of the measurement time window decreases quickly because the average lifetime of negative muons inside a material decreases as Z^{-4}. Therefore, light material is preferable as muon stopping target.

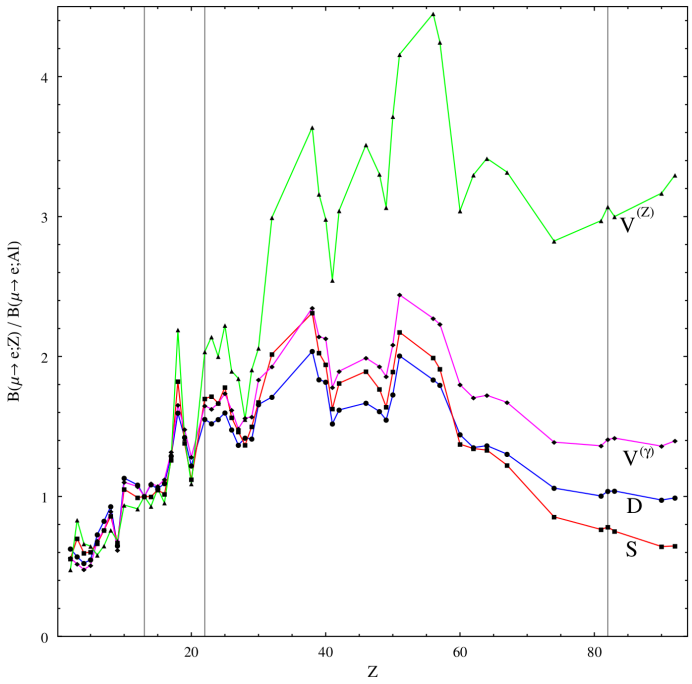

Figure 2.7: Target dependence of the $\mu-e$ conversion rate in different models calculated by Cirigliano and colleagues [31]. The conversion rates are normalised to the rate in aluminium. Four models were considered and noted with letters: D for dipole-interaction-dominated model, V for vector and S for scalar interactions. The three vertical lines from left to right correspond to $Z = 13$(Al), $Z = 22$(Ti), and $Z = 82$(Pb) respectively. Reprinted figure from reference [31]. Copyright 2009 by the American Physical Society.

The first choice for the muon stopping target material in the COMET is aluminium. A titanium target is also considered in the future. Configuration of the target is shown in table 2.3. Monte Carlo studies with this design showed that net stopping efficiency is 0.29, and average energy loss of signal electrons is about 400 keV.

A graded magnetic field (reduces from 3 T to 1 T) is produced at the location of the stopping target (see figure 2.8) to maximise the acceptance for $\mu-e$ conversion signals, since

Item	Specification
Material	Aluminium
Shape	Flat disks
Disk radius	100 mm
Disk thickness	200 µm
Number of disks	17
Disk spacing	50 mm

Table 2.3: Configuration of the muon stopping target.

electrons emitted in the backward direction would be reflected due to magnetic mirroring. The graded field also helps optimising the transmission efficiency to the subsequent electron transport section.

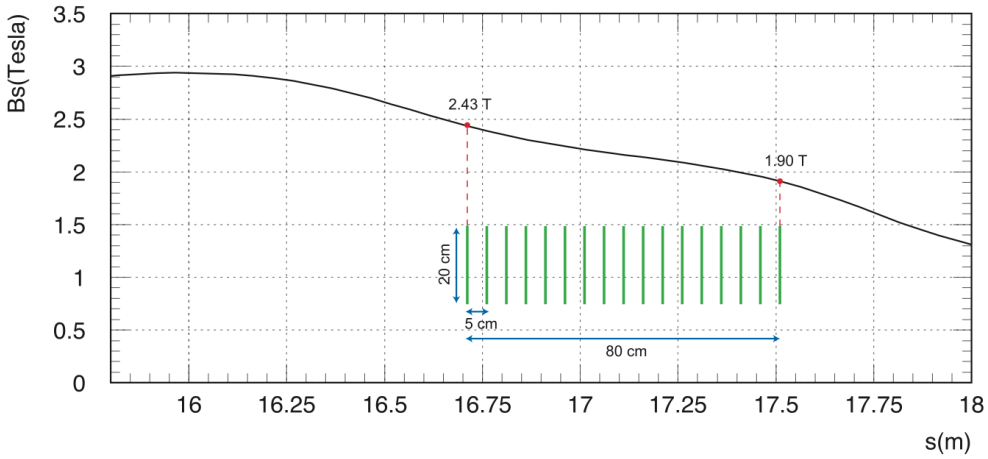

Figure 2.8: The graded magnetic field near the stopping target region.

2.2.5 Electron transportation beam line

The 180° bending electron transport solenoids help remove line-of-sight between the target and the detector system. It works similarly to the muon transportation section, but is tuned differently to accept electrons of about 105 MeV/c. A compensation field of 0.17 T along the vertical direction will be applied. Electrons with momentum less than 80 MeV/c are blocked at the exit of this section by a collimator to reduce DIO electrons rate. The net acceptance of signals of $\mu - e$ conversion is about 0.32, and the detector hit rate will be in the order of 1 kHz for a muon stopping rate of 10^{11} Hz.

2.2.6 Electron detectors

The $\mu - e$ conversion signal electrons is measured by an electron detector system, which consists of straw-tube trackers and an electromagnetic calorimeter - shown in figure 2.9. The requirements for the detector system is to distinguish electrons from other particles, and measure their momenta, energy and timings. The whole detector system is in a uniform solenoidal magnetic field under vacuum. Passive and active shielding against cosmic rays is considered.

The tracking detector has to provide a momentum resolution less than 350 keV/c in order to achieve a sensitivity of 3×10^{-17} . There are five stations of straw-tube gas chambers,

each provides two dimensional information. Each straw tube is 5 mm in diameter and has a 25-µm-thick wall. According to a GEANT4 Monte Carlo simulation, a position resolution of 250 µm can be obtained, which is enough for 350 keV/c momentum resolution. The DIO background of 0.15 events is expected.

The electromagnetic calorimeter serves three purposes: a) to measure electrons energy with high energy resolution; b) to provide timing information and trigger timing for the detector system; and c) to provide additional data on hit positions. Two candidate crystals, GSO and LYSO, are under consideration.

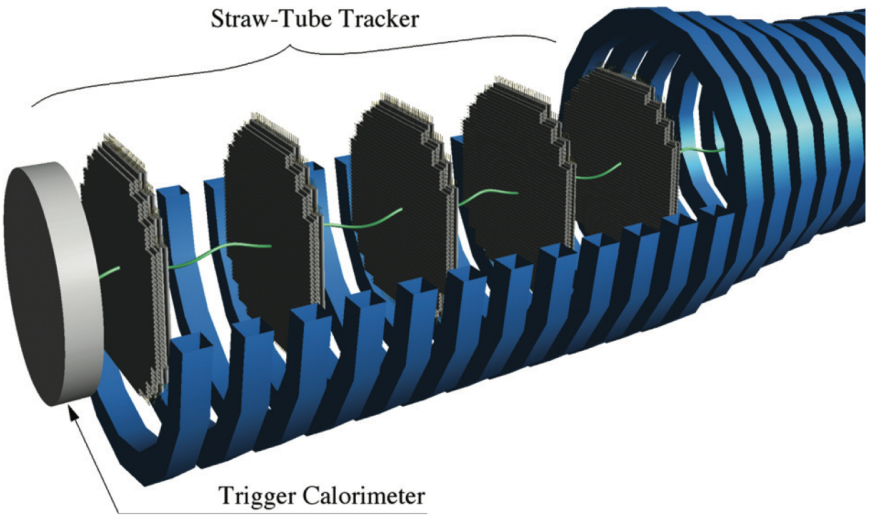

Figure 2.9: Layout of the electron detectors.

The requirements for $\mu - e$ conversion signals are:

- from the 350 keV/c momentum resolution, the signal region is determined to be 103.5 MeV/c to 105.2 MeV/c;
- transversal momentum of signal electrons is required to be greater than 52 MeV/c to remove backgrounds from beam electrons and muons decay in flight;
- timing wise, conversion electrons should arrive in the time window of detection which is about 700 ns after each proton pulses (figure 2.10). The acceptance in this detection window is about 0.39 for aluminium.

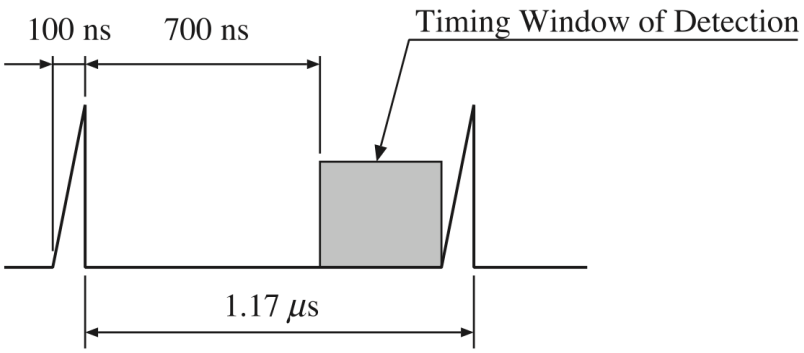

Figure 2.10: Timing window of detection.

2.2.7 Signal sensitivity and background estimation

The single event sensitivity (SES) of the $\mu - e$ conversion search is defined as:

$$\mathcal{B}(\mu^- Al \to e^- Al) = \frac{1}{N_\mu^{\text{stop}} \cdot f_{\text{cap}} \cdot A_e} \tag{2.5}$$

where N_μ^{stop} is the number of muons stopping in the muon target; f_{cap} is the fraction of captured muons; and A_e is the detector acceptance. The total number of stopped muons is projected as $N_\mu^{\text{stop}} = 2 \times 10^{18}$ for a 2×10^7 s run time; $f_{\text{cap}} = 0.61$ for aluminium; and the total acceptance for the COMET detector system is $A_e = 0.031$. Using these numbers, the SES of the COMET is calculated to be 2.6×10^{-17} . The 90% CL upper limit is given by $2.3 \times \mathcal{B}$:

$$\mathcal{B}(\mu^- Al \to e^- Al) < 6 \times 10^{-17} \quad (90\% \text{ C.L.}) \tag{2.6}$$

Potential backgrounds for the COMET are:

1. Intrinsic physics backgrounds: originates from muons stopped in the stopping target, including muon decays in orbit, radiative muon capture and particles such as protons and neutrons emitted after muon capture;

2. Beam related backgrounds: caused by particles (electrons, pions, muons and antiprotons) in the beam. They are either prompt or late-arriving. A beam pulsing with high proton extinction factor is required to reject this type of backgrounds;

3. Accidental background from cosmic rays

The expected background rates for the COMET at an SES of 3×10^{-17} is summarised in table 2.4.

Background	**Events**
Radiative pion capture	0.05
Beam electrons	<0.1
Muon decay in flight	<0.0002
Pion decay in flight	<0.0001
Neutron induced	0.024
Delayed pion radiative capture	0.002
Antiproton induced	0.007
Muon decay in orbit	0.15
Radiative muon capture	<0.001
Muon capture with neutron emission	<0.001
Muon capture with proton emission	<0.001
Cosmic ray muons	0.002
Electron cosmic ray muons	0.002
Total	0.34

Table 2.4: Backgrounds of the COMET experiment.

2.3 The COMET Phase-I

The techniques of beam pulsing and curved solenoids that the COMET will utilise are believed to greatly reduce potential backgrounds, by several orders of magnitude, for the

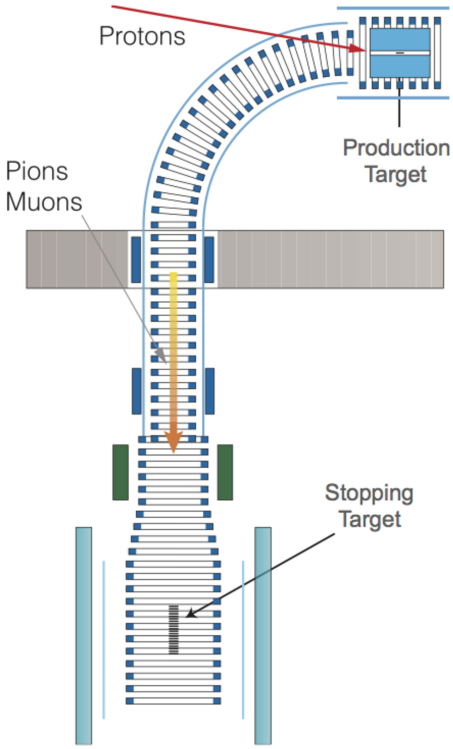

Figure 2.11: Layout of the COMET Phase-I, the target and detector solenoid are placed after the end of the first 90° bend.

$\mu - e$ conversion search. That also means that backgrounds are being extrapolated over four orders of magnitude from existing data. In order to obtain data-driven estimates of backgrounds, and inform the detailed design for the ultimate COMET experiment, a staged approach is desirable. Also, the KEK/J-PARC 5-year mid-term plan from 2013 includes the construction of the COMET beam line. For these reasons, the COMET collaboration considers to carry out the experiment in two stages. The first stage, so called COMET Phase-I, with a shorter muon transportation solenoid, up to the first 90°.

The COMET Phase-I has two major goals:

1. Direct measurements of the proton extinction factor, and other potential backgrounds for the full COMET experiment. These include backgrounds due to beam particles such as pions, neutrons, antiprotons, photons and electrons; and physics background from muon DIO. Straw tube trackers and crystal calorimeter with the same technology in the full COMET will be used, thus these detectors can be regarded as the final prototype.

2. Search for $\mu - e$ conversion with an intermediate single event sensitivity of 3.1×10^{-15}, a two orders of magnitude improvement from the SINDRUM-II limit. Another dedicated detector system (described in section 2.3.3) is considered for this physics measurement.

2.3.1 Proton beam for the COMET Phase-I

Proton beam for the Phase-I differs only in beam power compares to that of the full COMET. It is estimated that a beam power of 3.2 kW = 8 GeV × 0.4 μA (or 2.5×10^{12} protons per second) will be enough for beam properties study and achieving the physics goal of this stage. Starting from a lower intensity is also suitable for performing accelerator studies that are needed to realise 8 GeV beam extraction from the J-PARC main ring.

2.3.2 Pion production and transportation solenoids

Since the beam power will be lower, it is proposed to use a graphite target in the Phase-I. This will minimise the activation of the target station and heat shield which will be easier for necessary upgrading for Phase-II operation. A target length of 600 mm (1.5 radiation length) and target radius of 20 mm are chosen. The target is located at the centre of the pion capture solenoid where the peak magnetic field of 5 T is achieved. A correction dipole filed of 0.05 T is also applied to improve the pion yield.

The pion/muon beam line for COMET Phase-I consists of the pion capture solenoid section (CS), muon transport solenoid section (TS) up to the first 90° bending, and a set of matching solenoids (see figure 2.12). At the end of the muon beam line, the detectors and the detector solenoid (DS) are installed. To reduce beam backgrounds, a beam collimator is placed upstream of the detector solenoid.

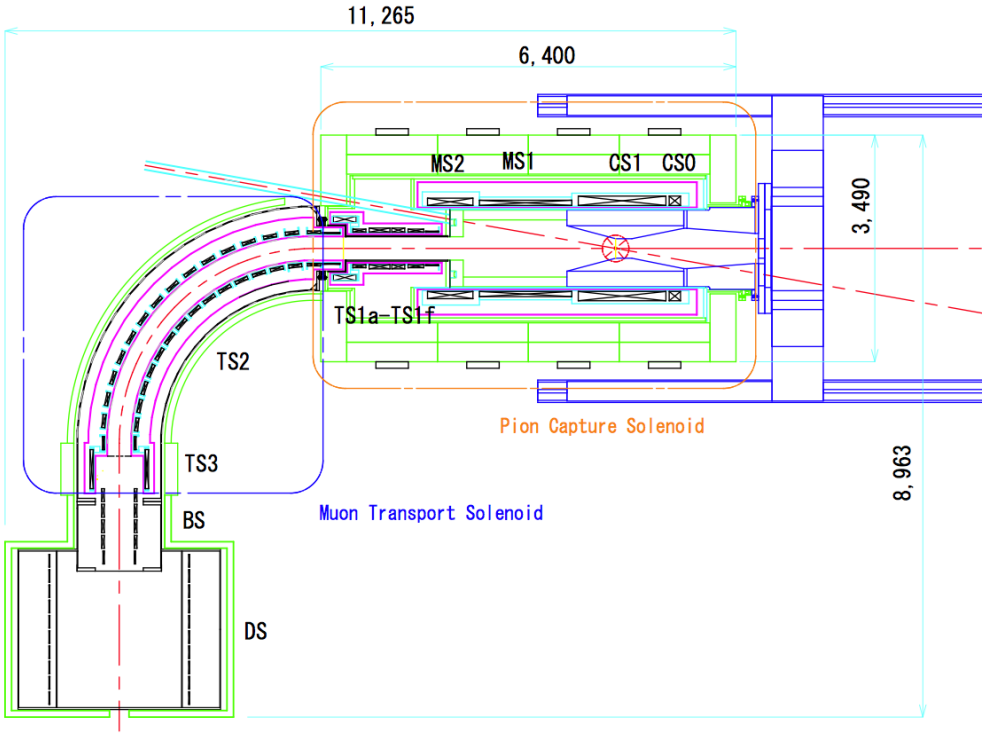

Figure 2.12: A schematic view of the superconducting solenoid magnet system for the COMET Phase-I. Prefix CS is for capture solenoids, MS is for matching solenoids, and TS is for transport solenoids. BS and DS are beam collimation system and detector solenoid, respectively.

2.3.3 Detectors for $\mu - e$ conversion search in the Phase-I

As mentioned, two types of detectors are considered for physics measurements in the Phase-I. The dedicated detector system consists of a cylindrical drift chamber (CDC), a trigger hodoscope, a proton absorber and a detector solenoid (figure 2.13). The whole system is referred as cylindrical detector system (CyDet) in the COMET's documentation. The CyDet has advantages that low momentum particles for the stopping target will not reach the detector, thus the hit rates are kept manageable even at high beam currents. Furthermore, the majority of beam particles, except those scattering at large angles, will not directly hit the CyDet.

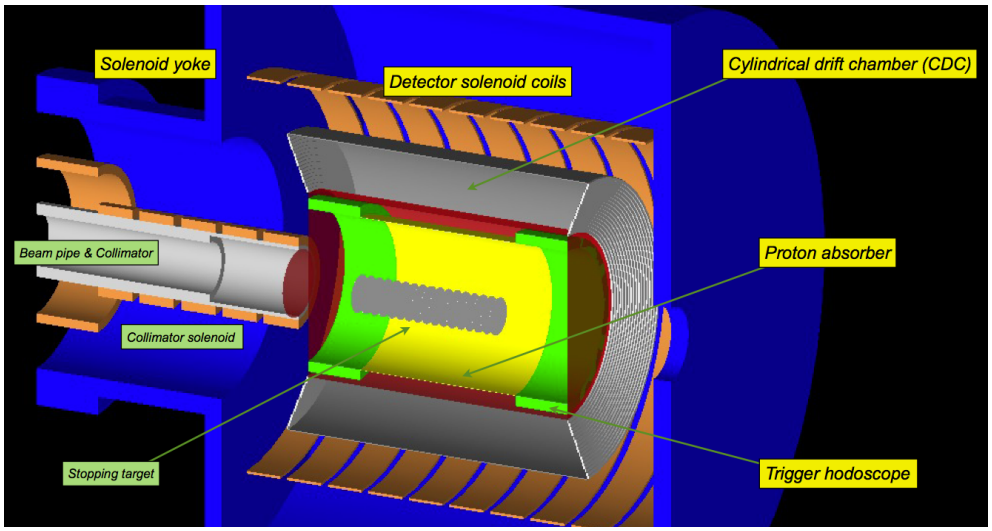

Figure 2.13: Schematic layout of the CyDet.

CDC configuration

The CDC is the main tracking detector that provides information for reconstruction of charged particle tracks and measuring their momenta. The key parameters for the CDC are listed in the table 2.5. Trigger hodoscopes are placed at both upstream and downstream ends of the CDC. A proton absorber is placed concentrically with respect to the CDC axis to reduce potential high rates caused by protons emitted after nuclear muon capture in the stopping target.

The CDC covers the region from 500 mm to 831 mm in the radial direction. The length of the CDC is 1500 mm. The inner wall is made of a 500-um-thick carbon fibre reinforced plastic (CFRP, density $1.57\,\mathrm{g\,m^{-3}}$). The end-plates will be conical in shape and about 10-mm-thick to support the feedthroughs. The outer wall is made of 5-mm CFRP.

The CDC is arranged in 20 concentric sense layers with alternating positive and negative stereo angles. The sense wires are made of gold-plated tungsten, 25 µm in diameter, tensioned to 50 g. The field wires are uncoated aluminium wires with a diameter of 80 µm, at the same tension of 50 g. A high voltage of $1700 \sim 1900$ V will be applied to the sense wires with the field wires at ground potential, giving an avalanche gain of approximately 4×10^4 . A gas mixture of helium:isobutane(90:10) is preferred since the CDC momentum resolution is dominated by multiple scattering. With these configurations, an intrinsic momentum resolution of 197 keV/c is achievable according to our tracking study.

Hit rate on the CDC

The maximal usable muon beam intensity will be limited by the detector hit occupancy. Charge particles with transversal momentum greater than 70 MeV/c are expected to reach the CDC. Those include: protons emitted from nuclear muon capture, and electrons from muon decay in orbit (DIO). It is calculated that the hit rate due to proton emission dominates, where the highest rate is 11 kHzcell compares to 5 kHzcell contributing from DIO electrons. Another potential issue caused by protons is the ageing effect on the CDC as they leave about a 100 times larger energy deposit than the minimum ionisation particles.

For those reasons, we plan to install a proton absorber to reduce the rate of protons reaching the CDC. However, there is no experimental data available for the rate of protons emitted after muon capture in aluminium. In the design of the COMET Phase-I, we use a conservative estimation of the rate of protons from energy spectrum of charged particles

Inner wall	Length	1500 mm
	Radius	500 mm
Outer wall	Length	1740.9 mm
	Radius	831 mm
Sense wire	Number of layers	20
	Material	Gold-plated tungsten
	Diameter	30 µm
	Number of wires	4986
	Tension	50 g
Field wire	Material	Aluminium
	Diameter	80 µm
	Number of wires	14562
	Tension	50 g
Gas		Helium:Isobutane (90:10)

Table 2.5: Main parameters of the CDC for the COMET Phase-I.

emitted from muon capture in ^{28}Si [32]. The baseline design for the proton absorber is 0.5 mm-thick CFRP, making the total thickness of material before the sensitive region is 1.0 mm in CFRP. In this configuration, the inner wall and the proton absorber contribute a spread of 167 keV/c to the momentum of a $\mu - e$ conversion signal electron. This figure is a little below the spread cause by multiple scatterings on the chamber gas at 197 keV/c. The impact of the proton absorber on the CDC's hit rate and momentum resolution is summarised in table 2.6.

Absorber thickness (mm)	**Total CFRP thickness** (mm)	**Proton hit rate** (kHz)	Δp (keV/c)
0	0.5	130	131
0.5	1.0	34	167
1.0	1.5	11	195
1.5	2.0	6	252

Table 2.6: Hit rates and contributions to momentum spread of the proton absorber and inner wall of the CDC. The resolutions are calculated for mono-energetic electrons of 104.96 MeV/c.

In order to obtain a better understanding of the protons emission, and then further optimisation of the CDC, a dedicated experiment to measure proton emission rate and energy spectrum is being carried out at PSI. This experiment is described in detail in next chapters.

It should be noted that the proton hit rate is not a problem for the COMET Phase-II where the additional electron transport solenoid would removed all protons emitted.

2.3.4 Sensitivity of the $\mu - e$ conversion search in the Phase-I

The SES for the Phase-I is given by the (2.5). Using $N_\mu = 1.3 \times 10^{16}$, $f_{\rm cap} = 0.61$, and $A_e = 0.043$ from MC study for the Phase-I, the SES becomes:

$$\mathcal{B}(\mu^- Al \to e^- Al) = 3.1 \times 10^{-15} \tag{2.7}$$

2.3.5 Time line of the COMET Phase-I and Phase-II

We are now in the construction stage of the COMET Phase-I, which is planned to be finished in the middle of 2016. We will carry out engineering run in the second half of 2016, and subsequently, physics run in 2017. A beam time of 90 days is expected to achieve the goal sensitivity of the Phase-I. An anticipated schedule for the COMET, both Phase-I and Phase-II, is shown in figure 2.14.

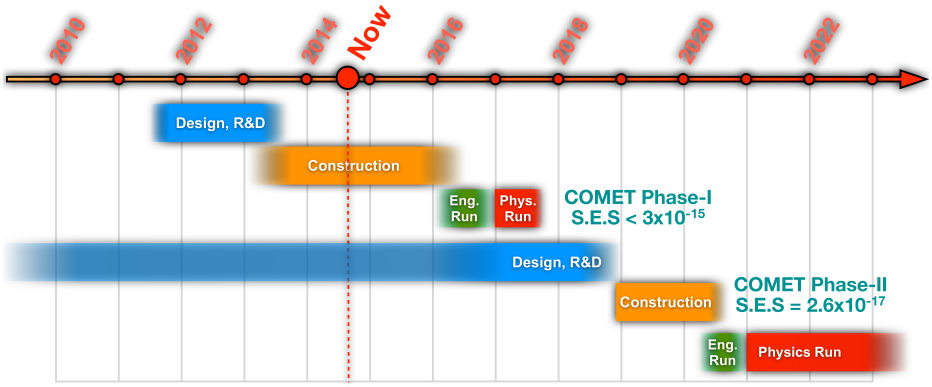

Figure 2.14: The anticipated schedule of the COMET experiment.

Chapter 3

Proton emission following nuclear muon capture and the AlCap experiment

As mentioned earlier, the emission rate of protons following nuclear muon capture on aluminium is of interest to the COMET Phase-I since protons could cause a very high hit rate on the proposed cylindrical drift chamber. Another $\mu - e$ conversion experiment, namely Mu2e at Fermilab, which aims at a similar goal sensitivity as that of the COMET, also shares the same interest on proton emission. Therefore, a joint COMET-Mu2e project was formed to carry out the measurement of proton, and other charged particles, emission. The experiment, so-called AlCap, has been proposed and approved to be carried out at PSI in 2013 [33]. In addition to proton emission, the AlCap experiment will also measure:

- neutron emission, because neutrons could cause backgrounds on the other detectors and damage the front-end electronics; and
- photon emission to validate the normalisation number of stopped muons in the stopping target.

The emission of particles following muon capture in nuclei has been studied thoroughly for several nuclei in the context of "intermediate energy nuclear physics" where it is postulated that the weak interaction is well understood and muons are used as an additional probe to investigate the nuclear structure [34, 35]. Unfortunately, the proton emission rate for aluminium in the energy range of interest has not been measured. This chapter reviews the current knowledge on emission of particles with emphasis on proton.

3.1 Atomic capture of the negative muon

Theoretically, the capturing process can be described in the following stages [36, 37]:

1. High to low (a few keV) energy: the muon velocity are greater than the velocity of the valence electrons of the atom. Slowing down process is similar to that of fast heavy charged particles. It takes about 10^{-10} s to 10^{-9} s to slow down from a relativistic 10^8 eV energy to 2000 eV in condensed matter, and about 1000 times as long in air.
2. Low energy to rest: in this phase, the muon velocity is less than that of the valence electrons, the muon is considered to be moving inside a degenerate electron gas. The muon rapidly comes to a stop either in condensed matters ($\simeq 10^{-13}$ s) or in gases ($\simeq 10^{-9}$ s).

3. Atomic capture: when the muon has no kinetic energy, it is captured by a host atom into one of high orbital states, forming a muonic atom. The distribution of initial states is not well known. The details depend on whether the material is a solid or gas, insulator or metal.

4. Electromagnetic cascade: since all muonic states are unoccupied, the muon cascades down to states of low energy. The transition is accompanied by the emission of Auger electrons or characteristic X-rays, or excitation of the nucleus. The time taken for the muon to enter the lowest possible state, 1S, from the instant of its atomic capture is $\sim 10^{-14}$ s.

5. Muon disappearance: after reaching the 1S state, the muons either decays or gets captured by the nucleus. The possibility to be captured effectively shortens the mean lifetime of negative muons stopped in a material. In hydrogen, the capture to decay probability ratio is about 4×10^{-4} . Around $Z = 11$, the capture probability is roughly equal to the decay probability. In heavy nuclei ($Z \geq$), the ratio of capture to decay probabilities is about 25.

   The K-shell muon will be $m_\mu/m_e \simeq 207$ times nearer the nucleus than a K-shell electron. The close proximity of the K-shell muon in the Coulomb field of a nuclear, together with its weak interaction with the nucleus, allows the muon to spend a significant fraction of time (10^{-7} – 10^{-6} s) within the nucleus, serving as an ideal probe for the distribution of nuclear charge and nuclear moments.

3.2 Nuclear capture of the negative muon

The nuclear capture process is written as:

$$\mu^- + A(N, Z) \rightarrow A(N, Z-1) + \nu_\mu \,. \tag{3.1}$$

The resulting nucleus can be either in its ground state or in an excited state. The reaction is manifestation of the elementary ordinary muon capture on the proton:

$$\mu^- + p \rightarrow n + \nu_\mu \,. \tag{3.2}$$

If the resulting nucleus at is in an excited state, it could cascade down to lower states by emitting light particles and gamma rays, leaving a residual heavy nucleus. The light particles are mostly neutrons and (or) photons. Neutrons can also be directly knocked out of the nucleus via the reaction (3.2). Charged particles are emitted with probabilities of a few percent, and are mainly protons, deuterons and alphas have been observed in still smaller probabilities. Because of the central interest on proton emission, it is discussed in a separated section.

3.2.1 Muon capture on the proton

The underlying interaction in proton capture in (3.2) at nucleon level and quark level are depicted in figure 3.1. The direction of time is from the left to the right hand side, as an incoming muon and an up quark exchange a virtual W boson to produce a muon neutrino and a down quark, hence a proton transforms to a neutron.

The four-momentum transfer in the interaction is fixed at

$$q^2 = (q_n - q_p)^2 = -0.88 m_\mu^2 \ll m_W^2 \,. \tag{3.3}$$

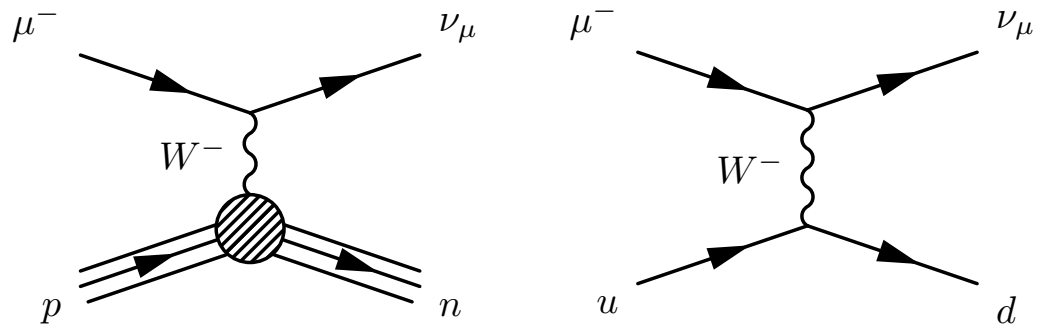

Figure 3.1: A tree-level Feynman diagram of muon capture on the proton, at the nucleon-level (left), and at the quark-level (right).

The smallness of the momentum transfer in comparison to the W boson's mass makes it possible to treat the interaction as a four-fermion interaction with Lorentz-invariant transition amplitude:

$$\mathcal{M} = \frac{G_F V_{ud}}{\sqrt{2}} J^\alpha j_\alpha \tag{3.4}$$

where J is the nucleon current $p \to n$, and j is the lepton current $\mu \to \nu_\mu$, G_F is the Fermi coupling constant, and V_{ud} is the matrix element of the Cabibbo-Kobayashi-Maskawa (CKM) matrix. The lepton current is expressed as a purely $V-A$ coupling of lepton states:

$$j_\alpha = i\bar{\psi}_\nu \gamma_\alpha (1-\gamma_5)\psi_\mu \tag{3.5}$$

The weak current of individual quarks is similar to that of leptons with the only modification is an appropriate element of the CKM matrix (V_{ud}, which is factored out in Eq. (3.4)):

$$J^\alpha = i\bar{\psi}_d (1-\gamma_5)\psi_u \tag{3.6}$$

If the nucleon were point-like, the nucleon current would have the same form as in (3.6) with suitable wavefunctions of the proton and neutron. But that is not the case, in order to account for the complication of the nucleon, the current must be modified by six real form factors $g_i(q^2), i = V, M, S, A, T, P$:

$$J_\alpha = i\bar{\psi}_n (V^\alpha - A^\alpha)\psi_p \,, \tag{3.7}$$

$$V^\alpha = g_V(q^2)\gamma^\alpha + i\frac{g_M(q^2)}{2m_N}\sigma^{\alpha\beta}q_\beta + g_S(q^2)q^\alpha \,, \text{ and} \tag{3.8}$$

$$A^\alpha = g_A(q^2)\gamma^\alpha\gamma_5 + ig_T(q^2)\sigma^{\alpha\beta}q_\beta\gamma_5 + \frac{g_P(q^2)}{m_\mu}\gamma_5 q^\alpha, \tag{3.9}$$

where the V^α and A^α are the vector and axial currents, m_μ and m_N are the muon and nucleon mass, respectively. The scaling by the muon and nucleon mass is by convention in Mukhopadhyay's review [38].

Among the six form factors, the so-called second class currents, g_T and g_S, vanish under the symmetry of G-parity, which is the product of charge conjugation and isospin rotation. Experimental limits for non-zero g_T and g_S are not very tight, but are negligible with respect to other uncertainties in muon capture [35].

The vector form factor g_V, and the weak-magnetic form factor g_M are equivalent to the electromagnetic form factors of the nucleon according the conserved vector current (CVC) hypothesis. The values of these couplings are determined from elastic electron-nucleon scattering experiments, then extrapolated to the momentum transfer q^2.

Using $\mu - e$ universality, the axial form factor g_A in this case is related to that of electron as: $(g_A/g_V)^\mu = (g_A/g_V)^e$ at zero momentum transfer. This equality has been checked using

results from muon decay and beta decay experiments. The q^2-dependence of g_A is deducted from neutrino scattering experiments.

The pseudoscalar form factor g_P is determined by measuring the capture rate of the process in Eq. (3.2). However, because of the smallness capture rate in comparison to muon decay rate, and other complications due to muonic molecules $p\mu p$, $d\mu p$ and $t\mu p$, g_P is the least well-defined form factor. Only recently, it is measured with a reasonable precision [39]. The values of the six form factors at $q^2 = -0.88m_\mu^2$ are listed in table 3.1.

Form factor	**Value at** $-0.88m_\mu^2$
g_S	0
g_T	0
g_V	0.976 ± 0.001
g_M	3.583 ± 0.003
g_A	1.247 ± 0.004
g_P	8.06 ± 0.55

Table 3.1: Values of the weak form factors of the nucleon at $q^2 = -0.88m_\mu^2$

3.2.2 Total capture rate

The captured muon at the 1S state has only two choices, either to decay or to be captured on the nucleus. Thus, the total capture rate for negative muon, Λ_t is given by:

$$\Lambda_t = \Lambda_c + Q\Lambda_d \tag{3.10}$$

where Λ_c and Λ_d are partial capture rate and decay rate, respectively, and Q is the Huff factor, which is corrects for the fact that muon decay rate in a bound state is reduced because of the binding energy reduces the available energy. The correction begins to be significant for $Z \geq 40$ as shown in table 3.2.

Theoretically, it is assumed that the muon capture rate on a proton of the nucleus depends only on the overlap of the muon with the nucleus. For light nuclei where the point nucleus concept is applicable, there are Z protons and the radius of the muon orbital decreases as Z^{-1}, the probability of finding the muon at the radius increases as Z^3, therefore the capture rate increases as Z^4. Because the muon radius soon becomes comparable to that of the nucleus, corrections are needed, so Z_{eff} is used instead of Z.

The effect of the nucleus for higher Z is more profound, there is no theoretical model that provides a satisfied explanation for all experimental data. One simple formula from Primakoff gives a reasonable, and of course not perfect, description of the existing data [35]:

$$\Lambda_c(A, Z) = Z_{\text{eff}}^4 X_1 \left[1 - X_2 \left(\frac{A - Z}{2A}\right)\right] \tag{3.11}$$

where $X_1 = 170\,\text{s}^{-1}$ is the muon capture rate for hydrogen, but reduced because a smaller phase-space in the nuclear muon capture compares to that of a nucleon; and $X_2 = 3.125$ takes into account the fact that it is harder for protons to transforms into neutrons due to the Pauli exclusion principle in heavy nuclei where there are more neutrons than protons.

The total capture rates for several selected elements are compiled by Measday [35], and reproduced in table 3.2.

$Z(Z_{eff})$	**Element**	**Mean lifetime** (ns)	**Capture rate** ($\times 10^{-3}$ ns)	**Huff factor**
1 (1.00)	^{1}H	2194.90(7)	0.450(20)	1.00
	^{2}H	2194.53(11)	0.470(29)	
2 (1.98)	^{3}He	2186.70(10)	2.15(2)	1.00
	^{4}He	2195.31(5)	0.356(26)	
3 (2.94)	^{6}Li	2175.3(4)	4.68(12)	1.00
	^{7}Li	2186.8(4)	2.26(12)	
4 (3.89)	^{9}Be	2168(3)	6.1(6)	1.00
5 (4.81)	^{10}B	2072(3)	27.5(7)	1.00
	^{11}B	2089(3)	23.5(7)	1.00
6 (5.72)	^{12}C	2028(2)	37.9(5)	1.00
	^{13}C	2037(8)	35.0(20)	
7 (6.61)	^{14}N	1919(15)	66(4)	1.00
8 (7.49)	^{16}O	1796(3)	102.5(10)	0.998
	^{18}O	1844(5)	88.0(14)	
9 (8.32)	^{19}F	1463(5)	229(1)	0.998
13 (11.48)	^{27}Al	864(2)	705(3)	0.993
14 (12.22)	^{28}Si	758(2)	868(3)	0.992
20 (16.15)	Ca	334(2)	2546(20)	0.985
40 (25.61)	Zr	110.4(10)	8630(80)	0.940
82 (34.18)	Pb	74.8(4)	12 985(70)	0.844
83 (34.00)	Bi	73.4(4)	13 240(70)	0.840
90 (34.73)	Th	77.3(3)	12 560(50)	0.824
92 (34.94)	U	77.0(4)	12 610(70)	0.820

Table 3.2: Total nuclear capture rate for negative muon in several elements, compiled by Measday [35]

3.2.3 Neutron emission

The average number of neutrons emitted per muon capture generally increases with Z, but there are large deviations from the trend due to particular nuclear structure effects. The trend is shown in table 3.3 and can be expressed by a simple empirical function $n_{avg} = (0.3 \pm 0.02)A^{1/3}$ [34].

The neutron emission can be explained by several mechanisms:

1. Direct emission follows reaction (3.2): these neutrons have fairly high energy, from a few MeV to as high as 40–50 MeV.

2. Indirect emission through an intermediate compound nucleus: the energy transferred to the neutron in the process (3.2) is 5.2 MeV if the initial proton is at rest, in nuclear environment, protons have a finite momentum distribution, therefore the mean excitation energy of the daughter nucleus is around 15 to 20 MeV [38]. This is above the nucleon emission threshold in all complex nuclei, thus the daughter nucleus can de-excite by emitting one or more neutrons. In some actinide nuclei, that excitation energy might trigger fission reactions. The energy of indirect neutrons are mainly in the lower range $E_n \leq 10$ MeV with characteristically exponential shape of evaporation process. On top of that are prominent lines might appear where giant resonances occur.

Experimental measurement of neutron energy spectrum is technically hard, and it is difficult to interpret the results. Due to these difficulties, only a few energy spectrum measurements were made, none of them covers the full energy range and mostly at high energy region [35].

Elements	Average number of neutrons per capture
Al	1.262 ± 0.059
Si	0.864 ± 0.072
Ca	0.746 ± 0.032
Fe	1.125 ± 0.041
Ag	1.615 ± 0.060
I	1.436 ± 0.056
Au	1.662 ± 0.044
Pb	1.709 ± 0.066

Table 3.3: Average number of neutrons emitted per muon capture compiled by Measday [35]

3.3 Proton emission

3.3.1 Experimental status

The measurement of charged particle emission is quite difficult and some early measurements with nuclear emulsion are still the best available data. There are two reasons for that:

1. The emission rate is small: the de-excitation of the nucleus through charged particle is possible, but occurs at very low rate compares to neutron emission. The rate is about 15% for light nuclei and reduces to a few percent for medium and heavy nuclei.

2. The charged particles are short ranged: the emitted protons, deuterons and alphas are typically low energy (2 MeV to 20 MeV). But a relatively thick target is normally needed in order to achieve a reasonable muon stopping rate and charged particle statistics. Therefore, emulsion technique is particularly powerful.

The first study was done by Morigana and Fry [40] where 24,000 muon tracks were stopped in their nuclear emulsion which contains silver, bromine AgBr, and other light elements, mainly nitrogen, carbon, hydrogen and oxygen. The authors identified a capture on a light element as it would leave a recoil track of the nucleus. They found that for silver bromide, $(2.2 \pm 0.2)\%$ of the captures produced protons and $(0.5 \pm 0.1)\%$ produced alphas. For light elements, the emission rate for proton and alpha are respectively $(9.5 \pm 1.1)\%$ and $(3.4 \pm 0.7)\%$. Subsequently, Kotelchuk and Tyler [41] had a result which was about 3 times more statistics and in fair agreement with Morigana and Fry (figure 3.2)

Protons with higher energy are technically easier to measure, but because of the much lower rate, they can only be studied at meson facilities. Krane and colleagues [42] measured proton emission from aluminium, copper and lead in the energy range above 40 MeV and found a consistent exponential shape in all targets. The integrated yields above 40 MeV are in the 10^{-4} – 10^{-3} range (see table 3.4), a minor contribution to total proton emission rate.

Their result on aluminium, the only experimental data existing for this target, is shown in figure 3.3 in comparison with spectra from neighbouring elements, namely silicon measured by Budyashov et al. [43] and magnesium measured Balandin et al. [44]. The authors noted aluminium data and silicon data are in reasonable agreement both in the yield and the energy dependence, while magnesium data shows significant drop in intensity. They then suggested the possibility of an interesting nuclear structure dependency that might be at work in this mass range.

The aforementioned difficulties in charged particle measurements could be solved using an active target, just like nuclear emulsion. Sobottka and Wills [32] took this approach when

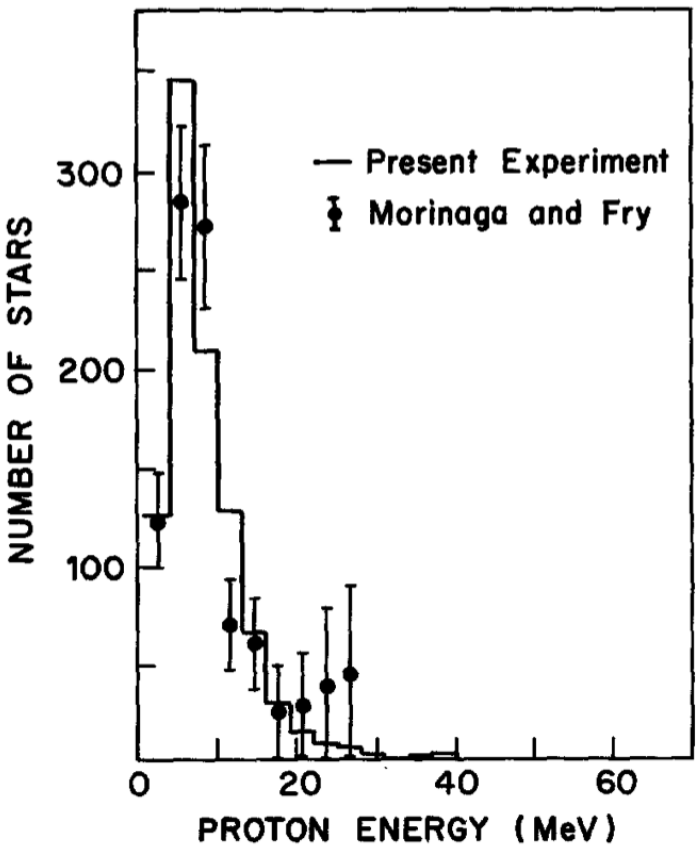

Figure 3.2: Proton spectrum after muon capture in silver bromide AgBr in early experiments recorded using nuclear emulsion. The closed circles are data points from Morigana and Fry [40], the histogram is measurement result of Kotelchuk and Tyler [41]. Reprinted figure from reference [41]. Copyright 1968 by the American Physical Society.

using a Si(Li) detector to stop muons. They obtained a spectrum of charged particles up to 26 MeV in figure 3.4. The peak below 1.4 MeV is due to the recoiling ^{27}Al. The higher energy events including protons, deuterons and alphas constitute $(15 \pm 2)\%$ of capture events, which is consistent with a rate of $(12.9 \pm 1.4)\%$ from gelatine observed by Morigana and Fry. This part has an exponential decay shape with a decay constant of 4.6 MeV. Measday noted [35] the fractions of events in the 26–32 MeV range being 0.3%, and above 32 MeV range being 0.15%. This figure is in agreement with the integrated yield above 40 MeV from Krane et al.

In principle, the active target technique could be applied to other material such as germanium, sodium iodine, caesium iodine, and other scintillation materials. The weak point of this method is that there is no particle identification like in nuclear emulsion, the best one can achieve after all corrections is a sum of all charged particles. It should be noted here deuterons can contribute significantly, Budyashov et al. [43] found deuteron components to be $(34 \pm 2)\%$ of the charged particle yield above 18 MeV in silicon, and $(17 \pm 4)\%$ in copper.

Another technique had been used to study proton emission is the activation method where the residual nucleus is identified by its radioactivity. This method can provide the rate of charged particles emission by adding up the figures from all channels such as $(\mu^-, \nu p)$, $(\mu^-, \nu p(xn))$, $(\mu^-, \nu\alpha)$, $(\mu^-, \nu\alpha(xn))$. The number of elements that can be studied using this method is limited by several requirements: (a) mono-isotopic element is preferable; (b) the radioactive daughter should emit gamma-rays with a reasonable half-life; (c) the $(\mu^-, \nu xn)$

Target	**Exponential constant** E_0 **(MeV)**	**Integrated yield** $E_p \geq 40$ **MeV**
Al	7.5 ± 0.4	$(1.38\pm0.09) \times 10^{-3}$
Cu	8.3 ± 0.5	$(1.96\pm0.12) \times 10^{-3}$
Pb	9.9 ± 1.1	$(0.171\pm0.028)\times 10^{-3}$

Table 3.4: Proton integrated yields and exponential constants measured by Krane et al. [42]. The yields are assumed to be proportional to $\exp(-E/E_0)$.

reactions should lead to either stable daughters, or daughters with very short half-lives. The last condition is important in ensuring the dominating neutron emission processes do not interfere with counting of the much less frequent proton emission reactions.

Vil'gel'mova et al. [45] found the single proton (unaccompanied by any neutron) emission rates in the $^{28}\mathrm{Si}(\mu^-, \nu p)^{27}\mathrm{Mg}$ and $^{39}\mathrm{K}(\mu^-, \nu p)^{38}\mathrm{Cl}$ reactions are (5.3±1.0)% and (3.2±0.6)%, respectively. Singer [34] compared the figure for silicon and the result from active target measurement and found that the reaction $^{28}\mathrm{Si}(\mu^-, \nu pn)^{26}\mathrm{Mg}$ could occur at a similar rate to that of the $^{28}\mathrm{Si}(\mu^-, \nu p)^{27}\mathrm{Mg}$. That also indicates that the deuterons and alphas might constitute a fair amount in the spectrum in figure 3.4.

Wyttenbach et al. [46] studied $(\mu^-, \nu p)$, $(\mu^-, \nu pn)$, $(\mu^-, \nu p2n)$, $(\mu^-, \nu p3n)$ and $(\mu^-, \nu\alpha)$ in a wide range of 18 elements from sodium to bismuth.Their results plotted against the Coulomb barrier for the outgoing protons are given in figure 3.5. The classical Coulomb barrier V they used are given by:

$$V = \frac{zZe^2}{r_0 A^{\frac{1}{3}} + \rho}, \tag{3.12}$$

where z and Z are the charges of the outgoing particle and of the residual nucleus respectively, $e^2 = 1.44\mathrm{MeV} \cdot \mathrm{fm}$, $r_0 = 1.35$ fm, and $\rho = 0$ fm for protons were taken.

Wyttenbach and colleagues saw that the cross section of each reaction decreases exponentially with increasing Coulomb barrier. The decay constant for all $(\mu^-, \nu pxn)$ is about 1.5 per MeV of Coulomb barrier. They also observed a ratio for different de-excitation channels:

$$(\mu^-, \nu p) : (\mu^-, \nu pn) : (\mu^-, \nu p2n) : (\mu^-, \nu p3n) = 1 : 6 : 4 : 4, \tag{3.13}$$

The authors compared their results with many preceded works and rejected the results from Vil'gel'mova et al. [45] as being too high, but Measday [35] noted it it is not necessarily true since there has been suggestion from other experiments that $(\mu^-, \nu p)$ reactions might become more important for light nuclei. Measday noted that the ratio (3.13) holds over a broad range of mass, but below $A = 40$ the $(\mu^-, \nu p)$ reaction can vary significantly from nucleus to nucleus.

3.3.2 Theoretical models

The first attempt to explain the result of Morigana and Fry was done by Ishii [47]. He assumed a two-step scenario: firstly a compound nucleus is formed, and then it releases energy by statistical emission of various particles. Three models for momentum distribution of protons in the nucleus were used: (I) the Chew-Goldberger distribution $\rho(p) \sim A/(B^2 + p^2)^2$; (II) Fermi gas at zero temperature; and (III) Fermi gas at a finite temperature ($kT = 9$ MeV).

A very good agreement with the experimental result for the alpha emission was obtained with distribution (III). However, the calculated emission rate of protons at the same temperature was 10 times smaller the experimental results from Morigana and Fry. The author

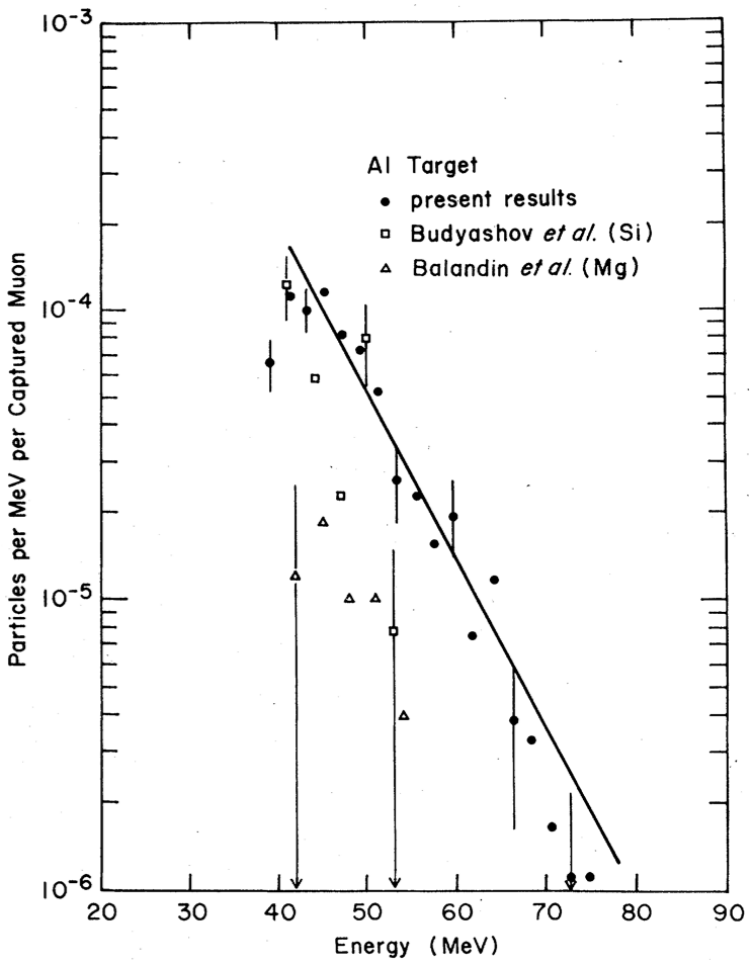

Figure 3.3: Yield of charged particles following muon capture in aluminium target (closed circle) in the energy range above 40 MeV and an exponential fit. The open squares are silicon data from Budyashov et al. [43], the open triangles are magnesium data from Balandin et al. [44]. Reprinted figure from reference [42]. Copyright 1979 by the American Physical Society.

found the distribution (I) is unlikely to be suitable for proton emission, and using that distribution for alpha emission resulted in a rate 15 times larger than the observed rate.

Singer [34] noted that by assuming a reduced effective mass for the nucleon, the average excitation energy increases, but the proton emission rate is not significantly improved and still could not explain the large discrepancy. He concluded that the evaporation mechanism can account for only a small fraction of emitted protons. Moreover, the high energy protons of 25–50 MeV cannot be explained by the evaporation mechanism. He and Lifshitz [48, 49] proposed two major corrections to Ishii's model:

1. A new description of the nucleon momentum in the nucleus with more high momentum components. This helps explaining the high momentum part of the proton spectrum.

2. Pre-equilibrium emission of proton is included: both pre-equilibrium and statistical emission were taken into account. The equilibrium state is achieved through a series of intermediate states, and at each state there is possibility for particles to escape from the nucleus.

With these improvements, the calculated proton spectrum agreed reasonably with data from Morigana and Fry in the energy range $E_p \leq 30$ MeV. Lifshitz and Singer noted

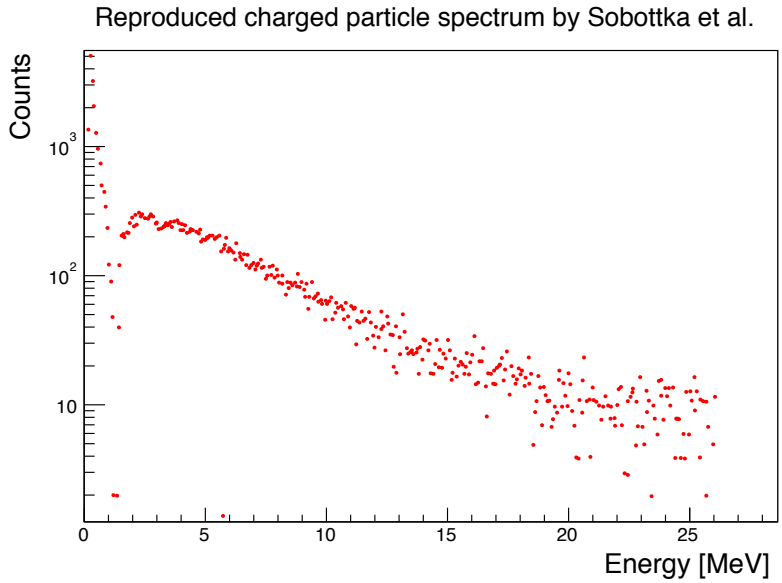

Figure 3.4: Charged particle spectrum from muon capture in a silicon detector, measured by Sobottka and Wills [32]. The plot is reproduced from the original figure in reference [32].

the pre-equilibrium emission is more important for heavy nuclei. Its contribution in light nuclei is about a few percent, increasing to several tens of percent for $100 < A < 180$, then completely dominating in very heavy nuclei. This trend is also seen in other nuclear reactions at similar excitation energies. The pre-equilibrium emission also dominates the higher-energy part, although it falls short at energies higher than 30 MeV. The comparison between the calculated proton spectrum and experimental data is shown in figure 3.6.

The authors found their corrections accounts well for the observed data in a wide range of elements $23 \leq A \leq 209$. They calculated both the single proton emission rate $(\mu^-, \nu p)$ and the inclusive emission rate:

$$\begin{aligned}\sum(\mu^-, \nu p) =&(\mu^-, \nu p) + (\mu^-, \nu pn) + (\mu^-, \nu p2n) \\ &+ \ldots + (\mu^-, \nu d) + (\mu^-, \nu dn)) + \ldots\end{aligned}$$

The deuteron emission channels are included to comparisons with activation data where there is no distinguish between $(\mu^-, \nu pn)$ and (μ^-, d), ... Their calculated emission rates together with available experimental data is reproduced in table 3.5 where a generally good agreement between calculation and experiment can be seen from. The rate of $(\mu^-, \nu p)$ reactions for ^{28}Al and ^{39}K are found to be indeed higher than average, though not as high as Vil'gel'mora et al. [45] observed.

For protons with higher energies in the range of 40–90 MeV observed in the emulsion data as well as in later experiments [42–44], Lifshitz and Singer [50] suggested another contribution from capturing on correlated two-nucleon cluster, an idea that had been proposed earlier by Singer [51]. In this calculation, the authors considered the captures on cluster in which two nucleons interact with each other via meson exchange current. There is experimental evidence that the nuclear surface is reach in nucleon clusters, and it had been shown that the meson exchange current increases the total capture rate in deuterons by 6%. The result of this model was a mix, it accounted well for Si, Mg and Pb data, but predicted rates about 4 times smaller in cases of Al and Cu, and about 10 times higher in case of AgBr (table 3.6).

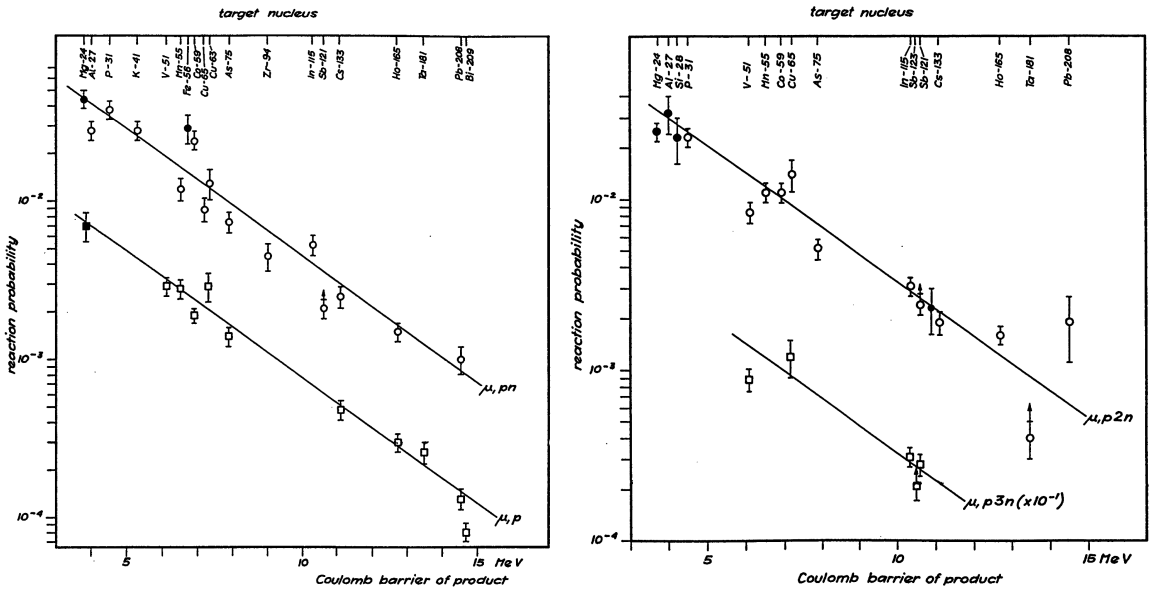

Figure 3.5: Activation results from Wyttenbach and colleagues [46] for the $(\mu^-, \nu p)$, $(\mu^-, \nu pn)$, $(\mu^-, \nu p2n)$ and $(\mu^-, \nu p3n)$ reactions. The cross section of each individual channels decreases exponentially as the Coulomb barrier for proton emission increases. Reprinted figure from reference [46] with permission from Elsevier.

3.3.3 Summary on proton emission from aluminium

There is no direct measurement of proton emission following muon capture in the relevant energy for the COMET Phase-I of 2.5–10 MeV:

1. Spectrum wise, only one energy spectrum (figure 3.3) for energies above 40 MeV is available from Krane et al. [42], where an exponential decay shape with a decay constant of 7.5±0.4 MeV. At low energy range, the best one can get is the charged particle spectrum, which includes protons, deuterons and alphas, from the neighbouring element silicon (figure 3.4). This charged particle spectrum peaks around 2.5 MeV and reduces exponentially with a decay constant of 4.6 MeV.

2. The activation data from Wyttenbach et al. [46] only gives rate of $^{27}\mathrm{Al}(\mu^-, \nu pn)^{25}\mathrm{Na}$ reaction, and set a lower limit for proton emission rate at $(2.8 \pm 0.4)\%$ per muon capture. If the ratio (3.13) holds true for aluminium, then the inclusive proton rate would be 7%, higher than the calculated rate of 4% by Lifshitz and Singer [49]. Both activation technique and inclusive rate calculation do not distinguish between different channels that give the same final state, such as between $^{27}\mathrm{Al}(\mu^-, \nu pn)^{25}\mathrm{Na}$ and $^{27}\mathrm{Al}(\mu^-, \nu d)^{25}\mathrm{Na}$ reactions.

In short, the knowledge on proton emission from aluminium at low energy is limited. The rate estimation does not separate protons from deuterons, and experimentally, there is a lower limit of $(2.8 \pm 0.4)\%$ per muon capture. A spectrum shape at this energy range is not available.

3.4 The AlCap experiment

3.4.1 Motivation of the AlCap experiment

As mentioned, protons from muon capture on aluminium might cause a very high rate in the COMET Phase-I CDC. The detector is designed to accept particles with momenta in the

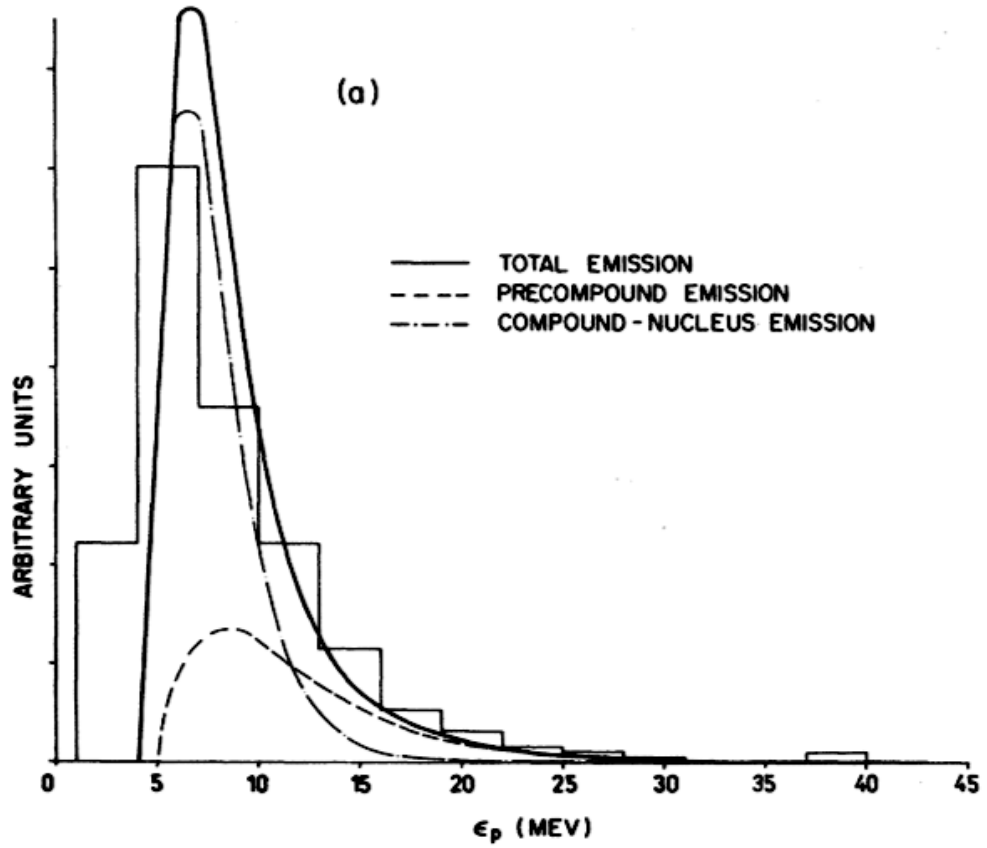

Figure 3.6: Proton energy spectrum from muon capture in AgBr, the data in histogram is from Morigana and Fry, calculation by Lifshitz and Singer [48] showed contributions from the pre-equilibrium emission and the equilibrium emission. Reprinted figure from reference [48]. Copyright 1978 by the American Physical Society.

range of 75 MeV/c to 120 MeV/c. figure 3.7 shows that protons with kinetic energies larger than 2.5 MeV could hit the CDC. Such events are troublesome due to their large energy deposition. Deuterons and alphas at the same momentum are not of concern because they have lower kinetic energy compared with protons and higher stopping power, thus are harder to escape the muon stopping target.

The COMET plans to introduce a thin, low-Z proton absorber in between the target and the CDC to reduce proton hit rate. The absorber will be effective in removing low energy protons. The high energy protons that are moderated by the absorber will fall into the acceptance range of the CDC, but because of the exponential decay shape of the proton spectrum, the hit rate caused by these protons should be affordable.

The proton absorber solves the problem of hit rate, but it degrades the reconstructed momentum resolution. Therefore its thickness and geometry should be carefully optimised. The limited information available makes it difficult to arrive at a conclusive detector design. The proton emission rate could be 4% as calculated by Lifshitz and Singer [49]; or 7% as estimated from the $(\mu^-, \nu pn)$ activation data and the ratio in (3.13); or as high as 15-20% from silicon and neon.

For the moment, design decisions in the COMET Phase-I are made based on conservative assumptions: emission rate of 15% and an exponential decay shape are adopted follow the silicon data from Sobottka and Will [32]. The spectrum shape is fitted with an empirical

Capturing nucleus	$(\mu, \nu p)$ calculation	$(\mu, \nu p)$ experiment	$\Sigma(\mu, \nu p(xn))$ calculation	$\Sigma(\mu, \nu p(xn))$ experiment	Est.
$^{27}_{13}$Al	9.7	(4.7)	40	> 28	(70)
$^{28}_{14}$Si	32	53 ± 10	144	150 ± 30	
$^{31}_{15}$P	6.7	(6.3)	35	> 61	(91)
$^{39}_{19}$K	19	32 ± 6	67		
$^{41}_{19}$K	5.1	(4.7)	30	> 28	(70)
$^{51}_{23}$V	3.7	2.9 ± 0.4	25	$> 20 \pm 1.8$	(32)
$^{55}_{25}$Mn	2.4	2.8 ± 0.4	16	$> 26 \pm 2.5$	(35)
$^{59}_{27}$Co	3.3	1.9 ± 0.2	21	$> 37 \pm 3.4$	(50)
$^{60}_{28}$Ni	8.9	21.4 ± 2.3	49	40 ± 5	
$^{63}_{29}$Cu	4.0	2.9 ± 0.6	25	$> 17 \pm 3$	(36)
$^{65}_{29}$Cu	1.2	(2.3)	11	$> 35 \pm 4.5$	(36)
$^{75}_{33}$As	1.5	1.4 ± 0.2	14	$> 14 \pm 1.3$	(19)
$^{79}_{35}$Br	2.7		22		
$^{107}_{47}$Ag	2.3		18		
$^{115}_{49}$In	0.63	(0.77)	7.2	$> 11 \pm 1$	(12)
$^{133}_{55}$Cs	0.75	0.48 ± 0.07	8.7	$> 4.9 \pm 0.5$	(6.7)
$^{165}_{67}$Ho	0.26	0.30 ± 0.04	4.1	$> 3.4 \pm 0.3$	(4.6)
$^{181}_{73}$Ta	0.15	0.26 ± 0.04	2.8	$> 0.7 \pm 0.1$	(3.0)
$^{208}_{82}$Pb	0.14	0.13 ± 0.02	1.1	$> 3.0 \pm 0.8$	(4.1)

Table 3.5: Probabilities in units of 10^{-3} per muon capture for the reaction $^{A}_{Z}X(\mu, \nu p)^{A-1}_{Z-2}Y$ and for inclusive proton emission compiled by Measday [35]. The calculated values are from Lifshitz and Singer. The experimental data are mostly from Wyttenbach and colleagues [46]. The inclusive emission the experimental figures are lower limits because only a few decay channels could be studied. The figures in crescent parentheses are estimates for the total inclusive rate derived from the measured exclusive channels by the use of ratio in (3.13).

Nucleus	**Experiment**$\times 10^3$	**Calculation**$\times 10^3$
Al	1.38 ± 0.09	0.3
Si	0.87 ± 0.14	0.5
Mg	0.17 ± 0.05	0.2
Cu	1.96 ± 0.12	0.5
AgBr	$(4.7 \pm 1.1) \times 10^{-2}$	0.4
Pb	0.17 ± 0.03	0.3

Table 3.6: Probability of proton emission with $E_p \geq 40\,\mathrm{MeV}$ calculated by Lifshitz and Singer [50] with the two-nucleon capture hypothesis in comparison with available data.

function given by:

$$p(T) = A \left(1 - \frac{T_{th}}{T}\right)^{\alpha} \exp\left(-\frac{T}{T_0}\right), \tag{3.14}$$

where T is the kinetic energy of the proton in MeV, and the fitted parameters are $A = 0.105\ \mathrm{MeV}^{-1}$, $T_{th} = 1.4$ MeV, $\alpha = 1.328$ and $T_0 = 3.1$ MeV. The function rises from the cut-off value of T_{th}, its rising edge is governed by the parameter α. The exponential decay component dominates at higher energy.

The baseline design of the proton absorber for the COMET Phase-I based on above

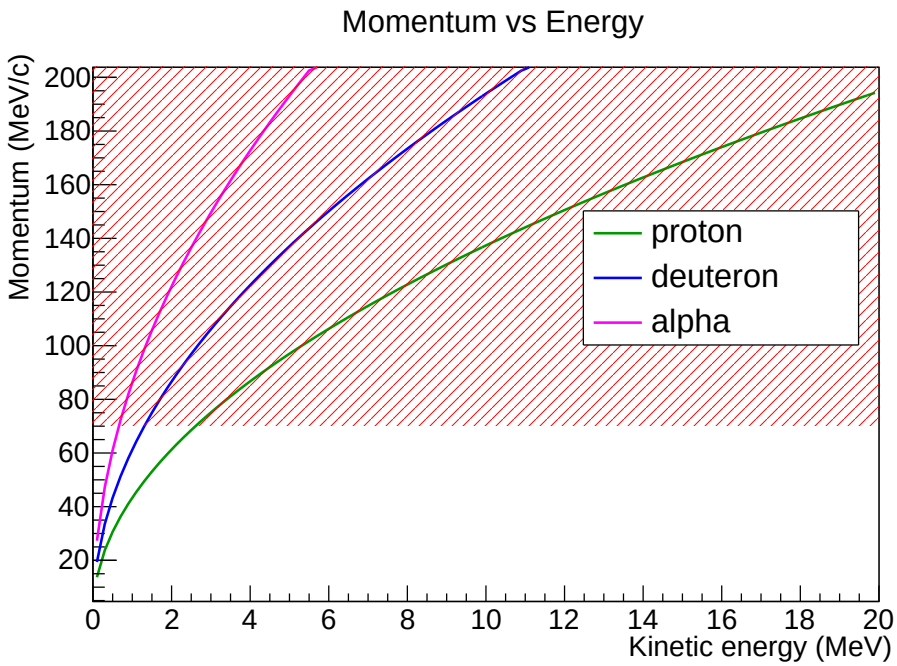

Figure 3.7: Momentum - kinetic energy relation of protons, deuterons and alphas at low energy region below 20MeV. Charged particles in the shaded area could reach the COMET Phase-I's CDC, for protons that corresponds kinetic energies higher than 2.5 MeV. Deuterons and alphas at low energies should be stopped inside the muon stopping target.

assumptions is a 0.5-mm-thick CFRP layer as has been described in section 2.3.3. The hit rate estimation is conservative and the contribution of the absorber to the momentum resolution is not negligible, further optimisation is desirable. Therefore a measurement of the rate and spectrum of proton emission after muon capture is required.

3.4.2 Experimental method for proton measurement

We planned to use a low-energy, narrow-momentum-spread available at PSI to fight the aforementioned difficulties in measuring protons. The beam momentum is tunable from 28 MeV to 45 MeV so that targets at different thickness from 25 µm to 100 µm can be studied. The πE1 beam line could deliver 10^3 muons/s at 1% momentum spread, and 10^4 muons/s at 3% momentum spread. The muon stopping distribution of the muons could be well-tuned using this excellent beam.

Emitting charged particles from nuclear muon capture will be identified by the specific energy loss. Experimentally, the specific energy loss is measured in the AlCap using a pair of silicon detectors: a 65 µm-thick detector, and a 1500 µm-thick detector. Each detector is 5×5 cm^2 in area. The thinner one provides dE information, while the sum energy deposition in the two gives E, if the particle is fully stopped. The silicon detectors pair could help distinguish protons from other charged particles from 2.5 MeV to 12 MeV as shown in figure 3.8.

Two pairs of detectors, placed symmetrically with respect to the target, provide a mean to check for muon stopping distribution inside the target. The absolute number of stopped muons is calculated from the number of muonic X-rays recorded by a germanium detector. For aluminium, the $(2p - 1s)$ line is at 346.828 keV. The acceptances of detectors will be assessed by detailed Monte Carlo study using Geant4.

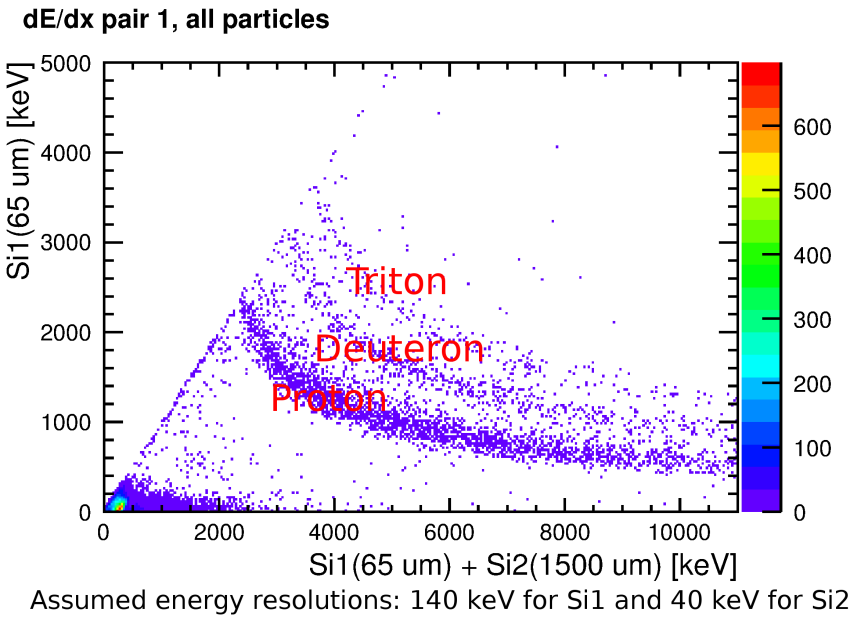

Figure 3.8: Simulation study of PID using a pair of silicon detectors. The detector resolutions follow the calibration results provided by the manufacturer.

3.4.3 Goals and plan of the experiment

The goal of the experiment is measure protons following nuclear muon capture on aluminium:

1. emission rate,
2. and spectrum shape in the lower energy region down to 2.5 MeV,
3. with a precision of about 5%.

The measured proton spectrum and rate will be used to assess the hit rate on the tracking drift chamber of the COMET Phase-I.

The measurement of protons itself is part of the AlCap, where experimental program is organised in three distinct work packages (WP), directed by different team leaders, given in parentheses.

WP1: (P. Kammel (University of Washington), Y. Kuno(Osaka University)) **Charged Particle Emission after Muon Capture.**
Protons emitted after nuclear muon capture in the stopping target dominate the single-hit rates in the tracking chambers for both the Mu2e and COMET Phase-I experiments. We plan to measure both the total rate and the energy spectrum to a precision of 5% down to proton energies of 2.5 MeV.

WP2: (J. Miller(Boston University)) **Gamma and X-ray Emission after Muon Capture.**
A germanium detector will be used to measure X-rays from the muonic atomic cascade, in order to provide the muon-capture normalisation for WP1, and is essential for very thin stopping targets. It is also the primary method proposed for calibrating the number of muon stops in the Mu2e and COMET experiments. Two additional calibration techniques will also be explored; (1) detection of delayed gamma rays from nuclei activated during nuclear muon capture, and (2) measurement of the rate of photons produced in radiative muon decay. The first of these would use a germanium detector and the second a sodium iodine detector. The sodium iodine calorimeter

will measure the rate of high energy photons from radiative muon capture (RMC), electrons from muon decays in orbit (DIO), and photons from radiative muon decay (RMD), as potential background sources for the conversion measurement. As these rates are expected to be extremely low near the conversion electron energy, only data at energies well below 100 MeV will be obtained.

WP3: (E. Hungerford (University of Houston), P. Winter(Argonne National Laboratory))
Neutron Emission after Muon Capture.
Neutron rates and spectra after capture in Al and Ti are not well known. In particular, the low energy region below 10 MeV is important for determining backgrounds in the Mu2e/COMET detectors and veto counters as well as evaluating the radiation damage to electronic components. Carefully calibrated liquid scintillation detectors, employing neutron-gamma discrimination and spectrum unfolding techniques, will measure these spectra. The measurement will attempt to obtain spectra as low or lower than 1 MeV up to 10 MeV.

WP1 was the most developed project in this program with most of the associated apparatus had been built and optimised. Therefore the measurement of proton has been carried out in November and December 2013, while preparing and completing test measurements and simulations to undertake WP2 and WP3.

Chapter 4

The AlCap Run 2013

The first run of the AlCap experiment was performed at the πE1 beam line area, PSI from November 26 to December 23, 2013. The goal of the run was to measure protons rate and their spectrum following muon capture on aluminium.

4.1 Experimental set up

The low energy muons from the πE1 beam line were stopped in thin aluminium and silicon targets, and charged particles emitted were measured by two pairs of silicon detectors inside of a vacuum vessel (figure 4.1). A stopped muon event is defined by a group of upstream detectors and a muon veto plastic scintillator. The number of stopped muons is monitored by a germanium detector placed outside of the vacuum chamber. In addition, several plastic scintillators were used to provide veto signals for the silicon and germanium detectors. Two liquid scintillators for neutron measurements were also tested in this run.

4.1.1 Muon beam and vacuum chamber

Muons in the πE1 beam line are decay products of pions created as a 590 MeV proton beam hits a thick carbon target. The beam line was designed to deliver muons with momenta ranging from 10 MeV/c to 500 MeV/c and momentum spread from 0.26 % to 8.0 % [52]. The beam parameters can be tuned by adjusting magnets and slits along the beam line.

One of the main requirements of the AlCap experiment was a low energy muon beam with narrow momentum bite in order to achieve a high fraction of stopping muons in the very thin targets. In this Run 2013, muons from 28 MeV/c to 45 MeV/c and momentum spread of 1% and 3% were used.

For part of the experiment the target was replaced with one of the silicon detector packages allowed an accurate momentum and range calibration of the beam at the target. Figure 4.2 shows the measured muon rates as a function of momentum for two different momentum bites. Figure 4.3 shows an example of the resulting energy spectra recorded by our silicon detector.

The targets and charged particle detectors are installed inside the vacuum chamber as shown in figure 4.1. The muon beam enters from the right of figure 4.1 and hits the target, which is placed at the centre of the vacuum chamber and orientated at 45 degrees to the beam axis. The side walls and bottom flange of the vessel provide several vacuum-feedthroughs for the high voltage and signal cables for the silicon and scintillator detectors inside the chamber. In addition, the chamber is equipped with several lead collimators to quickly capture muons that do not stop in the actual target.

For a safe operation of the silicon detector, a vacuum of 10^{-4} mbar was necessary. With the help of the vacuum group of PSI, we could consistently reach the required vacuum level

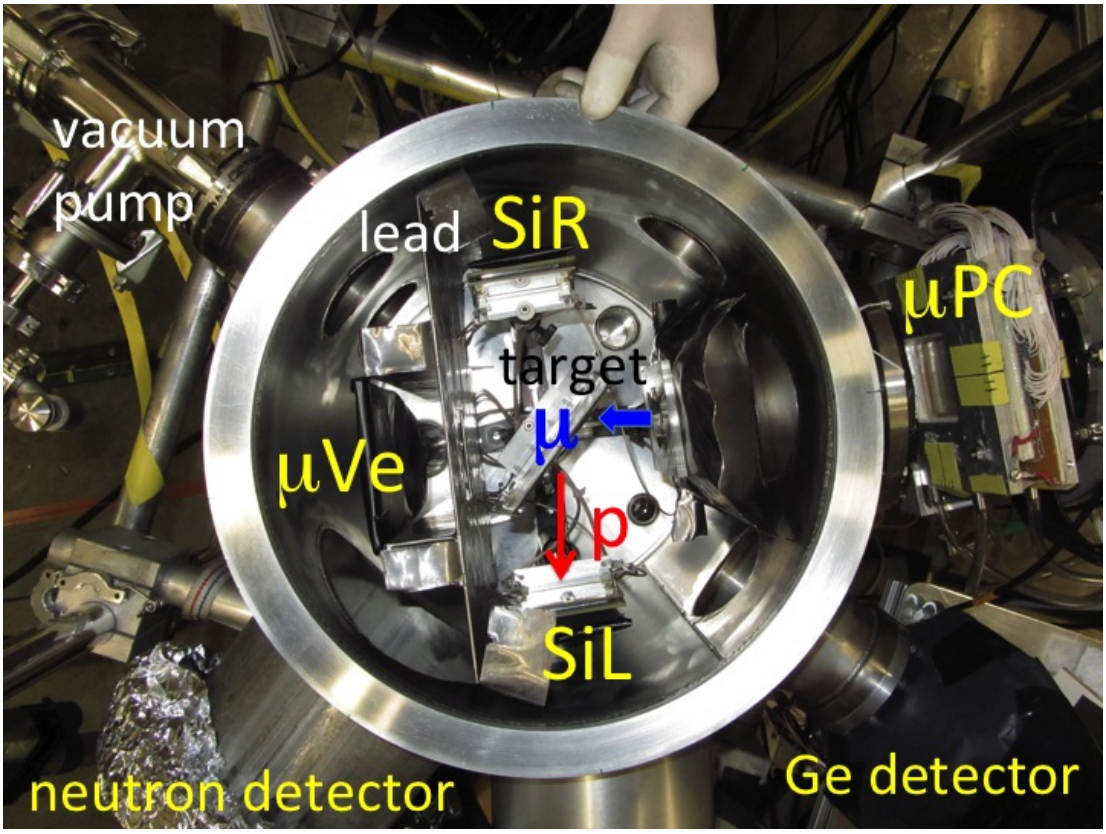

Figure 4.1: AlCap detectors: two silicon packages inside the vacuum vessel, muon beam detectors including plastic scintillators and a wire chamber, germanium detector and veto plastic scintillators.

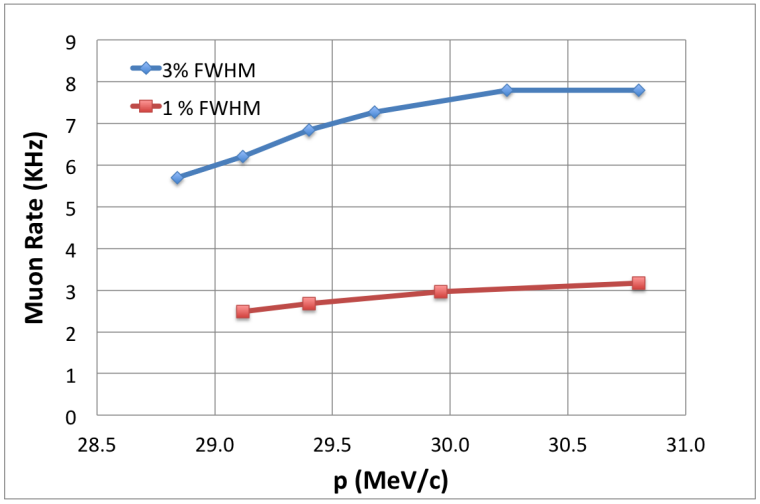

Figure 4.2: Measured muon rates at low momenta during the Run 2013. Beam rates at 1 % FWHM momentum bite were about 3 times smaller than the rates at 3 % FWHM.

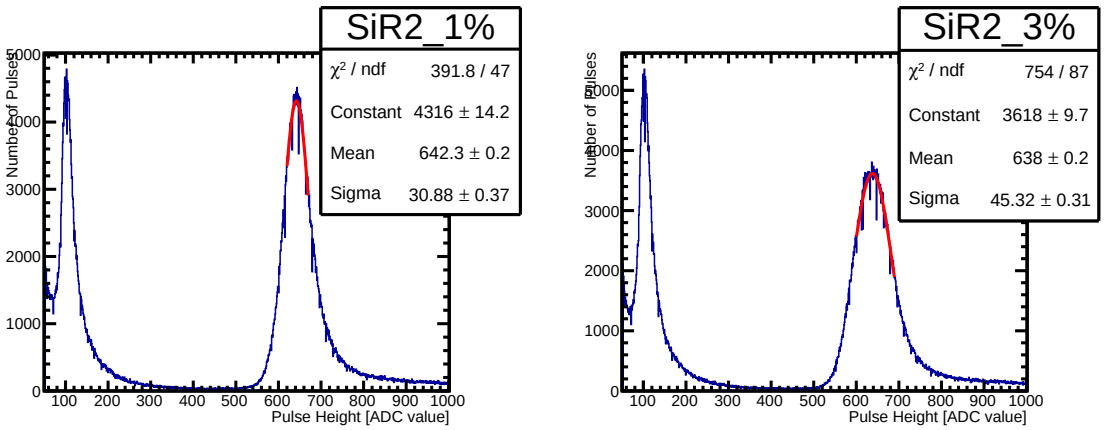

Figure 4.3: Energy deposition at 36.4 /c incident muon beam in an 1500 µm-thick active target. The peak at low energy is due to beam electrons, the peaks at higher energies are due to muons. Momentum bite of 1 and 3% FWHM on left and right hand side, respectively. The electron peak are the same in both plots as beam electrons are minimum ionisation particles and passed though the detector easily. The muon peak at the 3 % FWHM momentum bite is notably broader than that at 1 % FWHM setting.

within 45 minutes after closure of the chamber's top flange.

4.1.2 Silicon detectors

The main detectors for proton measurement in the Run 2013 were four large area silicon detectors. The silicon detectors were grouped into two detector packages located symmetrically at 90 degrees of the nominal muon beam path, SiL and SiR in figure 4.1. Each arm consists of: one ΔE counter, a 65 µm-thick silicon detector, divided into 4 quadrants; one E counter made from 1500 µm-thick silicon; and one plastic scintillator to identify electrons or high energy protons that pass through the silicon. The area of each of these silicon detectors and the scintillators is $50 \times 50\text{mm}^2$. There is a dead layer of 0.5 µm on each side of the silicon detectors according to the manufacturer Micron Semiconductor [1].

The detectors were named according to their positions relative to the muon view: the SiL package contains the thin detector SiL1 and thick detector SiL2; the SiR package has SiR1 and SiR2 accordingly. Each quadrant of the thin detectors were also numbered from 1 to 4, i.e. SiL1-1, SiL1-2, SiL1-3, SiL1-4, SiR1-1, SiR1-2, SiR1-3, SiR1-4.

Bias for the four silicon detectors was supplied by an ORTEC 710 NIM module, which has a vacuum interlock input to prevent biasing before the safe vacuum level has been reached. Typical voltage to fully depleted the detectors were −300 V and −10 V for the thick and thin silicon detectors respectively. The leakage currents at the operating voltages are less than 1.5 µA for the thick detectors, and about 0.05 µA for the thin ones (see figure 4.4).

The fact that a detector were fully depleted was checked by putting a calibration source ^{241}Am at its ohmic side, and observing the output pulse height on an oscilloscope. One would expect that the maximum pulse height increases as the bias is raised until the voltage of fully depleted. The effect can also be seen on the pulse height spectrum as in figure 4.5.

[1] http://www.micronsemiconductor.co.uk/

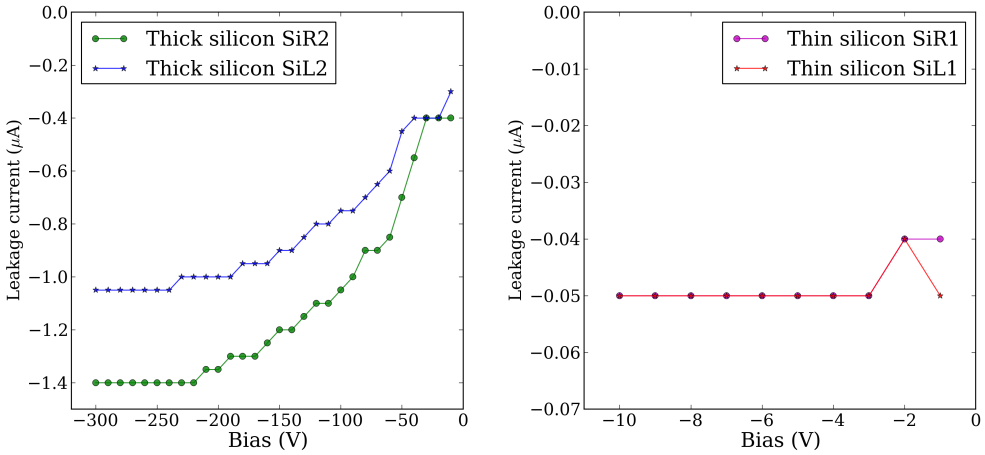

Figure 4.4: Leakage currents of the silicon detectors under bias.

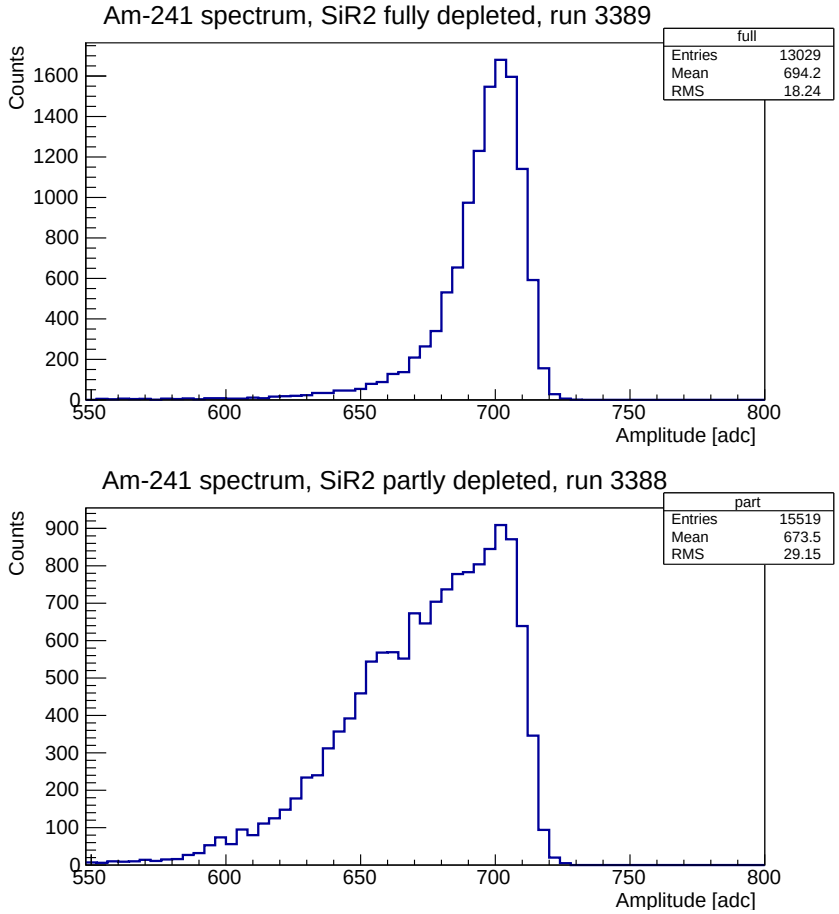

Figure 4.5: ^{241}Am spectra in cases of fully depleted (top), and partly depleted (bottom).

Elements	Transition	Energy	Intensity
^{27}Al	$2p-1s$	346.828 ± 0.002	79.8 ± 0.8
	$3p-1s$	412.87 ± 0.05	7.62 ± 0.15
^{28}Si	$2p-1s$	400.177 ± 0.005	80.3 ± 0.8
	$3p-1s$	476.80 ± 0.05	7.40 ± 0.20

Table 4.1: Reference values of major muonic X-rays from aluminium and silicon.

4.1.3 Upstream counters

The upstream detector consists of three counters: a 500 µm-thick scintillator muon trigger counter (μSC); a muon anti-coincidence counter (μSCA) surrounding the trigger counter with a hole of 35 mm in diameter to define the beam radius; and a multi-wire proportional chamber (μPC) that uses 24 X wires and 24 Y wires at 2 mm intervals.

The upstream detectors provide signal of an incoming muon as coincident hits on the muon trigger and the wire chamber in anti-coincidence with the muon anti-coincidence counter. This set of detectors along with their read-out system belong to the MuSun experiment, which operated at the same beam line just before our run. Thanks to the MuSun group, the detectors were well-tuned and ready to be used in our run without any modification.

4.1.4 Germanium detector

We used a germanium detector to normalise the number of stopped muons by measuring characteristics muon X-rays from the target material. The primary X-rays of interest are the 346.828 keV line for aluminium targets, and the 400.177 line for silicon targets. The energies and intensities of the X-rays listed in table 4.1 follow measurement results from Measday and colleagues [53].

The germanium detector is a GMX20P4-70-RB-B-PL, n-type, coaxial high purity germanium detector produced by ORTEC. The detector was optimised for low energy gamma and X-rays measurement with an ultra-thin entrance window of 0.5-mm-thick beryllium and a 0.3-µm-thick ion implanted contact. The germanium crystal is 52.5 mm in diameter, and 55.3 mm in length. The axial well has a diameter of 9.9 mm and 47.8 mm deep.

ORTEC quoted the energy resolution of the detector is 1.90 keV at the 1.73 MeV gamma line. The detector is equipped with a transistor reset preamplifier which, according to the producer, enables it to work in an ultra-high rate environment up to 10^6 countss^{-1} at 1 MeV.

The detector was installed outside of the vacuum chamber at 32 cm from the target, viewing the target through a 10-mm-thick aluminium window, behind a plastic scintillator counter used to veto electrons. Liquid nitrogen necessary for the operation of the detector had to be refilled every 8 hours. A timer was set up in the data acquisition system to remind this.

4.1.5 Plastic and liquid scintillators

Apart from the scintillators in the upstream group, there were four other plastic scintillators used as veto counters for:

- punch-through-the-target muons, ScVe
- electrons and other high energy charged particles for germanium detector (ScGe) and silicon detectors (ScL and ScR)

The ScL, ScR and ScVe were installed inside the vacuum vessel and were optically connected to external PMTs by light-guides at the bottom flange.

We also set up two liquid scintillation counters for neutron measurements in preparation for the next beam time where the neutron measurements will be carried out.

4.2 Front-end electronics and data acquisition system

The front-end electronics of the AlCap experiment was simple since we employed a trigger-less read out system with waveform digitisers and flash ADCs (FADCs). As shown in figure 4.6, all plastic scintillators signals were amplified by PMTs, then fed into the digitisers. The signals from silicon and germanium detectors were preamplified, and subsequently shaped by spectroscopy amplifiers and timing filter amplifiers (TFAs) to provide energy and timing information.

The germanium detector has its own transistor reset preamplifier installed very close to the germanium crystal. Two ORTEC Model 142 preamplifiers were used for the thick silicon detectors. The timing outputs of the preamplifiers were fed into three ORTEC Model 579 TFAs. We used an ORTEC Model 673 to shape the germanium signal with 6 µs shaping time.

A more modern-style electronics was used for thin silicon detectors where the preamplifier, shaping and timing amplifiers were implemented on one compact package, namely a Mesytec MSI-8 box. This box has 8 channels, each channel consists of one preamplifier board and one shaper-and-timing filter board which can be fine-tuned independently. The shaping time was set to 1 µs for all channels.

The detector system produced signals that differs significantly in time scale, ranging from very fast (about 40 ns from scintillators) to very slow (several µs from shaping outputs of semiconductor detectors). This lead to the use of several sampling frequencies from 17 MHz to 250 MHz, and three types of digitisers were employed:

- custom-built 12-bit 170-MHz FADCs which was designed for the MuCap experiment. Each FADC board has the same dimensions as those of a single-width 6U VME module, but is hosted in a custom built crate due to its different power supply mechanical structure. The FADC communicates with a host computer through a 100-Mb/s Ethernet interface using a simple Ethernet-level protocol. The protocol only allows detecting incomplete data transfers but no retransmitting is possible due to the limited size of the module's output buffer. The FADCs accept clock signal at the frequency of 50 MHz then multiply that internally up to 170 MHz. Each channel on one board can run at different sampling frequency not dependent on other channels. The FADC has 8 single-ended LEMO inputs with 1 V pp dynamic range.

- a 14-bit 100-MS/s CAEN VME FADC waveform digitiser model V1724. The module houses 8 channels with 2.25 Vpp dynamic range on single-ended MCX coaxial inputs. The digitiser features an optical link for transmission of data to its host computer. All of 8 channels run at the same sampling frequency and have one common trigger.

- a 12-bit 250-MS/s CAEN desktop waveform digitizer model DT5720. This digitiser is similar to the V1724, except for its form factor and maximum sampling frequency. Although there is an optical link available, the module is connected to its host computer through a USB 2.0 interface where data transfer rate of 30 MB/s was determined to be good enough in our run (actual data rate from this digitiser was typically about 5 MB/s during the run). Communication with both CAEN digitisers was based on CAEN's proprietary binary drivers and libraries.

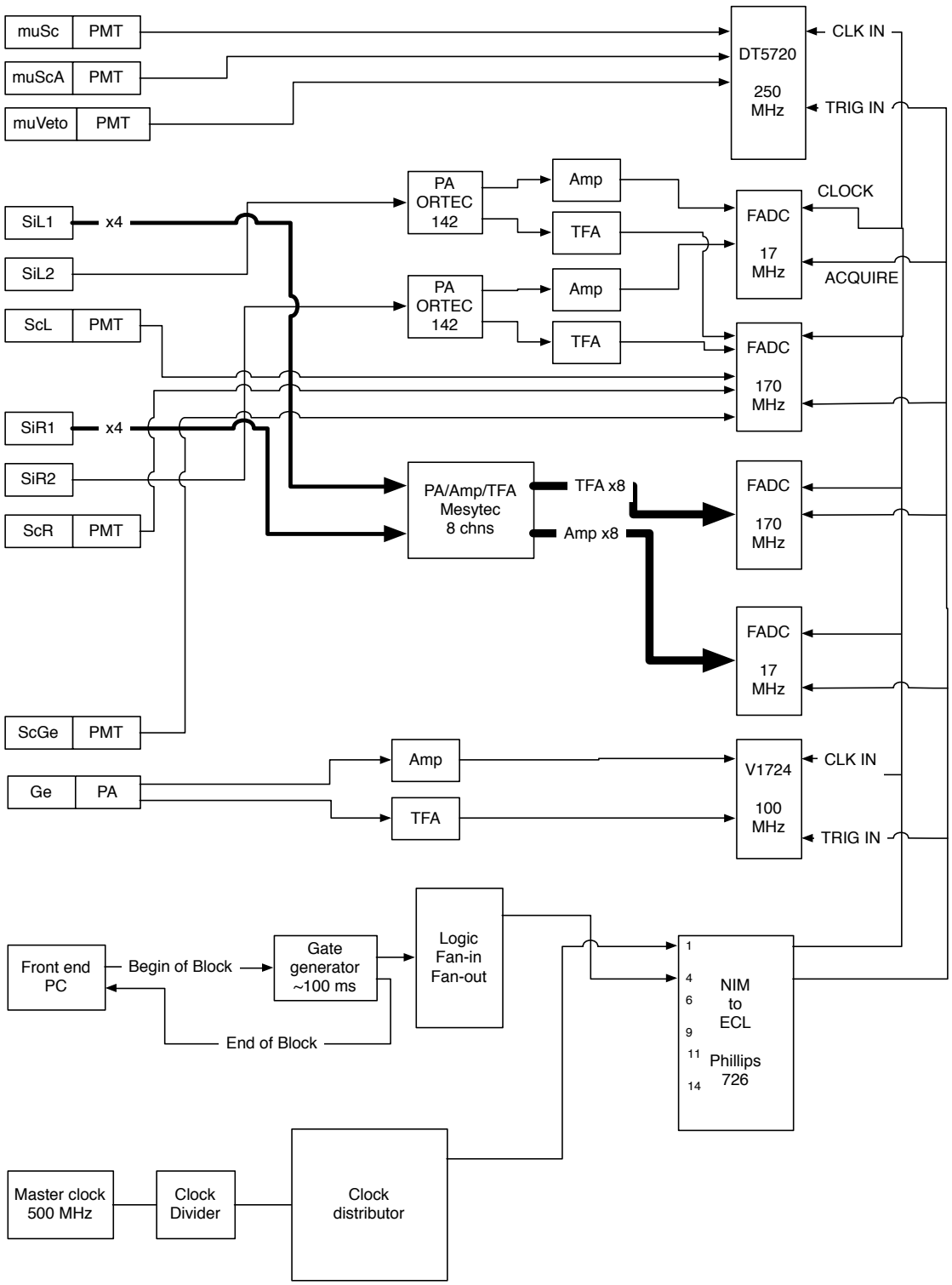

Figure 4.6: Schematic diagram of the electronics and DAQ used in the Run 2013

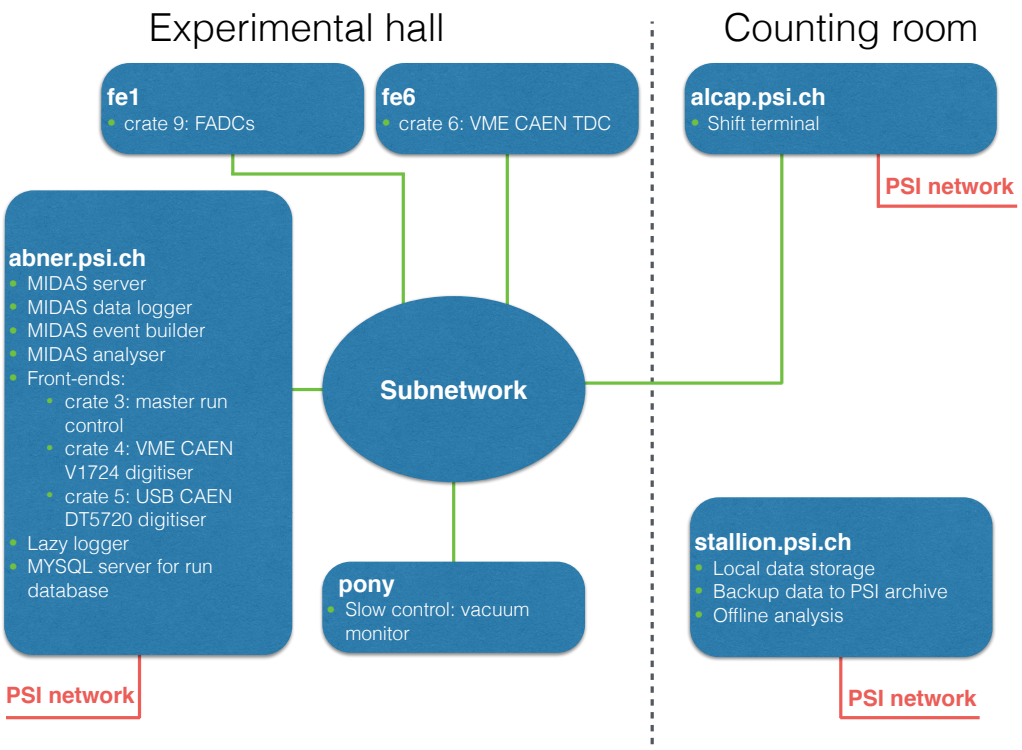

Figure 4.7: AlCapDAQ in the Run 2013. The `fe6` front-end is a VME single board computer belongs to the MuSun group, reads out the upstream detectors.

All digitisers were driven by external clocks which were derived from the same 500-MHz master clock, a high precision RF signal generator Model SG382 of Stanford Research System.

The silicon detectors were read out by FADC boards feature network-based data readout interface. To maximize the data throughput, each of the four FADC boards was read out through separate network adapter. The CAEN digitisers were used to read out the germanium detector (timing and energy, slow signals) or scintillator detectors (fast signals). For redundancy, all beam monitors (μSC, μSCA and μPC) were also read out by a CAEN time-to-digital converter (TDC) model V767 which was kindly provided by the MuSun experiment.

The Data Acquisition System (DAQ) of the AlCap experiment, so-called AlCapDAQ, provided the readout of front-end electronics, event assembling, data logging, hardware monitoring and control, and the run database of the experiment (figure 4.7). It was based on the MIDAS framework [2] and consisted of two circuits, *i*) a detector circuit for synchronous data readout from the front-end electronics instrumenting detectors, and *ii*) a slow control circuit for asynchronous periodic hardware monitoring (vacuum, liquid nitrogen filling). The detector circuit consisted of three computers, two front-end computers and one computer serving both as a front-end and as a back-end processor. The slow circuit consisted of one computer. All computers were running Linux operating system and connected into a private subnetwork.

The data were collected as dead-time-free time segments of 110 ms, called "block", followed by about 10-ms-long time intervals used to complete data readout and synchronize

[2] MIDAS is a general purpose DAQ software system developed at PSI and TRIUMF: `http://midas.triumf.ca`

the DAQ. Such data collection approach was chosen to maximize the data readout efficiency. During each 110-ms-long period, signals from each detector were digitized independently by threshold crossing. The data segment of each detector data were first written into on-board memories of front-end electronics and either read out in a loop (CAEN TDCs and CAEN digitizers) or streamed (FADCs) into the computer memories. The thresholds were adjusted as low as possible and individually for each detector. The time correlation between detectors would be established in the analysis stage.

At the beginning of each block, the time counter in each digitiser is reset to ensure time alignment across all modules. The period of 110 ms was chosen to be: *i*) long enough compared to the time scale of several µs of the physics of interest, *ii*) short enough so that there is no timer rollover on any digitiser (a FADC runs at its maximum speed of 170 MHz could handle up to about 1.5 s with its 28-bit time counter).

To ease the task of handling data, the data collecting period was divided into short runs, each run stopped when the logger had recorded 2 GB of data. The data size effectively made each run last for about 5 minutes. The DAQ automatically started a new run with the same parameters after about 6 seconds. The short period of each run also allows the detection, and helps to reduce the influence of effects such as electronics drifting, temperature fluctuation.

4.3 Detector calibration

The calibration was done mainly for the silicon and germanium detectors because they would provide energy information. The plastic scintillators were only checked by oscilloscopes to make sure that the minimum ionisation particles (MIPs) could be observed. The upstream plastic scintillation counters and wire chamber, as mentioned, were well-tuned by the MuSun group.

4.3.1 Silicon detector

The energy calibration for the silicon detectors were done routinely during the run, by:

- a 79.5 Bq ^{241}Am alpha source. The most prominent alpha particles have energies of 5.484 MeV (85.2%) and 5.442 MeV (12.5%). The alpha particles from the source would lose about 66 keV in the 0.5 µm-thick dead layer, and the peak would appear at 5418 keV (figure 4.8);

- a tail pulse generator, A tail pulse with amplitude of 66 mV was used to simulate the response of the silicon detectors' preamplifiers to a particle with 1 MeV energy deposition; and

- during data taking period, electrons in the beam were were also used for energy calibration of thick silicon detectors where energy deposition is large enough. The muons at different momenta provided another mean of calibration in the beam tuning period.

The conversion from ADC value to energy is done with a first-order polynomial:

$$\mathrm{E\ [keV]} = \mathrm{Slope} \times \mathrm{ADC} + \mathrm{Offset}. \tag{4.1}$$

The calibration coefficients for the silicon channels are listed in table 4.2.

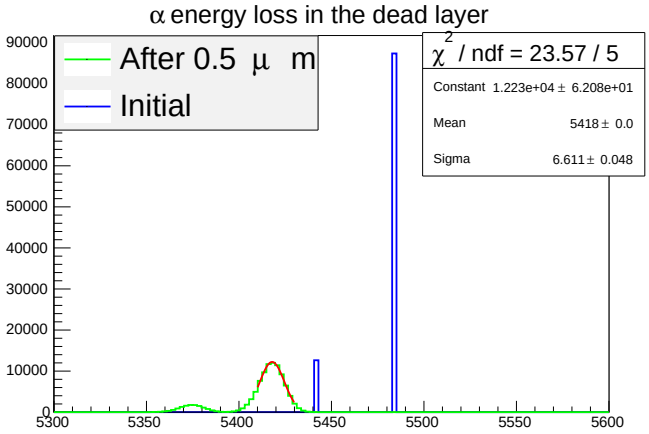

Figure 4.8: Energy loss of the alpha particles after a dead layer of 0.5 µm.

Detector	Slope	Offset
SiL-2	7.86	14.1
SiR-2	7.96	22.92
SiL1-1	2.61	−96.54
SiL1-2	2.54	−36.47
SiL1-3	2.65	−114.17
SiL1-4	2.54	−68.1
SiR1-1	2.53	−71.72
SiR1-2	2.62	−122.51
SiR1-3	2.49	−14.81
SiR1-4	2.53	−87.22

Table 4.2: Calibration coefficients of the silicon detector channels

4.3.2 Germanium detector

The germanium detector was calibrated using a ^{152}Eu source [3], the recorded pulse height spectrum is shown in figure 4.9. The source was placed at the target position so that the absolute efficiencies can be calculated. The peak centroids and areas were obtained by fitting a Gaussian peak on top of a first-order polynomial background. The only exception is the 1085.84 keV line because of the interference of the 1089.74 keV gamma, the two were fitted with two Gaussian peaks on top of a first-order polynomial background.

The relation between pulse height in ADC value and energy is found to be:

$$\mathrm{E\ [keV]} = 0.1219 \times \mathrm{ADC} + 1.1621 \tag{4.2}$$

The energy resolution (full width at half maximum - FWHM) was better than 2.6 keV for all the ^{152}Eu peaks. It was a little worse at 3.1 keV for the annihilation photons at 511.0 keV.

Following corrections for the peak areas are considered:

1. Correction for counting loss due to finite response time of the detector system, where two gamma rays arrive at the detector within a time interval short compared to that

[3] Energies and intensities of gamma rays are taken from the X-ray and Gamma-ray Decay Data Standards for Detector Calibration and Other Applications, which is published by IAEA at `https://www-nds.iaea.org/xgamma_standards/`

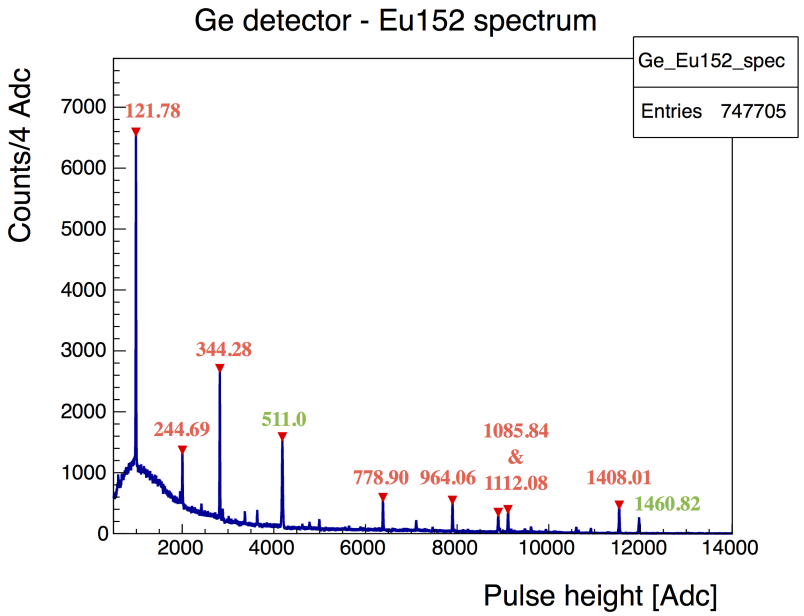

Figure 4.9: Energy spectrum of the ^{152}Eu calibration source recorded by the germanium detector. The most prominent peaks of ^{152}Eu along with their energies are annotated in red; the 1460.82 keV line is background from ^{40}K; and the annihilation 511.0 keV photons come both from the source and the surrounding environment.

response time. This correction is significant in our germanium system because of the current pulse information extracting method does not count the second pulse (see section 4.5.3).

2. Correction of counting time loss in the reset periods of the transistor reset preamplifier. A preamplifier of this type would reset itself after accumulating a predetermined amount of charge. During a reset, the preamplifier is insensitive so this can be counted as a dead time.

3. True coincidence summing correction: two cascade gamma rays hit the detector at the same time would cause loss of counts under the two respective peaks and gain under the sum energy peak.

4. Correction for self-absorption of a gamma ray by the source itself.

The corrections for the first two mechanisms can be estimated by examining pulse length and intervals between two consecutive pulses in the germanium detector (figure 4.11). The average pulse length is 45.7 µm, the average count rate obtained from the decay rate of the interval spectrum is $240\,\mathrm{s}^{-1}$.

The correction factor for the finite response time of the detector system is calculated as:

$$k_{\text{finite response time}} = e^{2\times(\text{pulse length})\times(\text{count rate})} \tag{4.3}$$

$$= e^{2\times 47.5\times 10^{-6}\times 241}$$

$$= 1.02 \tag{4.4}$$

The resets of the preamplifier show up as a peak around 2 ms, consistent with specification of the manufacturer. Fitting the peak on top of an exponential background gives the actual reset pulse length of 1947.34 µs and the number of resets during the calibration runs is 2335.0. The total time loss for resetting is hence: $1947.34 \times 10^{-6} \times 2335.0 = 4.55$ s.

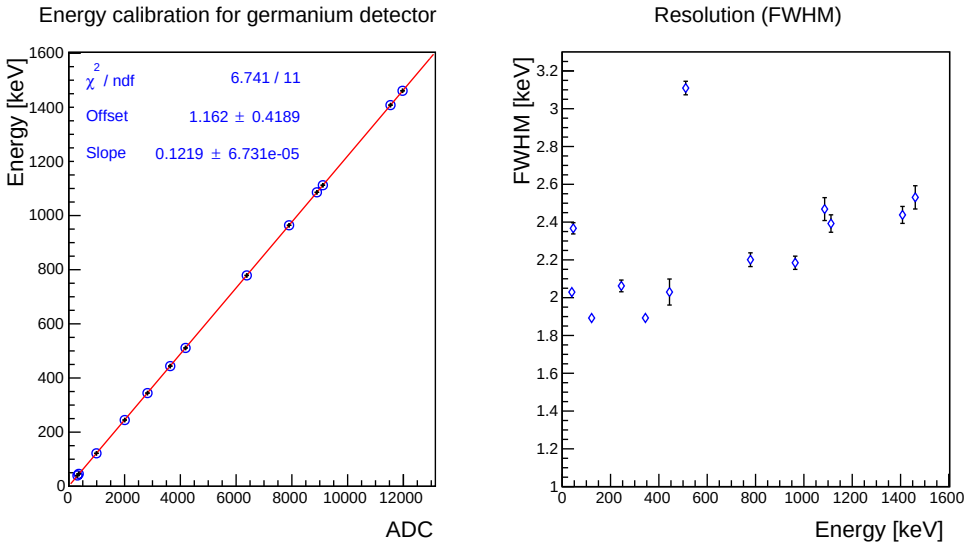

Figure 4.10: Germanium energy calibration and resolution.

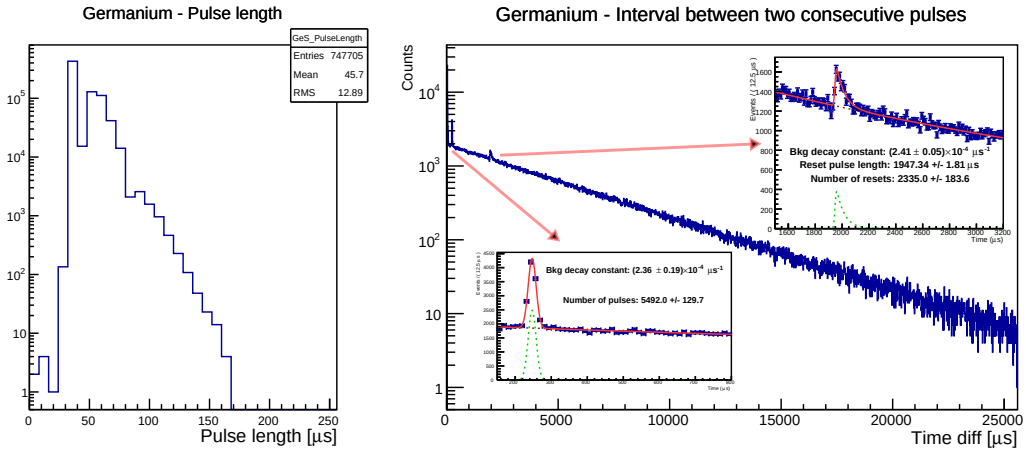

Figure 4.11: Germanium detector pulse length (left) and intervals between pulses on that detector (right). The peak around 2 ms corresponds to the resets of the preamplifier. The peak at 250 µs is due to triggering by the timing channel which is on the same digitiser.

That is a 0.14% loss for a measuring time of 3245.5 s. This percentage loss is insignificant compared with the loss in (4.4) and the statistical uncertainty of peak areas.

The true coincidence summing probability is estimated to be very small, about 5.4×10^{-6}, thanks to the far geometry of the calibration. The absorption in the source cover made of 22 mg/cm^2 polyethylene is less than 4×10^{-4} for a 100 keV photon. Therefore these two corrections are omitted.

The absolute efficiencies of the reference gamma rays show agreement with those obtained from a Monte Carlo (MC) study where a point source made of ^{152}Eu is placed at the target position (see figure 4.12). A comparison between efficiencies in case of the point-like source and a finite-size source is also done by MC simulation. The differences between the two sources are generally smaller than 3%, which are comparable with the uncertainties of the efficiency calibration. That means the point-like efficiencies can be used for a finite-sized source without correction. The absolute efficiencies of the referenced points, and calculated efficiencies at X-rays of interest are listed in table 4.3.

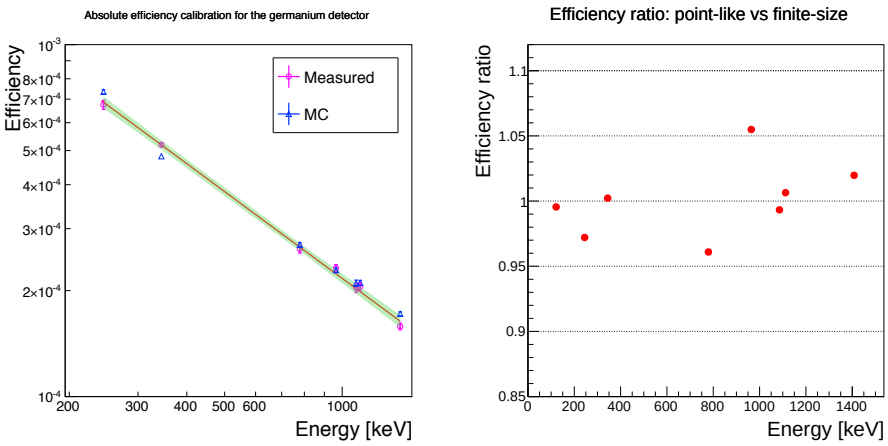

Figure 4.12: Absolute efficiency of the germanium detector (right) and MC comparison of efficiencies in case of point-like and finite-sized sources (left). The efficiencies curve is fitted on 7 measured energy points from 244 keV to 1408 keV, the shaded area is 95% confidence interval of the fit. The ratios on the left plot are normalised to the efficiencies of the point-like case at each energy point.

4.4 Data sets and statistics

The main goal of this Run 2013 was to measure the rates and energy spectra of protons following muon capture on aluminium. Also for normalisation and cross checking against the existing experimental data, two types of measurements with different targets were carried out for silicon targets:

(a) an active, thick target similar to the set up used by Sobottka and Wills [32]. This provides a cross-check against the existing experimental data. The silicon detector package at the right hand side was moved to the target position with the thick detector facing the muon beam in this set up.

(b) a passive, thin target and heavy charged particles were observed by the two silicon packages. The measurement serves multiple purposes: confirmation that the particle identification by dE/dx actually works, separation of components of heavy charged particles emitted from the silicon target.

As the emitted protons deposit a significant amount of energy in the target material, thin targets and thus excellent momentum resolution of the low energy muon beam are critical, aluminium targets of 50-µm and 100-µm thick were used. Although a beam with low momentum spread of 1% is preferable, it was used for only a small portion of the run due to the low beam rate (see figure 4.2). The beam momentum for each target was chosen to maximise the number of stopped muons. The collected data sets are shown in table 4.4.

4.5 Analysis framework

4.5.1 Concept

Since the AlCapDAQ is a trigger-less system, it stored all waveforms of the hits occured in 100-ms-long blocks without considering their physics significance. The analysis code therefore must be able to extract parameters of the waveforms, then organises the pulses into the physics events correlated to stopped muons (figure 4.13). In addition, the analyser is intended to be usable as a real-time component of a MIDAS DAQ, where simple analysis could be done online for monitoring and diagnostic during the run.

Photons (keV)	**Efficiency**	**Uncertainty**
121.78	9.05×10^{-4}	1.18×10^{-5}
244.69	6.40×10^{-4}	1.89×10^{-5}
344.28	5.00×10^{-4}	0.593×10^{-5}
778.90	2.56×10^{-4}	0.771×10^{-5}
964.06	2.22×10^{-4}	0.573×10^{-5}
1085.84	1.97×10^{-4}	0.822×10^{-5}
1112.08	1.88×10^{-4}	0.539×10^{-5}
1408.01	1.53×10^{-4}	0.339×10^{-5}
346.828	4.95×10^{-4}	1.22×10^{-5}
399.268	4.41×10^{-4}	0.978×10^{-5}
400.177	4.40×10^{-4}	0.975×10^{-5}
476.800	3.81×10^{-4}	0.768×10^{-5}

Table 4.3: Absolute efficiencies of the germanium detector in case of a point-like source placed at the centre of the target (upper half), and the calculated efficiencies for the X-rays of interest (lower half).

Target and thickness	**Momentum scaling factor**	**Run time (h)**	**Number of muons**
Si 1500 µm	1.32	3.07	2.78×10^7
	1.30	12.04	2.89×10^8
	1.10	9.36	1.37×10^8
Si 62 µm	1.06	10.29	1.72×10^8
Al 100 µm	1.09	14.37	2.94×10^8
	1.07	2.56	4.99×10^7
Al 50 µm	1.07	51.94	8.81×10^8

Table 4.4: Run statistics. Momentum scaling factors are normalised to 28 MeV/c.

The analysis framework of the AlCap consists of two separate programs. A MIDAS-based analyser framework, `alcapana`, processes the raw data and passes its ROOT data output to the second stage, `rootana`, where most of the physics analysis is performed. Both of the programs were designed to be modularised, which allowed us to develop lightweight analysis modules that were used online to generate plots quickly, while more sophisticated modules can be applied in offline analysis.

The DAQ system generated MIDAS files which stores the data as a stream of MIDAS "banks". In the AlCapDAQ, each bank corresponds to a single channel on a digitizer and was named according to a predefined convention. The map between detector channels and MIDAS bank names was stored in the MIDAS online database (ODB), along with other settings such as sampling frequencies, timing offsets, thresholds and calibration coefficients of each channel.

The first step of the analysis framework is to convert the raw MIDAS data into waveforms, series of digitised samples continuous in time corresponding to pulses from the detector. The waveform is called `TPulseIslands`, which contain the bank name, the ADC values of the samples and the time stamp of the first sample. This conversion is performed

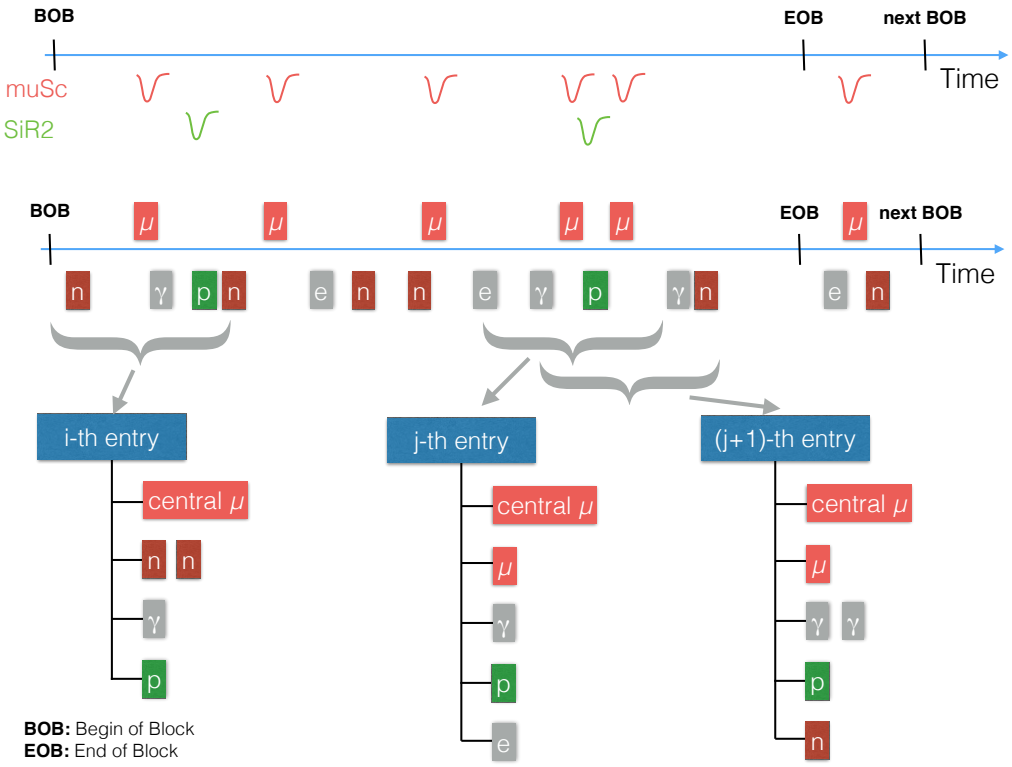

Figure 4.13: Concept of the AlCap analysis code: pulses from individual detector in blocks of time are analysed, then sorted centred around stopped muons.

in `alcapana` and the resulting objects are stored in a ROOT output file as a `TTree`.

The next step of the analysis is to obtain summary parameters of the pulses from the digitized samples. The parameters of primary interest are the amplitude and time of the peak and the integral of the pulse. This extraction of parameters is done by a `rootana` module, and the objects produced by this stage are called `TAnalysedPulse`s. Currently, we have a usable and simple algorithm that takes the pulse parameters from the peak of the waveform. In parallel, a pulse finding and template fitting code is being developed because it would provide more accurate pulse information. The first iteration of this code has been completed and is being tested.

After obtaining pulse parameters for individual channel, the pairing up of fast and slow pulses from the same physical detector needs to be done. This entails looping through all fast and slow pulses from each detector, checking for correlated pulses in time and amplitude, creating `TDetectorPulse`s. The `TDetectorPulse`s allow better understanding of the hits on the detector by combining timing information from the fast channel and amplitude information from the slow channel. It also helps reduce the impact of pile-up on the amplitude measurement, where the improved time resolution of the fast channels can be used to separate the overlapping amplitudes in the slow channels. The pulse pairing are applicable to the silicon and germanium channels only. The scintillator channels provide only fast timing signals which can be used as `TDetectorPulse`s directly.

The detector pulses are subsequently used to identify particles that hit the detectors. These particle hits are still stored in the time-ordered tree corresponds to the 110 ms block length from the AlCapDAQ. By iterating through the tree to find stopped muons and taking any hits within a certain window around this muon from every detector, a stopped-muon-centred tree shown in figure 4.13 can be produced. This will make it much easier to look for coincidences and apply cuts, thereby bringing the end goal of particle numbers and energy

Module name	Functions
common/MUnCompressRawData	decompress raw MIDAS data
FADC/MOctalFADCProcessRaw v1724/MV1724ProcessRaw dt5720/MDT5720ProcessRaw	convert raw data to `TPulseIslands`
muSC_muPC/MCaenCompProcessRaw muSC_muPC/MMuPC1AnalysisC muSC_muPC/MMuPC1AnalysisMQL muSC_muPC/MMuSCAnalysisMQL	decompress data from `fe6`, make coincidence in upstream counters
diagnostics/MCommonOnlineDisplayPlots	produce plots of interest
FADC/MOctalFADCBufferOverflow FADC/MOctalFADCPacketLoss	diagnostics for FADCs
common/MExpectedIslands common/MMuSCTimeDifferences common/MNumberIslands common/MPulseLengths	diagnostics in general
common/MTreeOutput	save `TPulseIslands` tree

Table 4.5: Online analysis modules in the Run 2013.

distributions.

4.5.2 Online analyser

The online analyser was developed and proved to be very useful during the run. A few basic modules were used to produce plots for diagnostic purposes including: persistency view of waveforms, pulse height spectra, timing correlations with respect to the upstream counters. The modules and their purposes are listed in table 4.5.

The `alcapana` served the plots on port 9090 of the `abner` via the ROOT socket protocol. We then used a ROOT-based program called `online-display` to display the plots on the shift terminal (`alcap`). The `online-display` simply executed ROOT macros which retrieved plots from the ROOT server, sorted then drew them in groups such as upstream counters, silicon arms. It could also periodically update the plots to reflect real-time status of the detector system.

4.5.3 Offline analyser

Some offline analysis modules have been developed during the beam time and could provide quick feedback in confirming and guiding the decisions at the time. For example, the X-ray spectrum analysis was done to confirm that we could observe the muon capture process and to help in choosing optimal momenta which maximised the number of stopped muons.

Although the offline analyser is still not fully available yet, several modules are ready (table 4.6). An initial analysis is possible using the existing modules thanks to the modularity of the analysis framework.

The MakeAnalysedPulses module takes a raw waveform, calculates the pedestal from a predefined number of first samples, subtracts this pedestal taking pulse polarity into account, then calls another module to extract pulse parameters. At the moment, the simplest module, so-called MaxBinAPGenerator, for pulse information calculation is in use. The module looks

Module name	Functions
MakeAnalysedPulses	make a pulse with parameters extracted from a waveform
MaxBinAPGenerator	simplest algorithm to get pulse information
TSimpleMuonEvent	sort pulses occur in a fixed time window around the muon hits
ExportPulse & PulseViewer	plot waveforms for diagnostics
PlotAmplitude	plot pulse height spectra
PlotAmpVsTdiff	plot pulse correlations in timing and amplitude
EvdE	plot $^{dE}/_{dx}$ histograms

Table 4.6: Available offline analysis modules.

for the sample that has the maximal deviation from the baseline, takes the deviation as pulse amplitude and the time stamp of the sample as pulse time. The procedure is illustrated on figure 4.14. This module could not handle pile-up or double pulses in one `TPulseIsland` in figure 4.15.

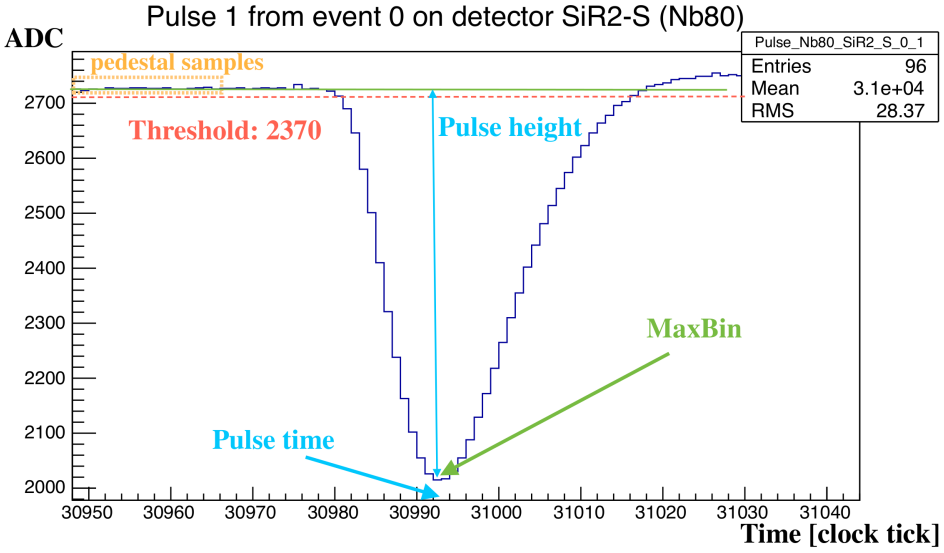

Figure 4.14: Pulse parameters extraction with MaxBinAPGenerator.

The TSimpleMuonEvent first picks a muon candidate, then loops through all pulses on all detector channels, and picks all pulses occur in a time window of ±10 µs around each candidate to build a muon event. A muon candidate is a hit on the upstream plastic scintillator with an amplitude higher than a threshold which was chosen to reject MIPs. The period of 10 µs is long enough compared to the mean life time of muons in the target materials (0.758 µs for silicon, and 0.864 µs for aluminium [15]) so practically all of emitted charged particles would be recorded in this time window.

A pile-up protection mechanism is employed to reject multiple muons events: if there exists another muon hit in less than 15 µs from the candidate then both the candidate and the other muon are discarded. This pile-up protection would cut out less than 11% total number of events because the beam rate was generally less than 8 kHz.

To make sure that we will analyse good data, a low level data quality checking was done on the whole data sets. The idea is to plot the variations of basic parameters, such as noise level, length of raw waveforms, pulse rate, time correlation to hits on the muon counter on

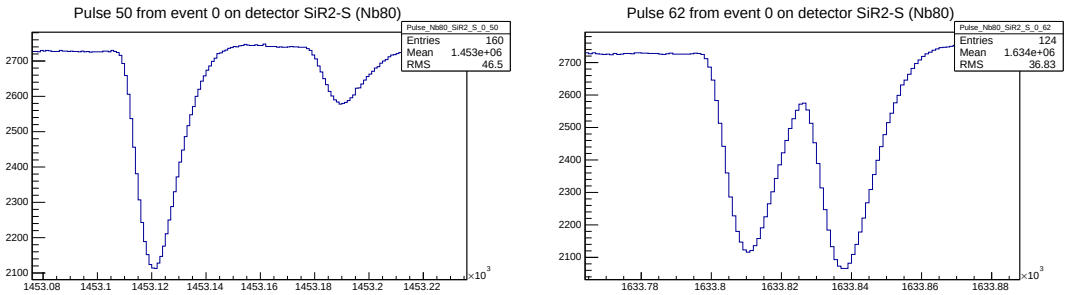

Figure 4.15: Double pulse and pile up are taken as one single pulse by the MaxBinAPGenerator

each channel during the data collecting period. Runs with significant difference from the averaging values were further checked for possible causes, and would be discarded if such discrepancy was too large or unaccounted for. Examples of such trend plots are shown in figure 4.16.

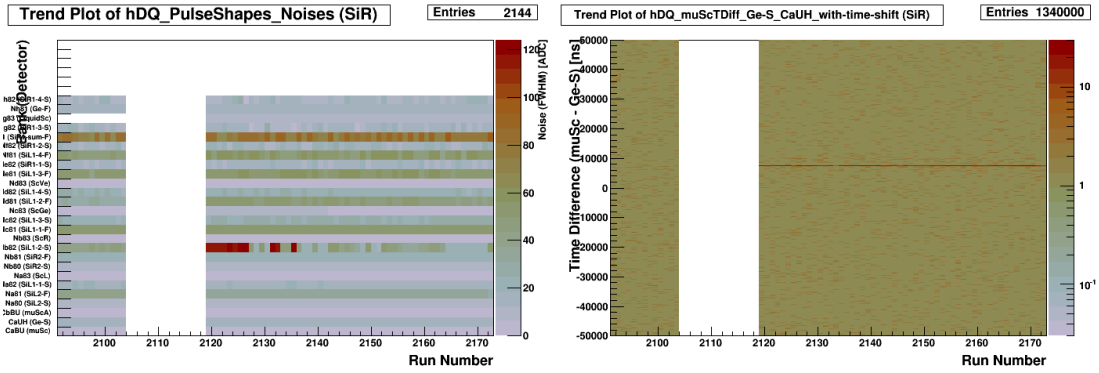

Figure 4.16: Example trend plots used in the low level data quality checking: noise level in FWHM (left) and time correlation with muon hits (right). The horizontal axis is run number, the vertical axis is the channel name (left), or the time difference between hit in the germanium detector and a hit in upstream counter (right). Colors in both plots indicate the number of events. In the left plot, the noise level was basically stable in in this data set, except for one channel where there was a sudden jump in a range of runs. On the right hand side, this sanity check helped find out the sampling frequency was wrongly applied in the first tranche of the data set.

4.6 Monte Carlo simulation

A full Monte Carlo (MC) simulation of the experimental set up has been developed based on Geant4 [54]. The geometrical implementation was detailed as much as possible and could be modified via configuration scripts at run time. Descriptions of the muon beam came from the beam line optic calculation provided by the accelerator experts at PSI.

The MC model greatly assisted the design of the experiment, such as alignment of the detectors with respect to the target, and shielding of scattered muons. It also helped make a sense of the observed results during the run and data analysing.

Chapter 5

Data analysis and results

This chapter presents the first analysis on subsets of the collected data for the aluminium 100-µm-thick target. The analysis use information from silicon, germanium, and upstream muon detectors. Pulse parameters were extracted from waveforms by the simplest method of peak sensing (as mentioned in section 4.5.3). Purposes of the analysis include:

- testing the analysis chain;
- verification of the experimental method, specifically the normalisation of number of stopped muons, and particle identification using specific energy loss;
- extracting a preliminary rate and spectrum of proton emission from aluminium.

5.1 Number of stopped muons normalisation

The active silicon target runs was used to check for the validity of the counting of number of stopped muons, where the number can be calculated by two methods:

- counting hits on the active target in coincidence with hits on the upstream scintillator counter;
- inferred from number of X-rays recorded by the germanium detector.

This analysis was done on a subset of the active target runs 2119 to 2140, which contains 6.43×10^7 muon events.

5.1.1 Number of stopped muons from active target counting

Because of the active target, a stopped muon would cause two coincident hits on the muon counter and the target. The energy of the muon hit on the active target is also well-defined as the narrow-momentum-spread beam was used. The correlation between the energy and timing of all the hits on the active target is shown in figure 5.1.

The prompt hits on the active silicon detector are mainly beam particles: muons and electrons. The most intense spot at time zero and about 5 MeV energy corresponds to stopped muons in the thick target. The band below 1 MeV is due to electrons, either in the beam or from muon decay in orbits, or emitted during the cascading of muon to the muonic 1S state. The valley between time zero and 1200 ns shows the minimum distance in time between two pulses. It is the limitation of the current pulse parameter extraction method where no pile up or double pulses is accounted for.

The delayed hits on the active target after 1200 ns are mainly secondary particles from the stopped muons:

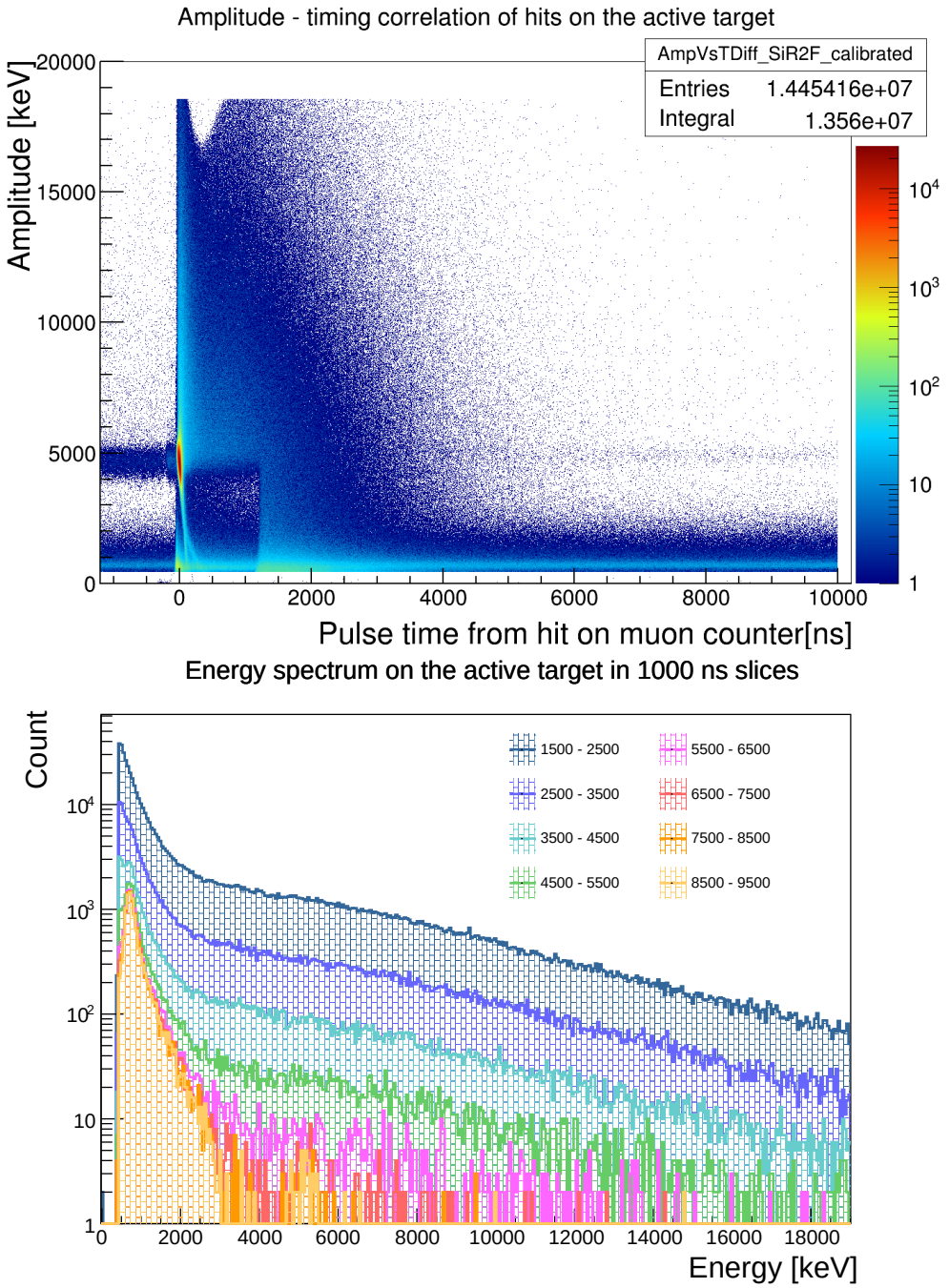

Figure 5.1: Energy - timing correlation of hits on the active target (top), and the projections onto the energy axis in 1000-ns-long slices from 1500 ns (bottom). The prompt peak at roughly 5 MeV in the top plot is muon peak. In the delayed energy spectra, the Michel electrons dominate at early time, then the beam electrons are more clearly seen in longer delay.

- electrons from muon decay in the 1S orbit,
- products emitted after nuclear muon capture, including: gamma, neutron, heavy charged particles and recoiled nucleus.

It can be seen that there is a faint stripe of muons in the time larger than 1200 ns region, they are scattered muons by other materials without hitting the muon counter. The electrons in the beam caused the constant band below 1 MeV and $t > 5000$ ns (see figure 5.1 bottom).

From the energy-timing correlation above, the cuts to select stopped muons are:

1. has one hit on muon counter (where a threshold was set to reject MIPs), and the first hit on the silicon active target is in coincidence with that muon counter hit:

$$|t_{\text{target}} - t_{\mu\ \text{counter}}| \leq 50\,\text{ns}\,, \tag{5.1}$$

2. and the first hit on the target has energy of that of the muons:

$$3.4\,\text{MeV} \leq E_{\text{target}} \leq 5.6\,\text{MeV}\,. \tag{5.2}$$

The two cuts (5.1) and (5.2) give a number of stopped muons counted by the active target:

$$N_{\mu\ \text{active Si}} = 9.32 \times 10^6 \pm 3.0 \times 10^3\,. \tag{5.3}$$

5.1.2 Number of stopped muons from the number of X-rays

The number of nuclear captures, hence the number of stopped muons in the active silicon target, can be inferred from the number of emitted muonic X-rays. The reference energies and intensities of the most prominent lines of silicon and aluminium are listed in table 5.1.

Quantity	**Aluminium**	**Silicon**
Muonic mean lifetime (ns)	864 ± 2	758 ± 2
Nuclear capture probability (%)	60.9	65.8
$(2p - 1s)$ X-ray energy (keV)	346.828 ± 0.002	400.177 ± 0.005
Intensity (%)	79.8 ± 0.8	80.3 ± 0.8

Table 5.1: Reference parameters of muon capture in aluminium and silicon taken from Suzuki et al. [15] and Measday et al. [53].

The muonic X-rays are emitted during the cascading of the muon to the muonic 1S state in the time scale of 10^{-9} s, so the hit caused by the X-rays must be in coincidence with the muon hit on the active target. Therefore an additional timing cut is applied for the germanium detector hits:

$$|t_{\text{Ge}} - t_{\mu\ \text{counter}}| < 500\,\text{ns} \tag{5.4}$$

The germanium spectrum after three cuts (5.1), (5.2) and (5.4) is plotted in figure 5.2. The $(2p-1s)$ line clearly showed up at 400 keV on a very low background. A peak at 476 keV is identified as the $(3p - 1s)$ transition. Higher transitions such as $(4p - 1s)$, $(5p - 1s)$ and $(6p - 1s)$ can also be recognised at 504 keV, 516 keV and 523 keV, respectively.

The net area of the $(2p - 1s)$ is found to be 2929.7 by fitting a Gaussian peak on top of a linear background from 395 keV to 405 keV. Using the same procedure of correcting

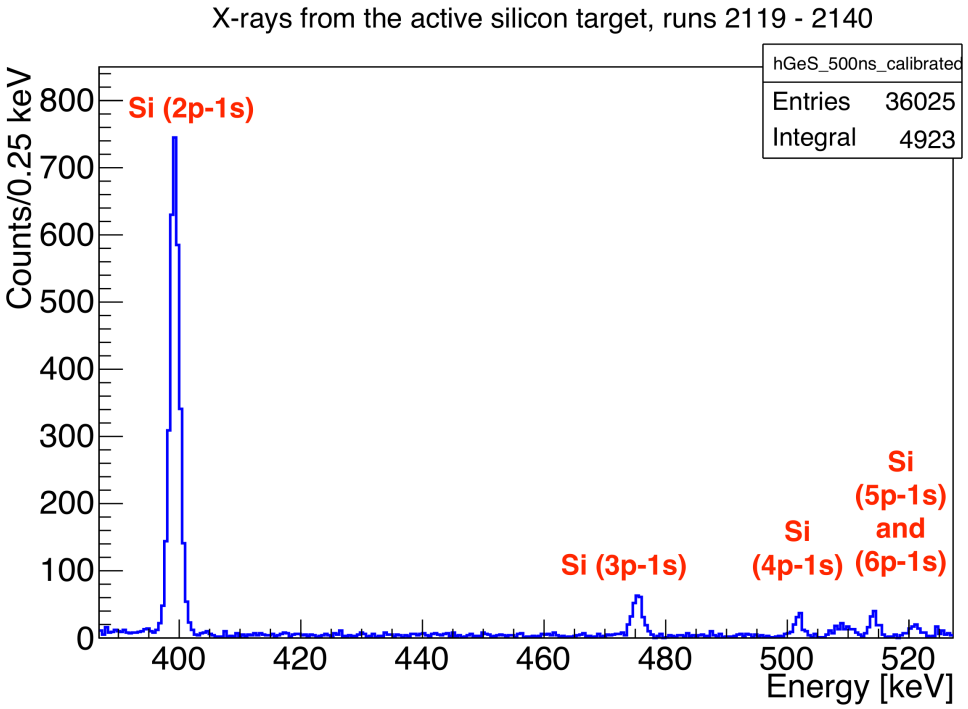

Figure 5.2: Prompt muonic X-rays spectrum from the active silicon target. The $(2p-1s)$ X-ray shows up at 400 keV; higher transitions can also be identified.

described in section 4.3.2, and taking detector acceptance and X-ray intensity into account (see table 5.2), the number of muon stopped is:

$$N_{\mu \text{ stopped X-ray}} = (9.16 \pm 0.28) \times 10^6 \,, \tag{5.5}$$

which is consistent with the number of X-rays counted using the active target.

The uncertainty of the number of muons inferred from the X-ray has equal contributions from statistical uncertainty in peak area and systematic uncertainty from efficiency calibration. The relative uncertainty in number of muons is 3%, good enough for the normalisation in this measurement.

5.2 Particle identification by specific energy loss

In this analysis, a subset of runs from 2808 to 2873 with the 100-µm aluminium target is used because of following advantages:

- it was easier to stop and adjust the muon stopping distribution in this thicker target;
- a thicker target gives better statistics because of a higher muon rate available at a higher momentum and less scattering.

Muons with momentum of 30.52 MeV/c, 3%-FWHM spread (scaling factor of 1.09, normalised to 28 MeV/c) were used for this target after a momentum scanning as described in the next subsection.

5.2.1 Momentum scan for the 100-µm aluminium target

Before deciding to use the momentum scaling factor of 1.09, we have scanned with momentum scales ranging from 1.04 to 1.12 to maximise the observed X-rays rate (and maximising

Measured X-rays	**Value**	**Absolute error**	**Relative error**
Gross integral	3083		
Background	101.5		
Net area ($2p - 1s$)	2929.7	56.4	0.02

Corrections	**Value**	**Details**
Random summing	1.06	average count rate 491.4 Hz, pulse length 57 µs
TRP reset	1.03	298 s loss during 9327 s run period
Self-absorption	1.008	silicon thickness 750 µm, linear attenuation 0.224 cm^{-1}
True coincidence	1	omitted

Efficiency and intensity	**Value**	**Absolute error**	**Relative error**
Detector efficiency	4.40×10^{-4}	0.10×10^{-4}	0.02
X-ray intensity	0.803	0.008	0.009

Results	**Value**	**Absolute error**	**Relative error**
Number of X-rays emitted	7.36×10^6	0.22×10^6	0.03
Number of muons stopped	9.16×10^6	0.28×10^6	0.03

Table 5.2: Corrections, efficiency and intensity used in calculating the number of X-rays from the active target.

the rate of stopped muons). The X-ray spectrum at each momentum point was accumulated in about 30 minutes to assure a sufficient amount of counts. Details of the scanning runs are listed in table 5.3. The on-site quick analysis suggested the 1.09 scaling factor was the

Momentum (MeV/c)	**Scaling factor**	**Runs**	**Length (s)**
29.12	1.04	2609 to 2613	2299
29.68	1.06	2602 to 2608	2563
29.96	1.07	2633 to 2637	2030
30.24	1.08	2614 to 2621	3232
30.52	1.09	2808 to 2813	2120
30.80	1.10	2625 to 2632	3234
31.36	1.12	2784 to 2792	2841

Table 5.3: Momentum scanning runs for the 100-µm aluminium target.

optimal value so it was chosen for all the runs on this aluminium target. But the offline analysis later showed that the actual optimal factor was 1.08. There were two reasons for the discrepancy:

1. the X-ray rates were normalised to run length, which is biased since there are more muons available at higher momenta;

2. the $(2p - 1s)$ peaks of aluminium at 346.828 keV were not fitted properly. The peak is interfered by a background peak at 351 keV from ^{214}Pb, but the X-ray peak area was obtained simply by subtracting an automatically estimated background.

In the offline analysis, the X-ray peak and the background peak are fitted by two Gaussian peaks on top of a linear background. The X-ray peak area is then normalised to the number of muons hitting the upstream detector (figure 5.3).

The ratio between the number of X-rays and the number of muons as a function of momentum scaling factor is plotted on figure 5.4. The trend showed that muons penetrated deeper as the momentum increased, reaching the optimal value at the scale of 1.08, then decreased as punch through happened more often from scales of 1.09 and above. The distributions of stopped muons are illustrated by MC results on the bottom plot in figure 5.4. At the 1.09 scale beam, the muons stopped 18 µm off-centred to the right silicon arm, the standard deviation of the depth distribution is 29 µm.

5.2.2 Event selection for the passive targets

As described in the section 4.5, the hits on all detectors are re-organised into muon events: central muons; and all hits within ±10 µs from the central muons. The dataset from runs 2808 to 2873 contains 1.17×10^9 of such muon events.

Particle banding identification

Selection of proton (and other heavy charged particles) events starts from searching for muon event that has at least one hit on thick silicon. If there is a thin silicon hit within a coincidence window of ±0.5 µs around the thick silicon hit, the two hits are considered to belong to one particle. The thresholds for energy deposited in all silicon channels, except the thin silicon on the left arm, are set at 100 keV in this analysis. The threshold on the left ΔE counter was higher, at roughly 400 keV, due to higher noise in that channel and it was decided at the run time to rise its threshold to reduce the triggering rate. The specific

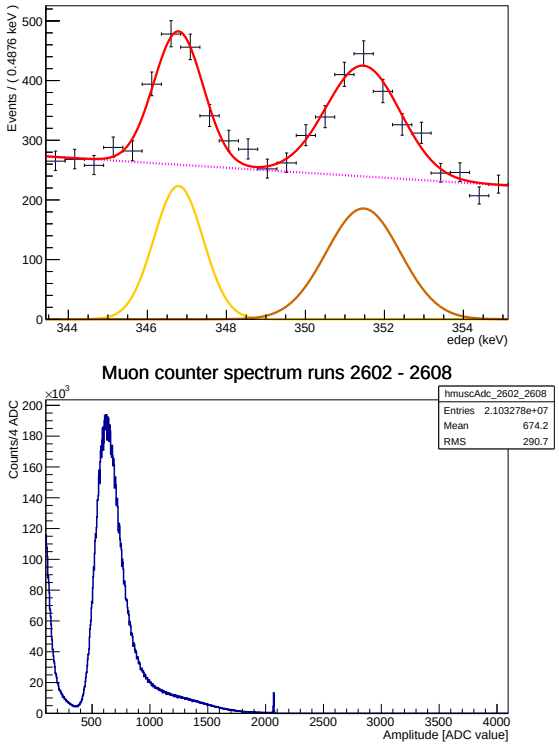

Figure 5.3: Fitting of the $(2p - 1s)$ muonic X-ray of aluminium (red) and the interfered peak at 351 keV (brown) with a linear background (left). The number of muons is integral of the upstream scintillator spectrum (right) from 400 to 2000 ADC channels.

energy loss as a function of total energy of the charged particles are plotted on figure 5.5. With the aid from MC simulation (figure 3.8), the banding on figure 5.5 can be identified as follows:

- the spot at the lower left conner belonged to electron hits;
- the scattered muons formed the small blurry cloud just above the electron region;
- the most intense band was due to proton hits;
- the less intense, upper band caused by deuteron hits;
- the highest band corresponded to alpha hits;
- the faint stripe above the deuteron band should be triton hits, which is consistent with a relatively low probability of emission of tritons.

It is not clearly seen in the $\Delta E - E$ plots because of the rather high thresholds on ΔE, but protons with higher energy would punch through both silicon detectors. Those events have low ΔE and E, making the proton bands to go backward to the origin of the $\Delta E - E$ plots. For the configuration of 58-µm thin, and 1535-µm thick detectors, the effect shows up for protons with energy larger than 16 MeV. The returning part of the proton band would make the cut described in the next subsection to include protons with higher energy into lower energy region. The effect of punch through protons could be eliminate using the veto plastic scintillators at the back of each silicon arm. But in this initial analysis, the veto information is not used, therefore the upper limit of proton energy is set at 8 MeV where there is clear separation between the protons at lower and higher energies with the same measured total energy deposition E.

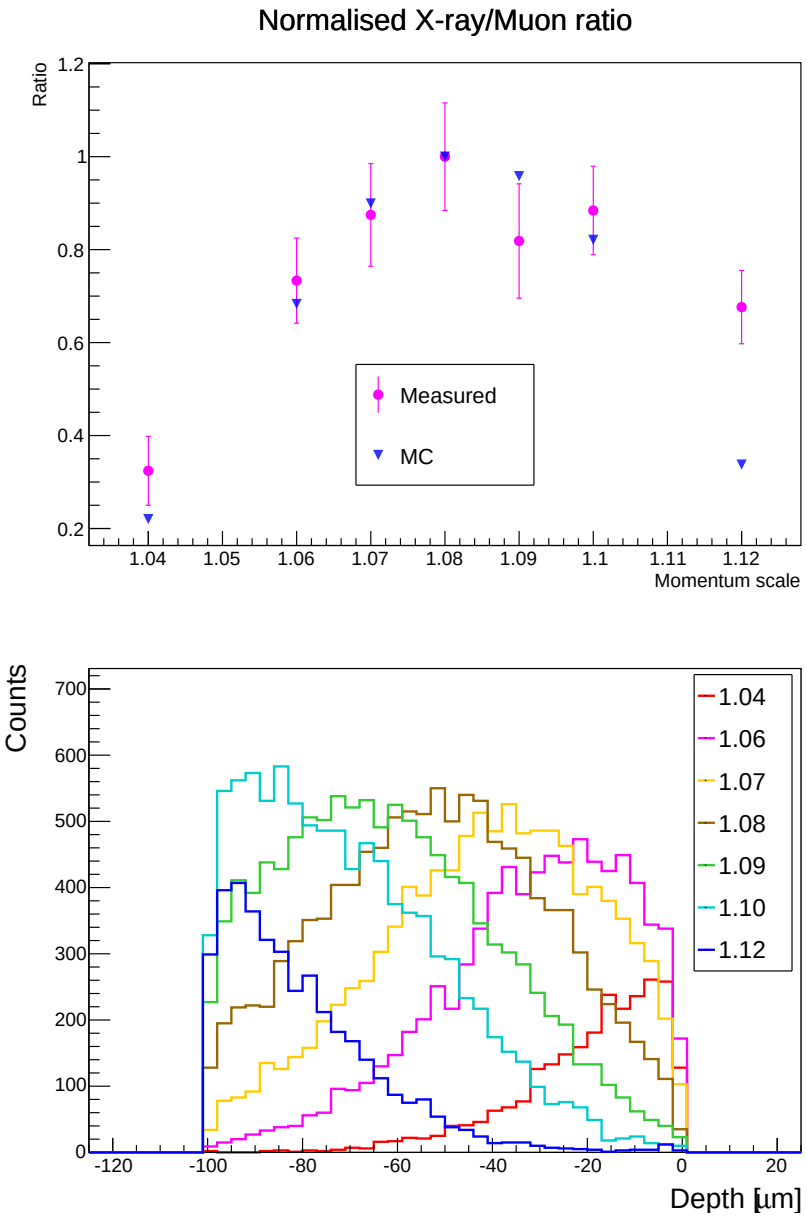

Figure 5.4: Number of X-rays per incoming muon as a function of momentum scaling factor (top); and muon stopping distributions with scaling factors from 1.04 to 1.12 obtained by MC simulation (bottom). The depth of muon stopping positions are measured normal to the surface of the target facing the muon beam.

Proton-like probability cut

Since protons of interested are at low kinetic energy, their ΔE distributions do not have long tails as that of the Landau distribution. For a given E, the distribution of ΔE is more like a Gaussian, and with slightly deformed high energy tail (see figure 5.7).

For a measured event, a proton likelihood probability is defined as:

$$P_i = \frac{1}{\sqrt{2\pi}\sigma_{\Delta E}} \exp\left[\frac{(\Delta E_{meas.} - \Delta E_i)^2}{2\sigma^2_{\Delta E}}\right], \tag{5.6}$$

where $\Delta E_{\text{meas.}}$ and E_i are measured energy deposition in thin silicon detector and in both detectors, respectively; ΔE_i and $\sigma_{\Delta E}$ are the expected value and standard deviation of the energy loss in the thin detector of protons with energy E, calculated by the MC simulation.

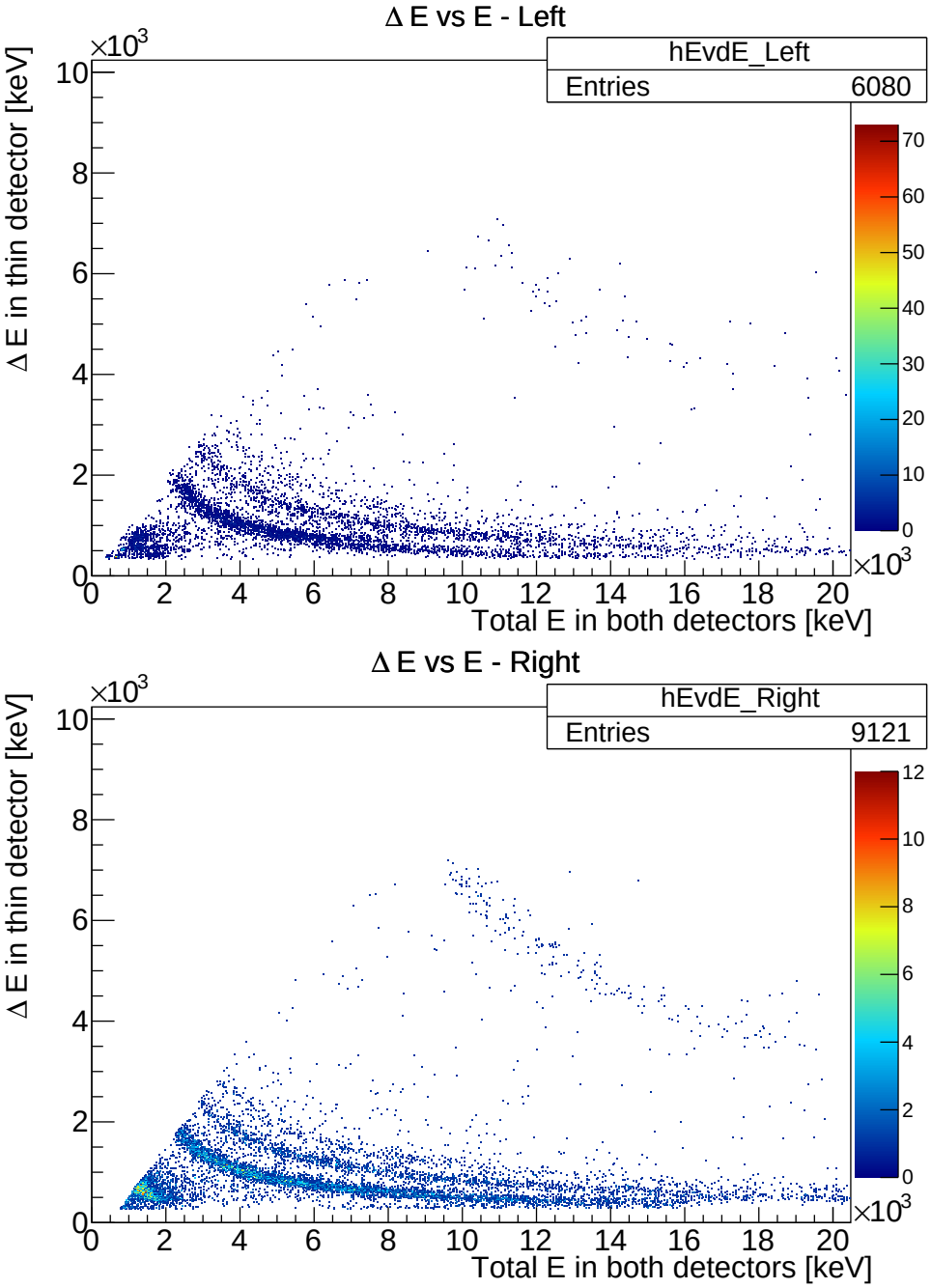

Figure 5.5: Energy loss in thin silicon detectors as a function of total energy recorded by both thin and thick detectors on the left arm (top) and the right arm (bottom).

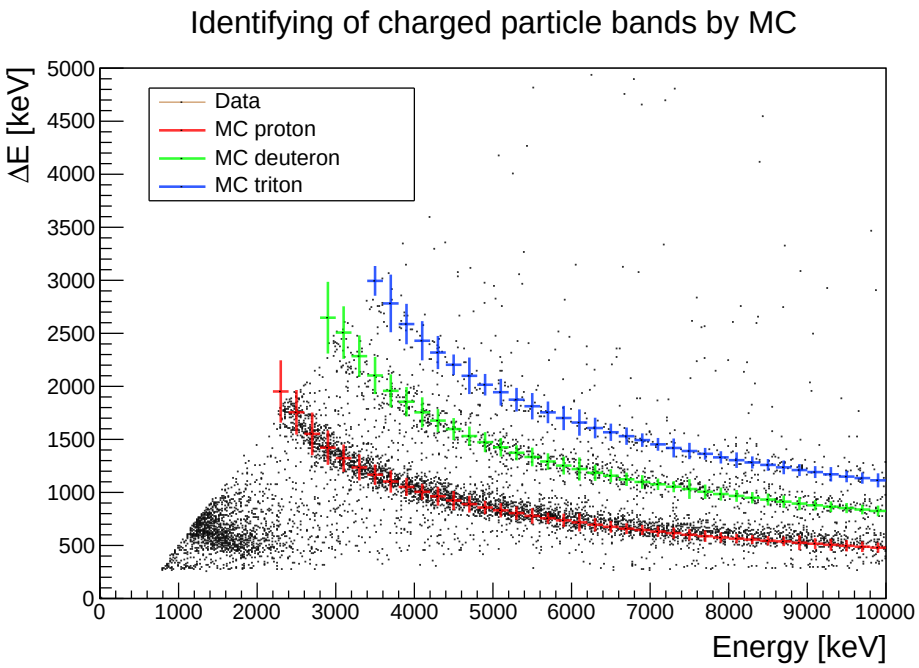

Figure 5.6: Identifying of charged particles banding: the dots are measured points, the histograms are expected bands of protons (red), deuterons (green) and tritons (blue), respectively. The MC bands are calculated for a pair of 58-µm-thick and 1535-µm-thick silicon detectors. The error bars on MC bands show the standard deviation of ΔE in E respective bins.

A measured event with higher P_i is more likely to be a proton event.

The lower threshold of proton-like probability, the more protons will be selected, but also more contamination from other charged particles would be classified as protons. The number of protons on the left and right arms at different cuts on P_i are listed in table 5.4. The proton yields are integrated in the energy range from 2.2 MeV to 8 MeV. The lower limit comes from the requirement of having at least one hit on the thick counter. The upper limit is to avoid the inclusion of punch through particles as explained in the previous session.

The cut efficiency depends on actual shape of the proton spectrum, other charged particles spectra, relative ratio between the yields of different particle species. The fraction of protons missed out, and the fraction of contamination from other charged particles at different probability thresholds, with two different assumptions on spectrum shape: flat distribution and Sobottka and Wills silicon shape (see (3.14)), are listed in the four last columns of table 5.4. The relative ratio of proton:deuteron:triton:alpha:muon is assumed to be 5:2:1:2:2. The probability threshold is therefore chosen to be 1.0×10^{-4} in in order to have both relatively low missing and contamination fractions compare to the statistical uncertainty of the measurement. The resulted band of protons is shown in (figure 5.8).

Possible backgrounds

There are several sources of potential backgrounds in this proton measurement:

1. Protons emitted after capture of scattered muons in the lead shield: the incoming muons could be scattered to other materials surrounding the target, emitting protons to the silicon detectors. In order to avoid complication of estimating this background, we used lead sheets to collimate and shield around the target and detectors. If a scattered muon is captured by the lead shielding, the proton from lead would be emitted shortly after the muon hit because of the short average lifetime of muons in lead

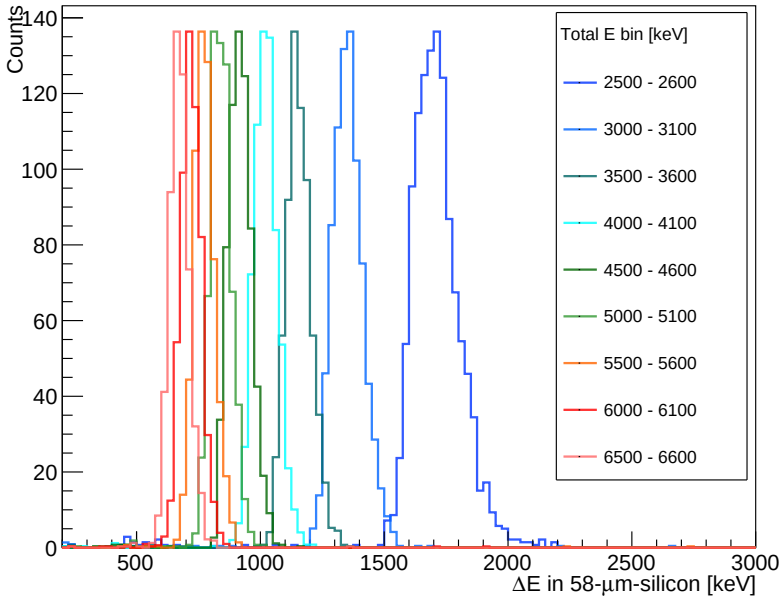

Figure 5.7: Distributions of ΔE of protons in a 58-µm-thick silicon detector for given E in various energy ranges.

P_i **threshold**	**Equiv.** σ	**Left**	**Right**	**Miss. flat**	**Contam. flat**	**Miss. expo.**	**Contam. expo.**
4.5×10^{-2}	2	1720	2214	1.9%	0.03%	6.1%	0.06%
2.7×10^{-3}	3	1801	2340	0.7%	0.05%	2.8%	0.1%
1.0×10^{-4}	3.89	1822	2373	0.5%	0.1%	1.2%	0.3%
5.7×10^{-7}	5	1867	2421	0.4%	0.7%	0.7%	0.9%

Table 5.4: Proton yields in energy range from 2.2 MeV to 8 MeV on the two silicon arms with different thresholds on proton-like probability P_i, and the MC calculated missing fractions and contamination levels with two different assumptions on spectrum shape: flatly distributed, and exponential decay spectrum (see (3.14)).

(78.4 ns [35]). In comparison, average lifetime of muons in aluminium is 864 ns [35], therefore a simple cut in timing could eliminate background of this kind.
The timing of events classified as protons are plotted in figure 5.9. The spectra show no significant fast decaying component, which should show up if the background from lead shielding were sizeable. A fit of an exponential function on top of a flat background gives the average lifetimes of muons as:

$$\tau_{\text{left}} = 870(25)\,\text{ns}\,, \tag{5.7}$$

$$\tau_{\text{right}} = 868(21)\,\text{ns}\,. \tag{5.8}$$

The consistency between fitted lifetimes and the reference value of average lifetime of muons in aluminium at 864(2) ns suggests the background from the lead shielding is negligible. This smallness can be explained as a combination of the two facts: (i) only a minority fraction of muons punched through the target and reached the downstream lead shield as illustrated in figure 5.4; and (ii) the probability of emitting protons from lead is very low compare to that of aluminium, about 0.4% per capture (see table 3.5).

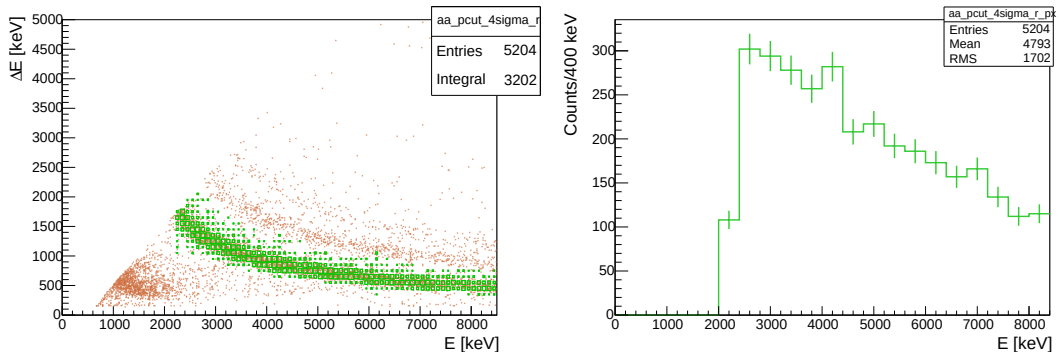

Figure 5.8: Protons (green) selected using the likelihood probability cut of 1.0×10^{-4} (left). The proton spectrum (right) is obtained by projecting the proton band onto the total energy axis.

2. The protons emitted after scattered muons stopped at the surface of the thin silicon detectors: these protons could mimic the signal if they appear within 1 µs around the time muon hit the upstream counter. The ΔE and E in this case would be sum of energy of a muon and energy of the resulted proton. The average energy of scattered muons can be seen in figure 5.5 to be about 1.4 MeV. The measured ΔE and E then would be shifted by 1.4 MeV, makes the measured data point move far away from the expected proton band. Therefore this kind of background should be small with the current probability cut.

3. The random background: this kind of background can be examined by the same timing spectrum in figure 5.9. The random events show up at negative time difference and large delay time regions and give a negligible contribution to the total number of protons.

It is concluded from above arguments that the backgrounds of this proton measurement is negligibly small.

5.3 Proton emission rate from aluminium

The analysis is done on the same dataset used in section 5.2. Firstly, the number of protons emitted is extracted using specific energy loss. Then correction for energy loss inside the target is applied. Finally, the number of protons is normalised to the number of nuclear muon captures.

5.3.1 Number of protons emitted

The numbers of protons in the energy range from 2.2 MeV to 8.5 MeV after applying the probability cut are:

$$N_{\text{p meas. left}} = 1822 \pm 42.7\,, \tag{5.9}$$

$$N_{\text{p meas. right}} = 2373 \pm 48.7\,. \tag{5.10}$$

The right arm received significantly more protons than the left arm did, which is expected as in section 5.2.1 where it is shown that muons stopped off-centred to the right arm.

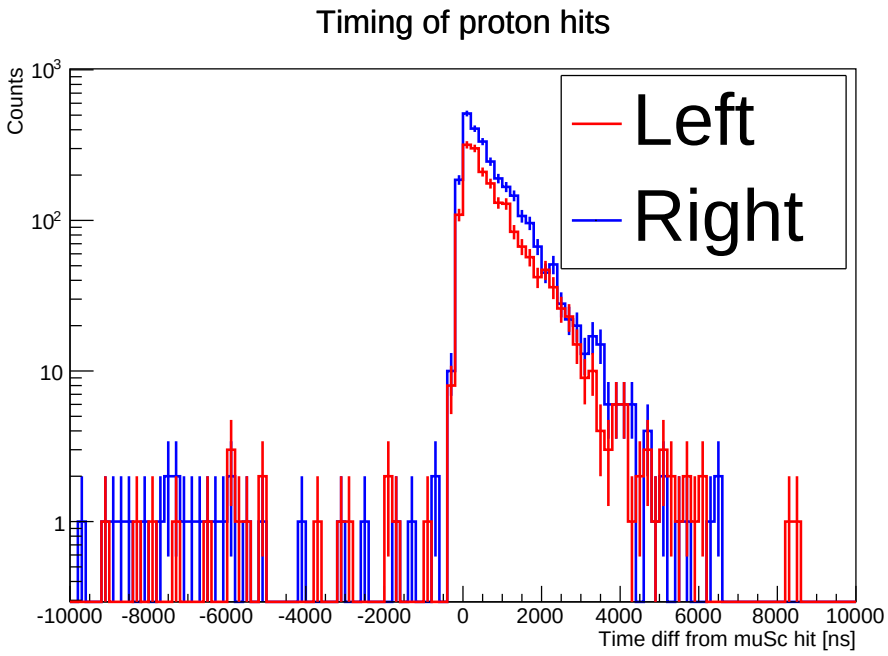

Figure 5.9: Timing of protons relative to muon hit. The spectra show the characteristic one-component decay shape.

5.3.2 Corrections for the number of protons

The protons spectra observed by the silicon detectors have been modified by the energy loss inside the target so correction (or unfolding) is necessary. The unfolding, essentially, is finding a response function that relates proton's true energy and measured value. This can be done in MC simulation by generating protons with a spatial distribution as close as possible to the real distribution of muons inside the target, then counting the number of protons reaching the silicon detectors. Such response function conveniently includes the geometrical acceptance.

For the 100-µm aluminium target and muons at the momentum scale of 1.09, the parameters of the initial protons are:

- horizontal distribution: Gaussian 26 mm FWHM, centred at the centre of the target;
- vertical distribution: Gaussian 15 mm FWHM, centred at the centre of the target;
- depth: Gaussian 69.2 µm FWHM, centred at 68.8 µm-deep from the upstream face of the target;
- energy: flatly distributed from 1.5 MeV to 15 MeV.

The calculated response matrices for the two arms are presented in figure 5.10. The different path lengths inside the target to the two silicon arms causes the difference in the two matrices. The response matrices are then used as MC truth to train and test the unfolding code. The code uses an existing ROOT package called RooUnfold [55] where the iterative Bayesian unfolding method is implemented. The unfolded spectra using the two observed spectra at the two arms as input are shown in figure 5.11. The two unfolded spectra generally agree with each other, except for a few first and last bins. In the lower energy region, there is a small probability for such protons to escape and reach the detectors, therefore the unfolding is generally unstable and the uncertainties are large. At the higher end, the jump on the right arm at around 9 MeV can be explained as the punch-through protons were

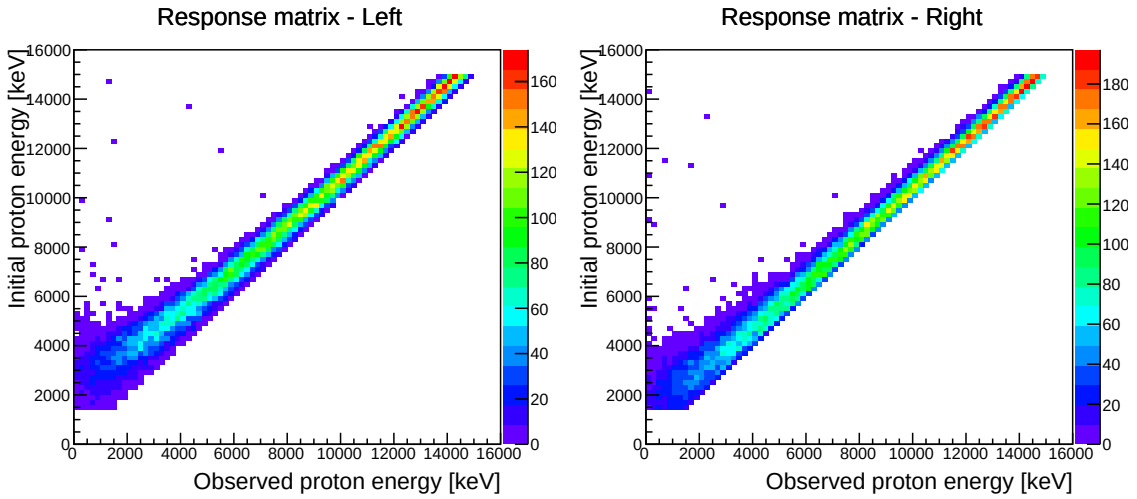

Figure 5.10: Response functions for the two silicon arms, showing the relation between protons energy at birth and as detected by the silicon detector arms.

counted as the proton veto counters were not used in this analysis. The lower threshold on the thin silicon detector at the right arm compared with that at the left arm makes this misidentification worse.

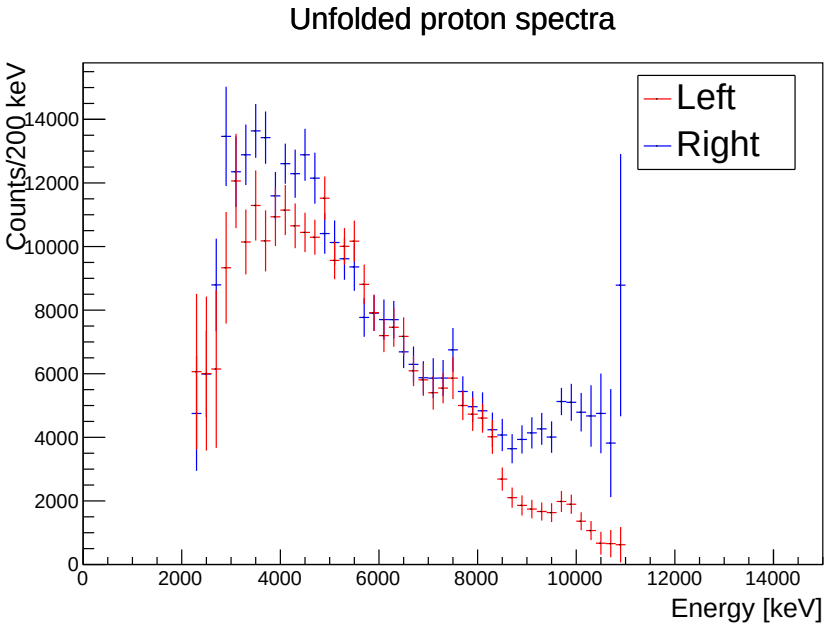

Figure 5.11: Unfolded proton spectra from the 100-µm aluminium target.

The stability of the unfolding code is tested by varying the lower and upper cut-off energies of the input spectrum. Plots in figure 5.12 show that the shapes of the unfolded spectra are stable after a few first or last bins.

The proton yields calculated from observed spectra in two arms are compared in figure 5.13 where the upper limit of the integrals is fixed at 8 MeV, and the lower limit is varied in 400 keV step. The upper limit was chosen to avoid the effects of punched through protons. The difference is large at cut-off energies less than 4 MeV due to large uncertainties at the first bins. Above 4 MeV, the two arms show consistent numbers of protons. The

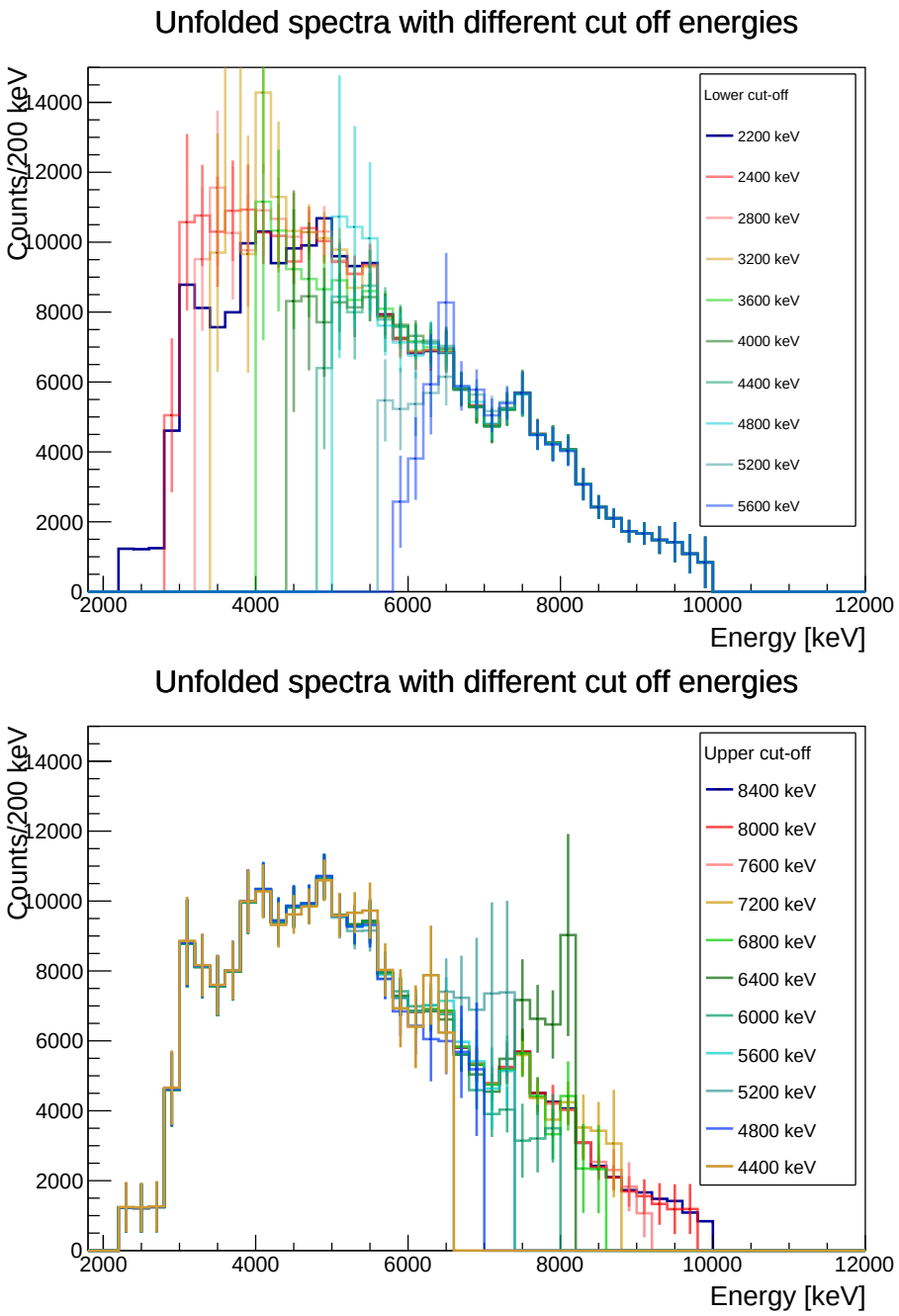

Figure 5.12: Unfolded spectra with different lower (top) and upper (bottom) cut-off energies.

yields of protons from 4 MeV to 8 MeV are:

$$N_{\text{p unfold left}} = (165.4 \pm 2.7) \times 10^3 \tag{5.11}$$

$$N_{\text{p unfold right}} = (173.1 \pm 2.9) \times 10^3 \tag{5.12}$$

The number of emitted protons is taken as average of the two yields:

$$N_{\text{p unfold}} = (169.3 \pm 1.9) \times 10^3 \tag{5.13}$$

5.3.3 Number of nuclear captures

Fitting the double peaks on top of a linear background gives the X-ray peak area of 5903.5 ± 109.2. With the same procedure as in the case of the active target, the number stopped

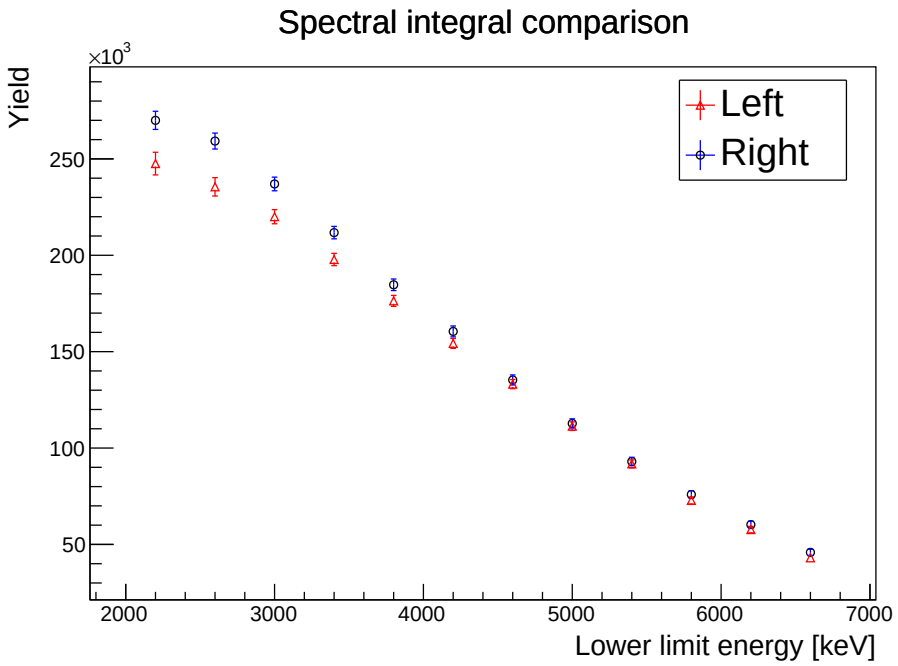

Figure 5.13: Proton yields calculated from two arms. The upper limit of integrations is fixed at 8 MeV, the horizontal axis is the lower limit of the integrations. The proton yields on the two arm agree well with each other from above 4 MeV.

muons and the number of nuclear captures are:

$$N_{\mu \text{ stopped}} = (1.57 \pm 0.05) \times 10^7 \,, \tag{5.14}$$

$$N_{\mu \text{ nucl. cap.}} = (9.57 \pm 0.31) \times 10^6 \,. \tag{5.15}$$

5.3.4 Proton emission rate

The proton emission rate in the range from 4 MeV to 8 MeV is therefore:

$$R_\text{p} = \frac{169.3 \times 10^3}{9.57 \times 10^6} = 1.7 \times 10^{-2} \,. \tag{5.16}$$

The total proton emission rate can be estimated by assuming a spectrum shape with the same parameterisation as in (3.14). The (3.14) function has a power rising edge, and a exponential decay falling edge. The falling edge has only one decay component and is suitable to describe the proton spectrum with the equilibrium emission only assumption. The pre-equilibrium emission contribution should be small for low-Z material, for aluminium the contribution of this component is 2.2% of total number of protons according to Lifshitz and Singer [49]. The fitted results are shown in figure 5.14 and table 5.5. The average spectrum is obtained by taking the average of the two unfolded spectra from the left and right arms. The fitted parameters are compatible with each other within their errors.

Using the fitted parameters of the average spectrum, the integration in range from 4 MeV to 8 MeV is 51% of the total number of protons. The total proton emission rate is therefore estimated to be 3.5×10^{-2}.

5.3.5 Uncertainties of the emission rate

The uncertainties of the emission rate come from:

- uncertainties in the number of nuclear captures: these were discussed in section 5.1.2;

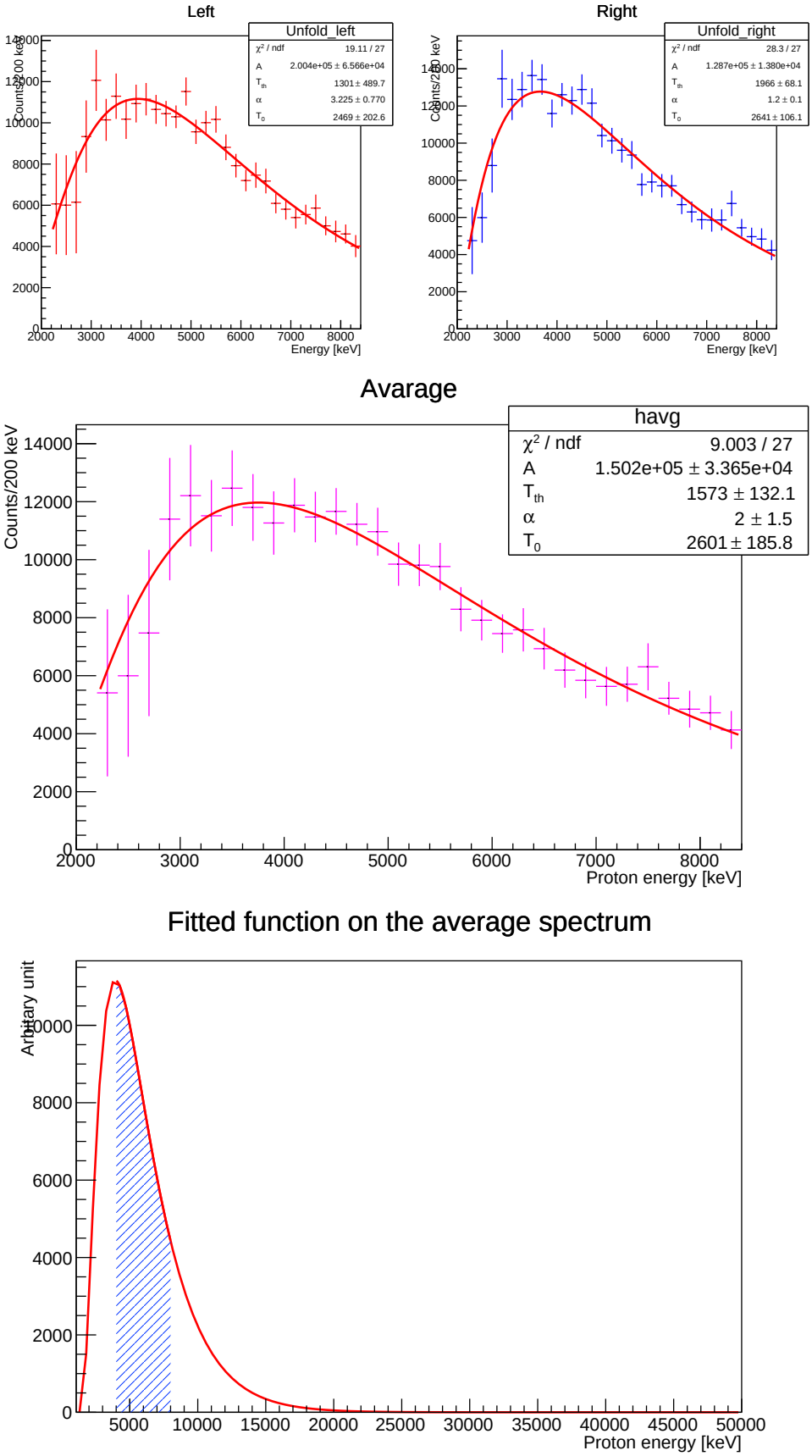

Figure 5.14: Fitting of the unfolded spectra on the left and right arms (top), and on the average spectrum (middle). The bottom plot shows the fitted function of the average spectrum in the energy range from 1 MeV to 50 MeV. The proton yield in the region from 4 MeV to 8 MeV (shaded) is 51% of the whole spectral integral.

Parameter	Left	Right	Average
$A \times 10^{-5}$	2.0 ± 0.7	1.3 ± 0.1	1.5 ± 0.3
T_{th} (keV)	1301 ± 490	1966 ± 68	1573 ± 132
α	3.2 ± 0.7	1.2 ± 0.1	2.0 ± 1.2
T_0 (keV)	2469 ± 203	2641 ± 106	2601 ± 186

Table 5.5: Parameters of the fits on the unfolded spectra, the average spectrum is obtained by taking average of the unfolded spectra from left and right arms.

- uncertainties in the number of protons:
  - statistical uncertainties of the measured spectra which are propagated during the unfolding process;
  - systematic uncertainties due to misidentification: this number is small compared to other uncertainties as discussed in section 5.2.2;
  - systematic uncertainty from the unfolding

The last item is studied by MC method using the parameterisation in section 5.3.4:

- protons with energy distribution obeying the parameterisation are generated inside the target. The spatial distribution is the same as that of in section 5.3.2. MC truth including initial energies and positions are recorded;
- the number of protons reaching the silicon detectors are counted, the proton yield is set to be the same as the measured yield to make the statistical uncertainties comparable;
- the unfolding is applied on the observed proton spectra, and the results are compared with the MC truth.

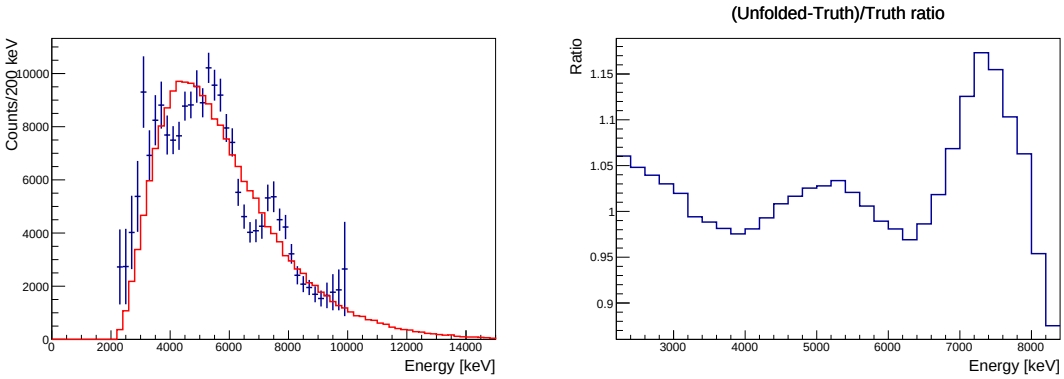

Figure 5.15: Comparison between an unfolded spectrum and MC truth. On the left hand side, the solid, red line is MC truth, the blue histogram is the unfoldede spectrum. The ratio between the two yields is compared in the right hand side plot with the upper end of integration is fixed at 8 MeV, and a moving lower end of integration. The discrepancy is genenerally smaller than 5% if the lower end energy is smaller than 6 MeV.

Figure 5.15 shows that the yield obtained after unfolding is in agreement with that from the MC truth. The difference is less than 5% if the integration is taken in the range from 4 MeV to 8 MeV. Therefore a systematic uncertainty of 5% is assigned for the unfolding routine.

A summary of uncertainties in the measurement of proton emission rate is presented in table 5.6.

Item	Value
Number of muons	3.2%
Statistical from measured spectra	1.1%
Systematic from unfolding	5.0%
Systematic from PID	<1.0%
Total	6.1%

Table 5.6: Uncertainties of the proton emission rate.

5.4 Results of the initial analysis

5.4.1 Verification of the experimental method

The experimental method described in section 3.4.2 has been validated:

- Number of muon capture normalisation: the number of stopped muons calculated from the muonic X-ray spectrum is shown to be consistent with that calculated from the active target spectrum.
- Particle identification: the particle identification by specific energy loss has been demonstrated. The banding of different particle species is clearly visible. The proton extraction method using cut on likelihood probability has been established. Since the distribution of ΔE at a given E is not Gaussian, the fraction of protons that do not make the cut is 0.5%, much larger than the threshold at 1×10^{-4}. The fraction of other charged particles being misidentified as protons is smaller than 0.1%. These uncertainties from particle identification are still small in compared with the uncertainty of the measurement (2.3%).
- Unfolding of the proton spectrum: the unfolded spectra inferred from two measurements at the two silicon arms show good agreement with each other, and with the muon stopping distribution obtained in the momentum scanning analysis.

5.4.2 Proton emission rates and spectrum

The proton emission spectrum in section 5.3.4 peaks around 3.7 MeV which is a little below the Coulomb barrier for proton of 3.9 MeV calculated using (3.12). The spectrum has a decay constant of 2.6 MeV in higher energy region.

The partial emission rate measured in the energy range from 4 MeV to 8 MeV is:

$$R_{p\ \text{meas.}} = (1.7 \pm 0.1)\%. \tag{5.17}$$

The total emission rate from aluminium assuming the spectrum shape holds for all energy is:

$$R_{p\ \text{total}} = (3.5 \pm 0.2)\%. \tag{5.18}$$

Comparison to theoretical and other experimental results

There is no existing experimental or theoretical work that could be directly compared with the obtained proton emission rate. Indirectly, it is compatible with the figures calculated by Lifshitz and Singer [48, 49] listed in table 3.5. It is significantly larger than the rate of 0.97% for the $(\mu, \nu p)$ channel, and does not exceed the inclusion rate for all channels $\Sigma(\mu, \nu p(xn))$ at 4%, leaving some room for other modes such as emission of deuterons or

tritons. Certainly, when the full analysis is available, deuterons and tritons emission rates could be extracted and the combined emission rate could be compared directly with the inclusive rate.

The result (5.18) is greater than the probability of the reaction $(\mu, \nu pn)$ measured by Wyttenbach et al. [46] at 2.8%. It is expectable because the contribution from the $(\mu, \nu d)$ channel should be small since it needs to form a deuteron from a proton and a neutron.

The rate of 3.5% was estimated with an assumption that all protons are emitted in equilibrium. With the exponential constant of 2.6 MeV, the proton yield in the range from 40 MeV to 70 MeV is negligibly small ($\sim 10^{-8}$). However, Krane and colleagues reported a significant yield of 0.1% in that region [42]. The energetic proton spectrum shape also has a different exponential constant of 7.5 MeV. One explanation for these protons is that they are emitted by other mechanisms, such as capture on two-nucleon cluster suggested by Singer [51] (see section 3.3.2 and table 3.6). Despite being sizeable, the yield of high energy protons is still small (3%) in compared with the result in (5.18).

Comparison to the silicon result

The probability of proton emission per nuclear capture of 3.5% is indeed much smaller than that of silicon. It is even lower than the rate of the no-neutron reaction $(\mu, \nu p)$. This can be explained as the resulted nucleus from muon capture on silicon, ^{28}Al, is an odd-odd nucleus and less stable than that from aluminium, ^{27}Mg. The proton separation energy for ^{28}Al is 9.6 MeV, which is significantly lower than that of ^{27}Mg at 15.0 MeV [56].

The proton spectrum from aluminium is softer than silicon charged particles spectrum of Sobottka and Wills [32] where the decay constant was 4.6 MeV. Two possible reasons can explain this difference in shape:

1. The higher proton separation energy of ^{27}Mg gives less phase space for protons at higher energies than that in the case of ^{28}Al if the excitation energies of the two compound nuclei are similar.

2. The silicon spectrum includes other heavier particles which have higher Coulomb barriers, hence contribute more in the higher energy bins, effectively reduces the decay rate.

Chapter 6

Impact to the COMET Phase-I

The measured proton emission rate of 3.5% is about 5 times smaller than the figure using to make the baseline design of the CDC in COMET Phase-I. The spectrum shape is softer than that of silicon, peaks around 4 MeV rather than at 2.5 MeV (figure 3.4). Therefore CDC hit rate due to proton should be smaller than the current estimation.

The CDC proton hit rate is calculated by a toy MC study. The dimensions of the geometry shown in figure 6.1 are from section 2.3.3. The inner wall of the CDC is 0.5 mm thick CFRP. A proton absorber made of CFRP is placed 5 cm far from the inner wall of the CDC. The absorber's thickness is varied from 0 (no absorber) to 1 mm.

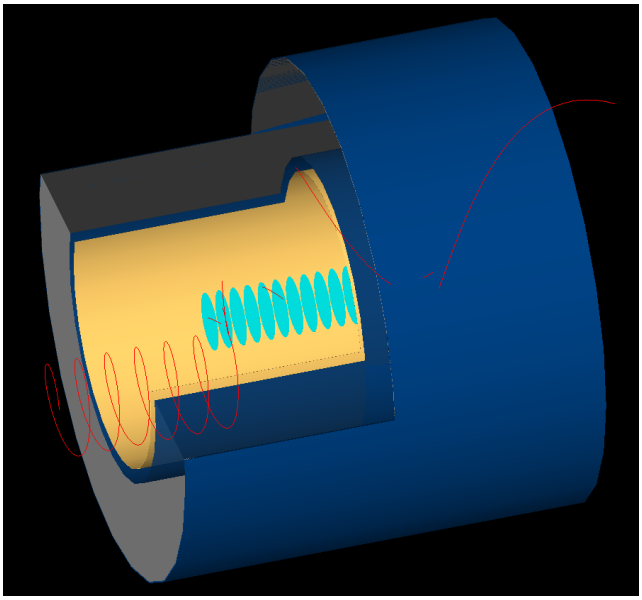

Figure 6.1: Geometry of the toy MC study for hit rate study.

The protons with the energy spectrum shape as in section 5.3.4 are generated inside the COMET's muon stopping targets which are 17 200-µm-thick aluminium discs. The spatial distribution of protons resembles the stopping distribution of muons inside the target discs calculated from the full MC simulation of the COMET detectors (figure 6.2).

The protons are then tracked in a 1 T magnetic field. The protons reaching the absorber, inner wall and the sensitive volume of the CDC are recorded (see figure 6.3).

A muon stopping rate of 1.3×10^9 Hz is assumed as in the COMET Phase I's TDR. The number of proton emitted is then $1.3 \times 10^9 \times 0.609 \times 0.035 = 2.8 \times 10^7$ Hz. The hit rates on a single cell in the inner most layer due to these protons with different absorber configurations are listed in table 6.1.

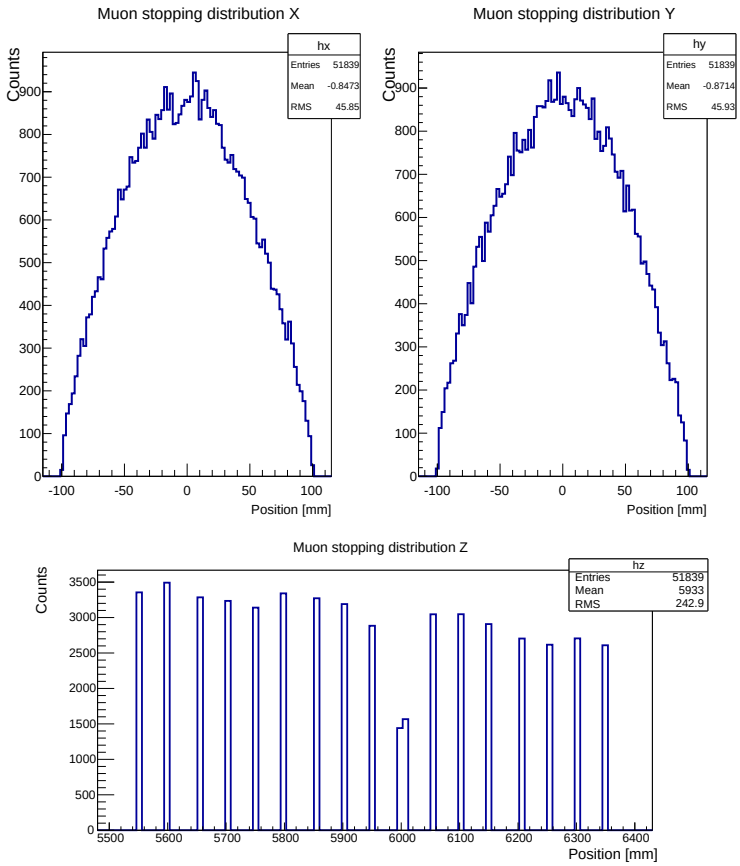

Figure 6.2: Spatial distribution of the generated protons in X, Y (top) and Z (bottom). Z is the axis of the CDC, X, Y are the horizontal and vertical axes respectively.

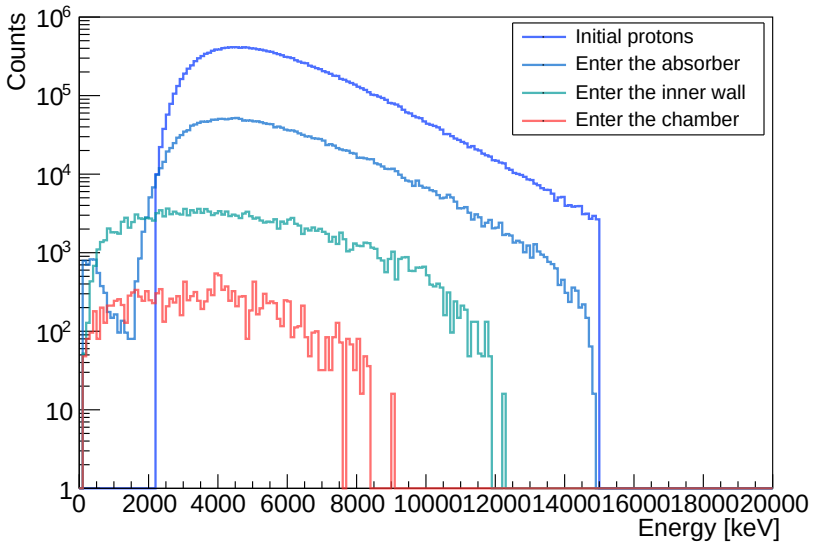

Figure 6.3: Proton energy spectra at different stages from birth to the sensitive volume of the CDC. The baseline design of 0.5 mm thick absorber and 0.5 mm thick inner wall was used to produce this plot.

At the baseline design of 0.5 mm, the hit rate is only 126 Hz, much smaller than the current estimation at 11 kHz. Even without the absorber, proton hit rate remains lower

Absorber thickness (mm)	**Inner wall thickness** (mm)	**Total CFRP thickness** (mm)	**Proton hit rate Phase-I TDR** (Hz)	**Proton hit rate New estimation** (Hz)
1	0.5	1.5	4×10^3	2
0.5	0.5	1.0	11×10^3	126
0	0.5	0.5	30×10^3	1436

Table 6.1: CDC proton hit rates in this study in comparison with the expected rates in COMET Phase-I's Technical Design Report [30] at different configurations of proton absorber and inner wall.

than that level at 1.4 kHz. Therefore the absorber is not necessary as far as the hit rate is concerned.

If the proton absorber is not used, the momentum spread of the signal electron reduces from 167 keV/c to 131 keV/c (table 6.2). This is a small improvement since the momentum resolution is dominated by intrinsic spread of 197 keV/c due to multiple scattering in gas and wires.

The last column of table 6.2 shows the integrated charge per unit length of a wire. The TDR deems an integrated charge level of 200 mC cm^{-1} safe. So even with the pessimistic estimation using silicon rate and spectrum and without the proton absorber, the integrated charge level in the CDC is still below the requirement. Therefore removing the absorber will not worsen the ageing process of the wires.

Absorber thickness (mm)	**Inner wall thickness** (mm)	**Total CFRP thickness** (mm)	**Momentum spread Δp** (keV/c)	**Integrated charge 300 days** (mC/cm)
1	0.5	1.5	195	25
0.5	0.5	1.0	167	60
0	0.5	0.5	133	160

Table 6.2: Momentum spreads due to the inner wall and absorber, and integrated charge per unit length of wire as calculated in the COMET Phase-I's TDR. The momentum spreads were calculated for signal electrons at 104.96 MeV/c. The integrated charge is estimated assuming 300 days of operation.

In summary, the toy MC study with the preliminary proton rate and spectrum shows that a proton absorber is not needed. It confirms the known fact that the estimation used in COMET Phase-I is conservative, and provides a solid prediction of the hit rate caused by protons.

Chapter 7

Conclusions

The AlCap is an experiment proposed at PSI to study charged particles, neutrons and photons emitting after nuclear muon capture on aluminium. These measurements are important for backgrounds and hit rates estimation of the new generation of $\mu - e$ conversion experiments, COMET and Mu2e. In the first stage of the COMET experiment, hit rate on its main tracking detector is anticipated to be dominated by low energy protons following muon capture on an aluminium target, which has never been measured.

The first run of the AlCap which aims for proton measurement has been carried out in 2013. Data analysis is in progress. Before finishing the complete AlCap analysis, an initial analysis on partial data was made. The main results are:

1. demonstration of the analysis chain from trigger-less waveforms to correlated physics events;

2. validation of the experimental method including: number of nuclear capture muons normalisation by muonic X-ray measurement, charged particle identification by specific energy loss, and unfolding of the proton energy spectrum using the iterative Bayesian method;

3. obtaining preliminary results on proton emission rate and spectrum: the proton spectrum has a peak at 3.7 MeV, then reduces exponentially with a decay constant of 2.6 MeV. The partial emission rate in the energy range from 4 MeV to 8 MeV is $(1.7 \pm 0.1)\%$ per nuclear muon capture, and the total emission rate assuming the shape holds for the whole spectrum is $(3.5 \pm 0.2)\%$ per nuclear muon capture.

The emission rate is consistent with the lower limit of 2.8% set by Wyttenbach et al. [46]. It is also compatible with the theoretical calculation by Lifshitz and Singer [49]. Compared with the existing result on silicon [32], the emission rate from aluminium is significantly smaller and the spectrum is softer.

The proton rate and spectrum have been used to optimise the planned proton absorber for the drift chamber of the COMET Phase-I. The resulted proton hit rate with the baseline configuration is very small compared with the current figure.The recommendation to the COMET Phase-I is to remove the proton absorber altogether. The momentum resolution of the drift chamber will be slightly improved, and the level of integrated charge will still remain below the safe level for the chamber.

The AlCap experiment is going to submit a beam time request for the 2015 run to collect more data and other measurements for neutrons and gamma rays.

Bibliography

[1] The COMET Collaboration, D. Bryman *et al.*, *An Experimental Search for Lepton Flavor Violating $\mu^- - e^-$ Conversion at Sensitivity of 10^{-16} with a Slow-Extracted Bunched Proton Beam*, **J-PARC Proposal P21** (2007).

[2] SINDRUM II Collaboration, W. H. Bertl *et al.*, Eur.Phys.J. **C47**, 337 (2006).

[3] Particle Data Group, J. Beringer *et al.*, Phys. Rev. D **86**, 010001 (2012).

[4] L. Michel, Proc.Phys.Soc. **A63**, 514 (1950).

[5] W. Fetscher, H. Gerber, and K. Johnson, Phys.Lett. **B173**, 102 (1986).

[6] S. Eckstein and R. Pratt, Annals of Physics **8**, 297 (1959).

[7] E. Hincks and B. Pontecorvo, Phys.Rev. **73**, 257 (1948).

[8] R. D. Sard and E. J. Althaus, Phys. Rev. **74**, 1364 (1948).

[9] G. Danby *et al.*, Phys.Rev.Lett. **9**, 36 (1962).

[10] Z. Maki, M. Nakagawa, and S. Sakata, Prog.Theor.Phys. **28**, 870 (1962).

[11] W. J. Marciano, T. Mori, and J. M. Roney, Ann.Rev.Nucl.Part.Sci. **58**, 315 (2008).

[12] S. Mihara, J. Miller, P. Paradisi, and G. Piredda, Ann.Rev.Nucl.Part.Sci. **63**, 531 (2013).

[13] R. H. Bernstein and P. S. Cooper, Phys.Rept. **532**, 27 (2013), 1307.5787.

[14] MEG Collaboration, J. Adam *et al.*, Phys.Rev.Lett. **110**, 201801 (2013), 1303.0754.

[15] T. Suzuki, D. F. Measday, and J. Roalsvig, Physical Review C **35**, 2212 (1987).

[16] A. Lagarrigue and C. Peyrou, Comptes Rendus Acad. Sci. Paris **234**, 1873 (1952).

[17] J. Steinberger and H. B. Wolfe, Phys. Rev. **100**, 1490 (1955).

[18] R. D. Sard, K. M. Crowe, and H. Kruger, Phys. Rev. **121**, 619 (1961).

[19] M. Conversi, L. di Lella, A. Egidi, C. Rubbia, and M. Toller, Phys. Rev. **122**, 687 (1961).

[20] G. Conforto *et al.*, Il Nuovo Cimento **26**, 261 (1962).

[21] J. Bartley, H. Davies, H. Muirhead, and T. Woodhead, Physics Letters **13**, 258 (1964).

[22] D. Bryman, M. Blecher, K. Gotow, and R. Powers, Phys. Rev. Lett. **28**, 1469 (1972).

[23] A. Badertscher *et al.*, Phys. Rev. Lett. **39**, 1385 (1977).

[24] A. Badertscher *et al.*, Nuclear Physics A **377**, 406 (1982).

[25] S. Ahmad *et al.*, Phys. Rev. D **38**, 2102 (1988).

[26] C. Dohmen *et al.*, Physics Letters B **317**, 631 (1993).

[27] (SINDRUM II Collaboration), W. Honecker *et al.*, Phys. Rev. Lett. **76**, 200 (1996).

[28] COMET, *Conceptual Design Report for experimental search for lepton flavor violating* $\mu^- - e^-$ *conversion at sensitivity of* 10^{-16} *with a slow-extracted bunched proton beam*, **KEK Report** (2009).

[29] The COMET Collaboration, R. Akhmetshin *et al.*, *Experimental Proposal for Phase-I of the COMET Experiment at J-PARC*, **KEK Report KEK/J-PARC-PAC 2012-10** (2012).

[30] COMET, *COMET Phase-I Technical Design Report*, **KEK Report** (2014).

[31] V. Cirigliano, R. Kitano, Y. Okada, and P. Tuzon, Phys. Rev. D **80**, 013002 (2009).

[32] S. E. Sobottka and E. L. Wills, Phys. Rev. Lett. **20**, 596 (1968).

[33] AlCap Collaboration, P. Kammel *et al.*, *Study of Muon Capture for Muon to Electron Conversion Experiments*, **PSI Proposal R-13-03.1** (2012).

[34] P. Singer, Springer Tracts Mod.Phys. **71**, 39 (1974).

[35] D. Measday, Phys.Rept. **354**, 243 (2001).

[36] E. Fermi and E. Teller, Phys.Rev. **72**, 399 (1947).

[37] C. Wu and L. Wilets, Ann.Rev.Nucl.Part.Sci. **19**, 527 (1969).

[38] N. C. Mukhopadhyay, Phys.Rept. **30**, 1 (1977).

[39] V. Andreev *et al.*, Phys. Rev. Lett. **110**, 012504 (2013).

[40] H. Morinaga and W. Fry, Il Nuovo Cimento **10**, 308 (1953).

[41] D. Kotelchuck and J. V. Tyler, Phys. Rev. **165**, 1190 (1968).

[42] K. Krane *et al.*, Physical Review C **20**, 1873 (1979).

[43] Y. Budyashov, V. Zinov, A. Konin, A. Mukhin, and A. Chatrchian, Sov.Phys.JETP **33**, 11 (1971).

[44] M. Balandin, V. Grebenyuk, V. Zinov, T. Kozlowski, and A. Konin, Yad.Fiz. **28**, 582 (1978).

[45] L. Vil'gel'mova, V. Evseev, L. Nikityuk, V. Pokrovskii, and I. Yutlandov, Yadern. Fiz. **13**, 551 (1971).

[46] A. Wyttenbach *et al.*, Nucl.Phys. **A294**, 278 (1978).

[47] C. Ishii, Progress of Theoretical Physics **21**, 663 (1959).

[48] M. Lifshitz and P. Singer, Phys.Rev.Lett. **41**, 18 (1978).

[49] M. Lifshitz and P. Singer, Phys.Rev. **C22**, 2135 (1980).

[50] M. Lifshitz and P. Singer, Phys.Lett. **B215**, 607 (1988).

[51] P. Singer, Phys. Rev. **124**, 1602 (1961).

[52] F. Foroughli, *$\pi E1$ secondary beam line*, **PSI Technical note** (1997).

[53] D. F. Measday, T. J. Stocki, B. A. Moftah, and H. Tam, Phys. Rev. C **76**, 035504 (2007).

[54] GEANT4, S. Agostinelli *et al.*, Nucl. Instrum. Meth. **A506**, 250 (2003).

[55] T. Adye, ArXiv e-prints (2011), 1105.1160.

[56] G. Audi, A. Wapstra, and C. Thibault, Nucl. Phys. A **729**, 337 (2003), The 2003 {NUBASE} and Atomic Mass Evaluations.